Universität Hamburg
DER FORSCHUNG | DER LEHRE | DER BILDUNG

Deutsches Elektronen-Synchrotron DESY
A Research Centre
of the Helmholtz Association

Crystal and Surface Structure of $(Al_xGa_{1-x})_2O_3$

Dissertation

zur Erlangung des Doktorgrades

an der Fakultät für Mathematik, Informatik und Naturwissenschaften

Fachbereich Physik
der Universität Hamburg

vorgelegt von

Ming-Chao Kao

Betreuung : Prof. Dr. Andreas Stierle

Co-Betreuung : Dr. Vedran Vonk

Hamburg

October 2026

Gutachter/innen der Dissertation:	Prof. Dr. Andreas Stierle Dr. Vedran Vonk
Zusammensetzung der Prüfungskommission:	Prof. Dr. Andreas Stierle Dr. Vedran Vonk Prof. Dr. Wolfgang Parak Prof. Dr. Jan Ingo Flege Prof. Dr. Gabriel Bester
Vorsitzende/r der Prüfungskommission:	Prof. Dr. Wolfgang Parak
Datum der Disputation:	30.09.2026
Vorsitzender des Fach-Promotionsausschusses PHYSIK:	Prof. Dr. Johannes Haller
Leiter des Fachbereichs PHYSIK:	Prof. Dr. Markus Drescher
Dekan der Fakultät MIN:	Prof. Dr.-Ing. Norbert Ritter

Eidesstattliche Erklärung / Declaration on oath

Hiermit erkläre und versichere ich, dass diese Dissertation von mir selbst verfasst wurde und meine eigene Arbeit ist. Ich bestätige, dass ich keine Hilfsmittel oder Quellen verwendet habe, außer denjenigen, die ausdrücklich anerkannt und ordnungsgemäß im Dokument referenziert sind. Zudem versichere ich, dass diese Dissertation in keiner Form für einen anderen Abschluss oder eine andere Qualifikation an dieser oder einer anderen Universität eingereicht oder akzeptiert wurde.

I hereby declare and affirm that this doctoral dissertation is my own work and has been written by me. I confirm that I have not used any aids or sources other than those explicitly acknowledged and properly referenced in the document. Additionally, I certify that this dissertation has not been submitted for, nor accepted in any form for, another degree or qualification at this or any other university.

Date	Signature of doctoral candidate

Preface

This dissertation is submitted in partial fulfillment of the requirements for the degree of Doctor of Physics at the University of Hamburg. It is presented as a cumulative thesis and is based on one peer-reviewed research publication and a manuscript scheduled for submission before the end of 2026. The research was carried out between 2023 and 2026 at the DESY NanoLab. During this time, I was employed as a doctoral researcher, and the outstanding scientific environment and research infrastructure at DESY NanoLab provided crucial support for the successful completion of this work.

List of publications and contributions:
This thesis consists of the following publication and manuscript.

Paper: Surface termination of β-Ga_2O_3(100) as-cleaved single crystals
Ming-Chao Kao, Lukas Paul Schewe, Arub Akhtar, Alina Vlad, Thomas F. Keller, Karsten Henkel, Saud Bin Anooz, Andreas Popp, Zbigniew Galazka, Jan Ingo Flege, Andreas Stierle, Vedran Vonk
Zbigniew Galazka grew the high-quality gallium oxide single crystal at IKZ in Berlin. Alina Vlad is the beamline scientist, who helped to set up the experiment and assisted in aligning the instrument at the SIXS beamline at the SOLEIL synchrotron in Paris. Lukas Paul Schewe, Arub Akhtar, Vedran Vonk, and I participated in the beamtime at SOLEIL and carried out all data acquisition. Thomas F. Keller assisted and guided me in the processing and analysis of the AFM images. Vedran Vonk and Andreas Stierle provided support with the CTR data simulation and analysis, as well as guidance with composing the manuscript. All authors contributed by suggesting improvements to the manuscript. Overall, I performed all data acquisition, simulation, and analysis, as well as the writing of the manuscript and the supporting information.

Manuscript : X-ray study of $(Al_xGa_{1-x})_2O_3$ single crystals and their (100) cleave plane
Ming-Chao Kao, Lukas Paul Schewe, Arub Akhtar, Luis Felipe Mochalski, Luisa Wartner, Carsten Paulmann, Alina Vlad, Karsten Henkel, Saud Bin Anooz, Andreas Popp, Zbigniew Galazka, Jan

Ingo Flege, Andreas Stierle, Vedran Vonk

Part of the results presented in this publication originate from the experiment reported in Paper 1, where the same group of colleagues supported the work. Another part of the results was obtained at the P24 beamline at DESY in PETRA III. During this beamtime, Carsten Paulmann the beamline scientist, helped to set up the experiment and assisted in aligning the instrument. Lukas Paul Schewe, Luis Felipe Mochalski, Luisa Wartner, Vedran Vonk, and I participated in the measurements and carried out all data acquisition. Vedran Vonk and Andreas Stierle provided support with the CTR data simulation and analysis, as well as guidance with composing the manuscript. All authors contributed by suggesting improvements to the final text. Overall, I performed all data acquisition, simulation, and analysis, as well as the writing of the manuscript and the supporting information.

Abstract

Gallium oxide (β-Ga_2O_3) is a highly promising wide-band-gap semiconductor for high-power electronic applications due to its large calculated critical field strength and favorable material properties. In particular, alloying with aluminium offers a viable route for band-gap engineering, enabling a tunable increase of the band gap from β-Ga_2O_3 to Al_2O_3 while aiming to preserve high crystal quality and useful electron transport properties. Understanding both the bulk properties and surface structure of $(Al_xGa_{1-x})_2O_3$ is therefore essential for future device processing and application.

In this work, β-Ga_2O_3 and Al-alloyed $(Al_xGa_{1-x})_2O_3$ as-cleaved single crystals were investigated using X-ray scattering techniques, including X-ray diffraction (XRD), X-ray reflectivity (XRR), and surface X-ray diffraction (SXRD), complemented by atomic force microscopy (AFM) and low-energy electron diffraction (LEED). Single-crystal X-ray diffraction (SCXRD) was employed to determine the precise lattice parameters and to evaluate the bulk crystal quality. SXRD was used to investigate the surface structures of all the as-cleaved crystals. In addition, the actual aluminum composition, x, of the crystals was determined with an accuracy of approximately 1% by combining the average electron density obtained from XRR fitting with the lattice parameters derived from SCXRD.

The cleaved (100) surfaces of β-Ga_2O_3 and $(Al_xGa_{1-x})_2O_3$ were found to cleave at the so-called B-termination, corresponding to planes formed by edge-sharing oxygen octahedra and involving the breaking of the longest and weakest Ga–O bonds. SXRD refinements showed only minor deviations from the bulk atomic positions, with displacements of at most about 0.1 Å. AFM measurements revealed relatively large terraces separated by steps of approximately half the a-axis length, or about 0.6 nm, indicating that adjacent terraces possess the same atomic termination and are related by crystal symmetry. The β-Ga_2O_3 (100) surface was found to be nearly bulk-terminated and remained smooth up to 800 °C. For the Al-alloyed crystal, the SXRD data likewise indicated B-termination; however, the surface composition

appeared to be Ga-rich, suggesting possible surface segregation after mild oxygen annealing. These results provide fundamental insight into the bulk ordering, alloy composition, and cleavage behavior of $(Al_xGa_{1-x})_2O_3$ single crystals. Such knowledge is important for the controlled processing of these materials and for their future use in semiconductor devices where surface stability, structural perfection, and band-gap engineering are critical.

Kurzfassung

Galliumoxid (β-Ga_2O_3) ist aufgrund seiner hohen berechneten kritischen Feldstärke und günstigen Materialeigenschaften ein äußerst vielversprechender Weitbandlücken-Halbleiter für Hochleistungsanwendungen in der Elektronik. Insbesondere bietet die Legierung mit Aluminium einen praktikablen Ansatz zur Bandlücken-Optimierung, da sich damit eine einstellbare Vergrößerung der Bandlücke von β-Ga_2O_3 bis Al_2O_3 realisieren lässt, während gleichzeitig eine hohe Kristallqualität und nützliche Elektronentransporteigenschaften erhalten bleiben sollen. Das Verständnis sowohl der Volumeneigenschaften als auch der Oberflächenstruktur von $(Al_xGa_{1-x})_2O_3$ ist daher für die zukünftige Prozessierung und Anwendung von entscheidender Bedeutung.

In dieser Arbeit wurden frisch gespaltene Einkristalle von β-Ga_2O_3 und Al-legiertem $(Al_xGa_{1-x})_2O_3$ mithilfe von Röntgenstreumethoden untersucht, darunter Röntgenbeugung (XR D), Röntgenreflektometrie (XRR) und Oberflächen Röntgenbeugung (SXRD), ergänzt durch Rasterkraftmikroskopie (AFM) und Niederenergie-Elektronenbeugung (LEED). Die Einkristall Röntgenbeugung (SCXRD) wurde verwendet, um die präzisen Gitterparameter zu bestimmen und die Volumenqualität der Kristalle zu bewerten. SXRD diente zur Untersuchung der Oberflächenstrukturen aller frisch gespaltenen Kristalle. Darüber hinaus wurde die tatsächliche Aluminiumzusammensetzung, x, der Kristalle mit einer Genauigkeit von etwa 1% bestimmt, indem die aus der XRR-Anpassung erhaltene mittlere Elektronendichte mit den aus SCXRD abgeleiteten Gitterparametern kombiniert wurde.

Die gespaltenen (100)-Oberflächen von β-Ga_2O_3 und $(Al_xGa_{1-x})_2O_3$ zeigten eine Spaltung an der sogenannten B-Termination, die den Ebenen entspricht, die durch kantenverknüpfte Sauerstoffoktaeder gebildet werden und das Brechen der längsten und schwächsten Ga–O Bindungen beinhalten. Die SXRD-Verfeinerungen ergaben nur geringe Abweichungen von den Volumen-Atompositionen, mit Verschiebungen von höchstens etwa 0.1 Å. AFM-Messungen zeigten relativ große Terrassen, die durch Stufen von ungefähr der halben a-Achsenlänge, also

etwa 0.6 nm, getrennt sind, was darauf hindeutet, dass benachbarte Terrassen dieselbe atomare Terminierung aufweisen und durch Kristallsymmetrie miteinander in Beziehung stehen. Für die (100)-Oberfläche von β-Ga_2O_3 wurde festgestellt, dass sie nahezu volumen-terminiert ist und bis 800 °C glatt bleibt. Für den Al-legierten Kristall ergaben die SXRD-Daten ebenfalls eine B-Termination; die Oberflächenzusammensetzung schien jedoch Ga-reich zu sein, was auf eine mögliche Oberflächensegregation nach mildem Sauerstoff-Tempern hindeutet. Diese Ergebnisse liefern grundlegende Einblicke in die Ordnung im Volumen, die Legierungszusammensetzung und das Spaltverhalten von $(Al_xGa_{1-x})_2O_3$ Einkristallen. Ein solches Wissen ist wichtig für die kontrollierte Verarbeitung dieser Materialien und für ihren zukünftigen Einsatz in Halbleiterbauelementen, bei denen Oberflächenstabilität, strukturelle Perfektion und Bandlücken-Engineering entscheidend sind.

Contents

Preface v

Abstract vii

Kurzfassung ix

1 Introduction 1

1.1 Motivation . . . 1

1.2 Applications of Gallium Oxide . . . 2

1.3 Research Goals . . . 6

2 Surface Science Theory and Experimental Methods 9

2.1 Principles of X-ray Interaction with Matter . . . 9

2.1.1 Surface X-ray Diffraction (SXRD) . . . 14

2.1.2 Crystal Truncation Rods (CTR) Analysis . . . 16

2.1.3 X-ray Reflectivity (XRR) . . . 17

2.2 Low-Energy Electron Diffraction (LEED) . . . 21

2.3 Atomic Force Microscopy (AFM) . . . 25

2.4 Experimental Setups Overview . . . 26

2.4.1 Laboratories at the DESY NanoLab . . . 27

2.4.2 SXRD beamtime at SIXS beamline (Soleil Synchrotron) . . . 29

2.4.3 Crystallography beamtime at P24 beamline (PTERA III, DESY) . . . 31

2.5 Data Acquisition and Analysis Workflows . . . 32

2.5.1 Surface X-ray Diffraction Data Processing and Analysis . . . 32

2.5.2 SC-XRD Data Integration and Analysis . . . 36

3 Gallium Oxide - Crystal Structure, Growth, Surface Preparation **39**
3.1 Bulk Crystal Structure . . . 39
3.2 Gallium Oxide β-Ga_2O_3 (100) Single Crystal . . . 40
3.3 $(Al_xGa_{1-x})_2O_3$ (100) (x = 0-0.3) Single Crystals . . . 42
3.4 Growth of High-Quality Crystals . . . 45
3.4.1 Czochralski Method . . . 46
3.4.2 Metalorganic Chemical Vapor Phase Epitaxy (MOVPE) Thin Films . . . 49
3.4.3 Cleavage Planes . . . 53
3.4.4 Termination of the (100) Surfaces . . . 54
3.4.5 Twin Domain in β-$(Al_xGa_{1-x})_2O_3$ Single Crystals . . . 56

4 Surface Crystallography of As-cleaved β-Ga_2O_3(100) Crystals **61**
4.1 Surface Termination of β-Ga_2O_3(100) As-cleaved Single Crystals . . . 61

5 X-ray Study of $(Al_xGa_{1-x})_2O_3$ Single Crystals and Their (100) Cleave Plane **69**

6 Summary and Conclusion **83**

A Appendix **87**
A.1 Surface Crystallography of As-cleaved β-Ga_2O_3(100) Crystals . . . 87
A.1.1 Supporting Information : Paper I . . . 87
A.2 X-ray study of $(Al_xGa_{1-x})_2O_3$ single crystals and their (100) cleave plane . . . 94
A.2.1 Supporting Information : Paper II . . . 94
A.3 Single-Crystal X-ray Diffraction Data (P24) . . . 103
A.4 Crystallography Data . . . 124

List of Figures **127**

List of Tables **135**

List of Publications **137**

Bibliography **139**

Acknowledgements **149**

Chapter 1

Introduction

1.1 Motivation

The growing demand for efficient energy conversion, renewable energy integration, and advanced power electronic systems has created a strong need for ultrawide-bandgap (UWBG) semiconductors capable of operating at higher voltages and currents, withstanding elevated temperatures and breakdown fields, and delivering lower power losses than conventional silicon-based technologies. Among the current state-of-the-art materials, silicon carbide (SiC) and gallium nitride (GaN) have achieved significant progress; however, Beta-type gallium oxide (β-Ga_2O_3) is predicted to surpass both due to its exceptionally high calculated critical field strength. [1, 2]

UWBG materials represent a promising route toward next-generation power electronics, and β-Ga_2O_3 has emerged as an especially attractive candidate due to its wide intrinsic bandgap, high critical breakdown field, and the availability of affordable native substrates. To expand its applicability and enable advanced device concepts, alloying β-Ga_2O_3 with aluminum has gained lots of interest, as Al incorporation enables controlled bandgap engineering, increasing the bandgap almost linearly from 4.85 eV in Ga_2O_3 to roughly 7 eV at high Al concentrations. The main challenge, however, is preserving reasonable electron mobility, which is already relatively modest in the pure material (around 150 $cm^2/V/s$). Understanding how Al incorporation affects the structural, electronic, and surface properties of the material is therefore essential for enabling the reliable fabrication of high-performance devices. [1–8]

Recent DFT and TEM studies (Akhtar et al.) of several $(Al_xGa_{1-x})_2O_3$ crystals indicate preferential ordering of Al and Ga between octahedral and tetrahedral lattice sites. [9] Additionally, our synchrotron-based surface X-ray diffraction (SXRD) studies of $(Al_xGa_{1-x})_2O_3$ (100) single

crystals with $x = 0$ - 0.3 reveal that the (100) cleaved surface is nearly bulk-terminated and maintains a smooth morphology up to 800°C under an oxygen partial pressure of 10^{-6} mbar. These findings highlight the structural robustness of the material and provide valuable insights into its stability under conditions relevant for epitaxial growth and device engineering.

This thesis is motivated by the need to gain a deeper understanding of the fundamental properties of β-Ga_2O_3 and $(Al_xGa_{1-x})_2O_3$ single crystals, which have so far received limited attention. In particular, this work focuses on synchrotron-based X-ray studies to elucidate the structural quality of single crystals and the epitaxial relationship of MOVPE-grown thin films, which are crucial for their application in high-power semiconductor electronics. It aims to address crucial knowledge gaps concerning the influence of aluminum incorporation on the structural and surface properties of $(Al_xGa_{1-x})_2O_3$ single crystals and their thin films. By employing state-of-the-art synchrotron-based X-ray diffraction techniques, this thesis seeks to provide a detailed investigation of the material structure, thereby establishing an important foundation for the further development of high-quality materials and the advancement of gallium oxide for next-generation power electronics.

1.2 Applications of Gallium Oxide

Gallium oxide, particularly its monoclinic beta-phase (β-Ga_2O_3), has emerged as one of the most promising UWBG semiconductor materials for next-generation electronic and optoelectronic technologies. With a band gap of approximately 4.85 eV, β-Ga_2O_3 uniquely combines deep-ultraviolet transparency with outstanding electrical properties. These characteristics enable a broad range of applications that require high power handling, high breakdown voltages, and strong UV sensitivity. To evaluate these material advantages for high-power device applications, Baliga's figure of merit (BFOM) is most commonly used, and is defined as [10]

$$\mathrm{BFOM} = \varepsilon \mu E_b^3 \tag{1.1}$$

where ε is the dielectric constant, μ is the charge carrier mobility, and E_b is the electrical breakdown field. As indicated by Equation 1.1, the BFOM is dominated by the cubic dependence on the breakdown field, giving UWBG materials a substantial theoretical advantage over conventional silicon (Si) and even established wide-bandgap semiconductors such as Si and GaN. In the case of β-Ga_2O_3, the electron mobility is lower than GaN. However, its exceptionally high critical breakdown field, estimated at around 8 MV/cm, yields a BFOM several

Table 1.1: Comparison of fundamental material parameters relevant to power semiconductors performance, including BFOM values. Table adapted from Higashiwaki et al. [12]

Property	Si	GaAs	4H-SiC	GaN	Diamond	β-Ga_2O_3
Bandgap E_g (eV)	1.1	1.4	3.3	3.4	5.5	4.8–4.9
Breakdown field E_b (MV/cm)	0.3	0.4	2.5	3.3	10	8
Electron mobility μ (cm^2/V·s)	1400	8000	1000	1200	2000	300
Relative dielectric constant ε	11.8	12.9	9.7	9.0	5.5	10
BFOM (relative) $\varepsilon\mu E_b^3$	**1**	**15**	**340**	**870**	**24664**	**3444**

times higher than GaN (3.3 MV/cm) and orders of magnitude greater than Si (0.3 MV/cm), as Table 1.1 summarized. [11, 12]

To further tune the properties of β-Ga_2O_3, it is possible to alloy it with aluminum, which leads to an almost linear increase in the band gap from 4.85 to 7 eV. [1, 2, 8] While tuning the band gap is advantageous, it is also essential to preserve high crystal quality and sufficient electron mobility. Pure β-Ga_2O_3 demonstrates an electron mobility of around 150 cm^2/(V·s), which is critical for device performance. Achieving these characteristics relies on precise control of the crystal growth process and a detailed understanding of the effects of alloying on both surface and bulk properties. Consequently, it is imperative to investigate the structure in great detail, serving as a fundamental basis for further development towards perfect materials.

In addition to these intrinsic electronic properties, β-Ga_2O_3 benefits from the feasibility of large-area single-crystal melt growth. Similar to the mature processes used for silicon wafers. It further strengthens the position of β-Ga_2O_3 and its alloy $(Al_xGa_{1-x})_2O_3$ as a cost-effective candidate for next-generation power electronics, solar-blind photodetectors and gas sensors. A rough overview of the relevant application space is shown in Figure 1.1(b), which maps device requirements in a two-dimensional power–frequency domain. The accessible power range is governed not only by current and voltage handling capabilities, but also by device ruggedness, thermal management, efficiency, linearity, size, cost, and existing technology infrastructure. [1, 3]

In this broader context, wide-bandgap (WBG) and UWBG semiconductors have attracted sustained interest for mid- to high-voltage applications as Figure 1.1(a) and (b), where silicon can no longer meet efficiency or functionality demands due to fundamental material limitations. [1, 13] UWBG materials, in particular, open pathways to the multi-kilovolt to megavolt regime that remains inaccessible to silicon and even to most established WBG semiconductors. Despite this substantial potential, WBG and UWBG materials still account for only a small share of today's power electronics market, underscoring both the challenge and the op-

portunity ahead. This chapter provides an overview of the key application areas of β-Ga_2O_3, highlighting the material advantages that underpin its growing technological relevance.

High-power electronic devices represent one of the most significant application areas for Gallium Oxide. For high-power switching, β-Ga_2O_3 is predicted to outperform SiC and GaN technologies due to its approximately three times higher critical electric field strength, and alloying with Al can even achieve bandgap engineering (for ultra-high-voltage switching), making it an attractive material for efficient next-generation power conversion systems with reduced energy loss. As a result, β-Ga_2O_3 is being extensively investigated for high-power switching components, [12] including field effect transistors, rectifiers, and power conversion systems. [14] Demonstrated device architectures, ranging from depletion mode to enhancement mode transistors, showcase the ability of β-Ga_2O_3 to operate reliably under high electric fields while maintaining low leakage currents. The combination of its high breakdown strength and the availability of large-area native substrates positions β-Ga_2O_3 as a strong candidate for next-generation power electronics requiring robust performance and minimized energy losses. [1–3]

Solar-blind UV photodetectors take advantage of the wide band gap of β-Ga_2O_3, which renders the material intrinsically insensitive to visible light while remaining strongly responsive to deep-UV radiation, a characteristic known as solar blindness. [15] This enables detector operation without interference from sunlight and is crucial for applications such as environ-

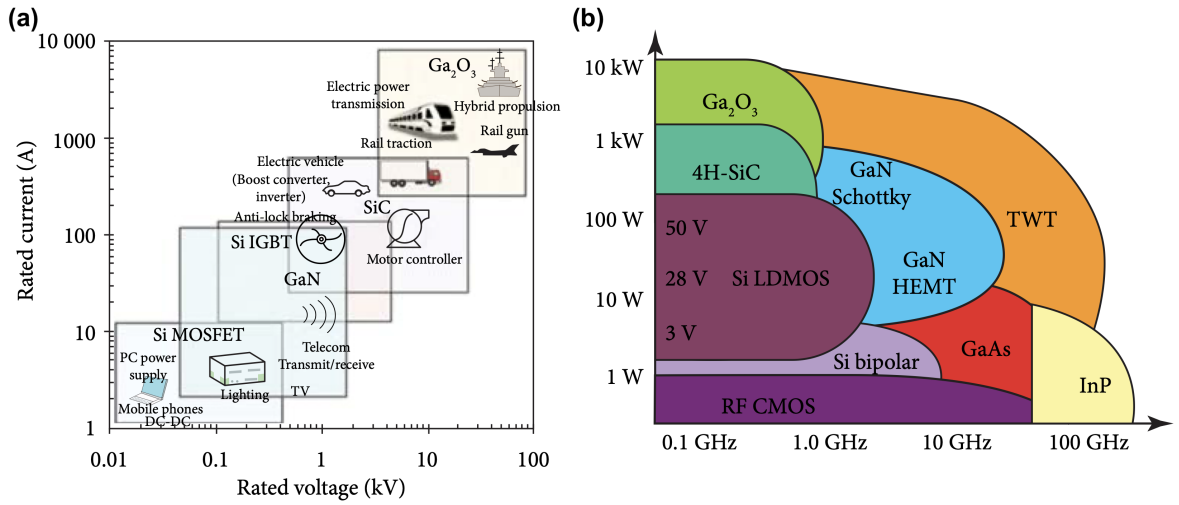


Figure 1.1: Application space of Si and wide-bandgap semiconductors. (a) Summary of voltage and current ratings reported for Si, SiC, GaN, and Ga_2O_3 power devices from Pearton et al. [13] (b) Power–frequency operating regimes as described by Mastro et al. [3] Figure adapted from [1, 3, 13].

mental monitoring, flame detection, missile tracking, and UV astronomy. [16,17] With a band gap of about 4.85 eV, [16] β-Ga_2O_3 offers low dark current, high responsivity, and stable performance under harsh environmental conditions. Its transparency in the visible spectrum combined with strong UV absorption further enhances device efficiency. In addition, Al-alloyed Ga_2O_3 provides tunable cutoff wavelength via bandgap engineering, enabling spectral selectivity beyond that of pure β-Ga_2O_3 and expanding its potential for deep-UV photodetectors design. Ongoing research continues to optimize device architectures and electrode geometries to achieve higher detectivity and faster response times in β-Ga_2O_3-based photodetectors. [17]

The high surface reactivity of β-Ga_2O_3, combined with its transparency and thermal stability, makes it suitable for gas sensing applications. Surface adsorption of gas molecules can significantly alter the electrical conductivity of β-Ga_2O_3, enabling detection of various chemical species. This sensitivity to surface interactions allows β-Ga_2O_3 based sensors to operate reliably even at elevated temperatures, surpassing the performance and durability of many conventional metal oxide sensors. Potential applications include environmental monitoring, industrial safety systems, and detection of hazardous gases. Advances in nanoscale β-Ga_2O_3 structures further enhance sensitivity and selectivity due to the larger active surface area and tunable surface chemical properties.

Gas Sensing with β-Ga_2O_3 leverages the material's strong surface reactivity, wide bandgap, and excellent thermal stability. When gas molecules adsorb onto the β-Ga_2O_3 surface, they induce measurable changes in electrical conductivity, enabling the detection of oxidizing and reducing gases even at high temperatures where many conventional metal-oxide sensors lose sensitivity. These properties make β-Ga_2O_3 a promising material for environmental monitoring, industrial safety, and the detection of hazardous gases. Advances in nanostructured β-Ga_2O_3 further enhance sensor performance through increased surface area and tunable surface chemistry. Moreover, accurate determination of the single-crystal surface structure, as presented in this study, is essential for understanding gas-adsorption mechanisms and for optimizing the future design and functionality of β-Ga_2O_3-based gas sensors. [16,17]

The diverse application landscape of β-Ga_2O_3 is driven by its exceptional material properties, including its ultra-wide band gap, high breakdown electric field, optical transparency, and adaptable surface chemistry. These characteristics support a wide range of devices, from high-power switches to solar-blind UV photodetectors and robust gas sensors, demonstrating the flexibility of β-Ga_2O_3 as a platform for next-generation electronic and optoelectronic technologies. As advances continue in crystal growth, defect control, surface characteriza-

tion, and nanoscale device engineering, the full potential of β-Ga_2O_3 will become increasingly accessible. Overall, these developments position β-Ga_2O_3 not only as a promising semiconductor for specialized applications but also as a key material for future high-performance, energy-efficient systems.

1.3 Research Goals

The primary mission of this research project is to perform a comprehensive analysis of the crystal structure, surface structure and morphology, and electronic properties of as-cleaved β-Ga_2O_3 and Al-alloyed $(Al_xGa_{1-x})_2O_3$ single crystals. This will be achieved by combining the advanced surface science techniques with cutting-edge synchrotron-based X-ray characterization methods, including LEED, AFM, XRR, SXRD, and SC-XRD. Specifically, this project aims to establish accurate atomic-level crystal models of the single crystal structure and their cleaved surfaces under ultra-high vacuum (UHV) conditions. We will investigate how aluminum incorporation affects lattice parameter evolution, site occupancy, and overall crystal quality. In addition, the synchrotron-based X-ray diffraction results will be used to clarify possible mechanisms related to aluminum distribution within the crystal, including diffusion, surface segregation, and potential phase separation. A further important goal is to understand how preparation steps such as cleavage and oxygen annealing affect surface structure and morphology. Therefore, a detailed understanding of surface termination, morphology, and structural stability is essential for optimizing subsequent thin-film growth processes. In this context, by correlating structural evolution with compositional changes and surface preparation conditions, this research will provide fundamental scientific insights relevant to the optimization of gallium oxide semiconductor wafer production and related thin-film processes.

1. **Structural Analysis of the Gallium Oxide single crystal Surfaces**
   Synchrotron-based SXRD, LEED, and AFM are used to precisely determine the surface structure and morphology of the β-Ga_2O_3 (100) single crystal. By analysing Crystal Truncation Rods (CTRs), atomic-structural models of the single crystal surface structure were presented. This structural characterization is directly relevant for $(Al_xGa_{1-x})_2O_3$ thin-film growth, since β-Ga_2O_3 single crystals serve as substrates for semiconductor applications. Thus, the surface termination, and surface morphology of the substrate which strongly influence nucleation, interface quality, and ultimately the structural and electronic properties of the grown films. A detailed understanding of the substrate sur-

face is therefore essential for optimizing preparation steps such as cleaving, oxygen annealing, and other surface treatments, as well as for highly surface-sensitive applications such as gas sensing, as mentioned above in Chapter 1.2.

2. **Influence of Al Alloying on Gallium Oxide single crystal Surfaces and Structure**
The recent availability of $(Al_xGa_{1-x})_2O_3$ single crystals opens new possibilities for bandgap engineering beyond β-Ga_2O_3, enabling materials with a wider band gap and potentially improved suitability for future power electronic and optoelectronic applications. [18] Systematic studies will be carried out to understand how aluminum incorporation modifies the crystal structure, physical properties, and overall quality of $(Al_xGa_{1-x})_2O_3$ single crystals. By analyzing synchrotron-based diffraction data, the evolution of structural and compositional characteristics across different Al alloying levels will be identified and correlated with changes within the crystal. Recent reported on $(Al_xGa_{1-x})_2O_3$ indicate a critical threshold at an Al composition of $x > 0.16$, which crystallinity begins to degrade and defects appear on the surface along the [201] and [001] direction. [19]

3. **Epitaxy of $(Al_xGa_{1-x})_2O_3$ Thin Film on β-Ga_2O_3 (100) Single Crystal**
The epitaxy of $(Al_xGa_{1-x})_2O_3$ thin films on β-Ga_2O_3 (100) single crystals is investigated. Since alloying with Al provides a way for bandgap engineering in β-Ga_2O_3, understanding the growth behavior and structural properties of these films is particular necessary for further applications. Synchrotron-based X-ray diffraction is employed to assess the structural quality of the films and their epitaxial relationship with the single crystal substrate, with particular emphasis on possible epitaxial strain, domains, and possible structural imperfections. These results help clarify the final crystal quality of $(Al_xGa_{1-x})_2O_3$ on the single crystal substrates and support their further development for future semiconductor applications.

Chapter 2

Surface Science Theory and Experimental Methods

This chapter introduces the methods used in this Ph.D. thesis and the theoretical concepts behind them. Chapter 2.1 discusses the interaction of X-rays with matter and the "surface sensitive" techniques derived from these principles. Chapter 2.2 then introduces Low-Energy Electron Diffraction, which is used to verify surface symmetry and sample quality. Finally, Chapter 2.3 describes Atomic Force Microscopy, which provides real-space images of the surface topography.

2.1 Principles of X-ray Interaction with Matter

The interaction of X-rays with matter provides the foundation for a variety of experimental techniques used to investigate the atomic structure of surfaces and interfaces. In particular, X-ray-based methods such as surface X-ray diffraction (SXRD), grazing incident X-ray diffraction (GIXRD), and X-ray reflectivity (XRR) are widely applied to determine atomic-scale structure, surface morphology, thickness, and density of layered structure. Since the 1980s, the availability of powerful synchrotron radiation sources has significantly advanced surface science studies using SXRD, in comparison with conventional rotating anode X-ray sources, which are orders of magnitude less intense. The following chapter is based on references. [20–22].

Before discussing specific surface-sensitive techniques, it is important to understand the basic physics of how X-rays interact with matter. X-rays are a form of electromagnetic radiation wave with high energy or short wavelength, which allows them to penetrate deeply into materials. When X-rays interact with atoms, they may be absorbed, scattered, or emitted, and

these processes depend on the energy of the X-rays and the properties of the material. X-rays can be described with the wavelength λ, which is related to the corresponding photon energy E_γ, and according to the Planck-Einstein relation

$$E_\gamma = \hbar k = \frac{hc}{\lambda} \tag{2.1}$$

where $h \approx 6.626 \times 10^{-34}$ J·s is the Planck constant, and $c \approx 2.998 \times 10^8$ m/s is the speed of light in vacuum, $\hbar$ is the reduced Planck constant, and $k = 2\pi/\lambda$ represents the magnitude of the wavevector. Because X-ray diffraction relies on length scales comparable to inter-atomic distances, wavelengths are typically expressed in Ångströms (Å). By combining the physical constants into a single factor, this relation can be written in a convenient form that directly converts between wavelength and photon energy (keV) as

$$\lambda(\text{Å}) \approx \frac{12.398}{E_\gamma(\text{keV})} \tag{2.2}$$

When X-rays interact with matter, several processes may occur, including photoelectric absorption, (inelastic) Compton scattering, and (elastic) Thomson scattering. Structural characterization techniques such as SXRD, CTR, and XRR rely predominantly on elastic scattering. In this process, the oscillating electric field ($\mathbf{E}$) of the incident X-ray wave forces the atomic electron cloud to oscillate at the frequency of the incident radiation. Since the electrons are much lighter than the atomic nuclei, they are driven to oscillate at the same frequency as the incoming radiation. These accelerating charges then re-emit electromagnetic radiation without a change in energy, so the scattered beam retains the same wavelength as the incident beam.

To describe this scattering event mathematically, we define the wavevectors of the incident and scattered beams as $\mathbf{k}_i$ and $\mathbf{k}_f$, respectively. Both vectors have a magnitude of $|\mathbf{k}| = 2\pi/\lambda$. The scattering geometry is entirely defined by the momentum transfer vector $\mathbf{Q}$, also known as the scattering vector

$$\mathbf{Q} = \mathbf{k}_f - \mathbf{k}_i \tag{2.3}$$

With the momentum transfer vector $\mathbf{Q}$ is defined, we can quantify the scattering behavior of a single atom. The scattering amplitude of an single atom $A(\mathbf{Q})$ is characterized by its (atomic) form factor $f^0(\mathbf{Q})$, which can be describes as

$$A(\mathbf{Q}) = -\mathbf{r}_e f^0(\mathbf{Q}) \tag{2.4}$$

where $r_e \approx 2.818 \times 10^{-15}$ m the classical electron radius (the Thomson scattering length) and $f^0(\mathbf{Q})$ is the atomic form factor. This form factor is the Fourier transform of the atom's electron density $\rho(\mathbf{r})$:

$$f^0(\mathbf{Q}) = \int_{\text{Atom}} \rho(\mathbf{r}) e^{i\mathbf{Q}\cdot\mathbf{r}} d\mathbf{r} \tag{2.5}$$

Since the electron cloud has a size comparable to the X-ray wavelength, scattering from different parts of the cloud can interfere. For $|\mathbf{Q}| \to 0$, all electrons scatter in phase and $|\mathbf{Q}| \to Z$, where Z is the number of electrons in the atom. For large $|\mathbf{Q}|$, destructive interference causes $f^0(\mathbf{Q})$. When the incident photon energy $E_\gamma = \hbar k$ approaches an atomic absorption edge, the scattering becomes energy dependent and resonance effects must be included. The full atomic form factor of an atom is then written as

$$f(\mathbf{Q}, \hbar\omega) = f^0(\mathbf{Q}) + f'(\hbar\omega) + if''(\hbar\omega) \tag{2.6}$$

Here, the correction terms are largely independent of $\mathbf{Q}$. The real component, $f'(\hbar\omega)$, represents the dispersion correction associated with the atomic level structure, while the imaginary component, $f''(\hbar\omega)$, accounts for photoelectric absorption effects in the scattered wave.

Ultimately, the measurable scattering intensity I_s from a single atom is proportional to the absolute square of the complex scattering amplitude, $A(\mathbf{Q})$:

$$I_s = |A(\mathbf{Q})|^2 = r_0^2 |f(\mathbf{Q}, \hbar\omega)|^2 P \tag{2.7}$$

where P is the polarization factor, which accounts for the polarization state of the incident synchrotron beam.

Scattering from a Crystal

When considering an ordered array of atoms, the crystal structure factor $F_{\text{crystal}}(\mathbf{Q})$, can be written as the product of the unit cell structure factor $F_{\text{unit cell}}$, and the lattice structure factor F_{lattice}. The mathematical derivation can be expressed as

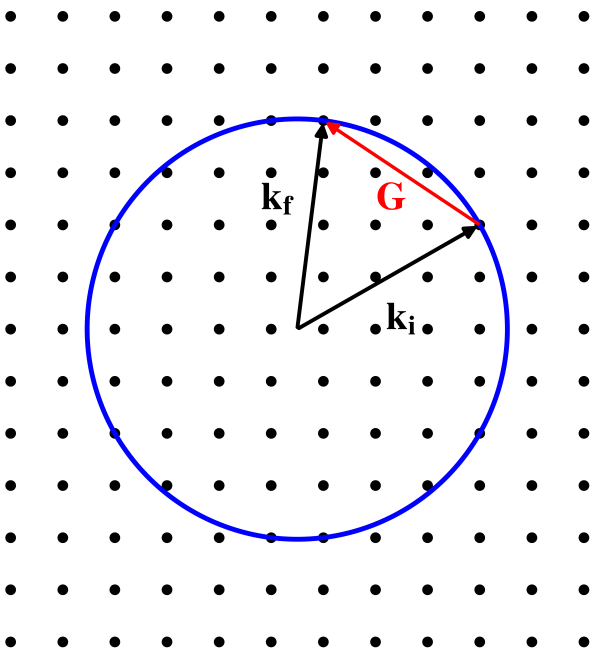


Figure 2.1: A schematic representation of the Ewald sphere construction in two dimensions. The reciprocal lattice points are indicated by black dots. The incident wavevector ($\mathbf{k}_i$) and the scattered wavevector ($\mathbf{k}_f$) originate from the center of the Ewald sphere (solid blue circle). The scattering vector ($\mathbf{G}$) connects the origin to the reciprocal lattice point, satisfying the Laue condition for diffraction ($\mathbf{k}_f - \mathbf{k}_i = \mathbf{G}$).

$$F_{\text{crystal}}(\mathbf{Q}) = F_{\text{unit cell}} \cdot F_{\text{lattice}} = \underbrace{\sum_j f_j(Q) e^{iQr_j}}_{\text{unit cell}} \underbrace{\sum_{n_1,n_2,n_3} e^{iQR_n}}_{\text{lattice sum}} \tag{2.8}$$

In this equation, the first summation represents the contribution from the arrangement of all atoms at positions $\mathbf{r}_j$ within a single unit cell, while the second summation (the lattice sum) covers every unit cell position in the entire lattice defined by the translation vector $\mathbf{R}_n = n_1\mathbf{a}_1 + n_2\mathbf{a}_2 + n_3\mathbf{a}_3$, where n_i are the integers. The mathematical derivation above is based on the "kinematic approximation," which assumes that X-rays interact weakly with matter and undergo scattering only once, neglecting multiple scattering events. For the lattice sum to yield a non-zero scattered intensity, the periodicity of the structure requires that the phase factor connects identical lattice positions, meaning $e^{i\mathbf{Q}\cdot\mathbf{R}_n} = 1$. This implies that the dot product of the momentum transfer $\mathbf{Q}$ and the lattice vector $\mathbf{R}_n$ must be an integer multiple of 2π, satisfying $\mathbf{Q} \cdot \mathbf{R}_n = 2\pi \times$ integer. This is known as the **Laue condition**, which is fulfilled when the momentum transfer matches a reciprocal lattice vector $\mathbf{Q} = \mathbf{G}$ as Figure 2.1 illustrated. The reciprocal lattice vector is defined as

$$\mathbf{Q} = \mathbf{G} = h\mathbf{a}_1^* + k\mathbf{a}_2^* + l\mathbf{a}_3^* \tag{2.9}$$

Consequently, only a few distinct points in the reciprocal space, so called Bragg peaks exhibit a scattered intensity greater than zero, while the intensity in most of the reciprocal space is zero. Furthermore, the Laue condition is physically equivalent to **Bragg's Law** as illustrated in Figure 2.2, directly connecting the scattering angle θ to the real-space lattice plane d-spacing via

$$n\lambda = 2d_{hkl}\sin\theta \tag{2.10}$$

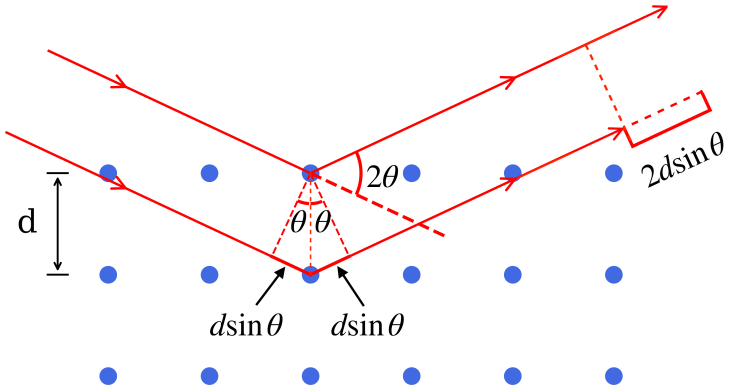


Figure 2.2: Bragg diffraction geometry. Constructive interference occurs when the path difference between rays reflected from adjacent lattice planes equals an integer multiple of the wavelength, $2d_{hkl}\sin\theta = n\lambda$. The angle between the incident and diffracted beams is 2θ.

The lattice plane spacing d_{hkl} for specific crystal systems can be calculated directly from their respective unit cell parameters. For a cubic lattice, where $a = b = c = a_0$. A hexagonal lattice, where $a = b \neq c$. And a monoclinic lattice, where $a \neq b \neq c$ and $\alpha = \gamma = 90°$, $\beta \neq 90°$, the d-spacing relationships with the corresponding lattice form can be expressed as

$$d_{\text{cube}} = \frac{a_0}{\sqrt{h^2 + k^2 + l^2}} \tag{2.11}$$

$$d_{\text{hexagonal}} = \left[\frac{4}{3}\left(\frac{h^2 + hk + k^2}{a^2}\right) + \frac{l^2}{c^2}\right]^{-1/2} \tag{2.12}$$

$$d_{\text{monoclinic}} = \left[\frac{1}{\sin^2\beta}\left(\frac{h^2}{a^2} + \frac{k^2\sin^2\beta}{b^2} + \frac{l^2}{c^2} - \frac{2hl\cos\beta}{ac}\right)\right]^{-1/2} \tag{2.13}$$

To intuitively demonstrate the effect of the number of unit cells on the lattice structure factor, the three-dimensional sum can be simplified to a one-dimensional linear array of N unit cells, where N is proportional to the size of the crystal. The absolute value of this structure factor is given by

$$|F_N(\mathbf{Q})| = \left| \sum_{n=0}^{N-1} e^{i\mathbf{Q}n\mathbf{a}} \right| = \frac{\sin(NQ_a a/2)}{\sin(Q_a a/2)} \tag{2.14}$$

This function exhibits strong maxima (Bragg peaks) at $Q_a a = 2\pi h$ for any integer h. Between two neighboring Bragg peaks, there are $N - 1$ intermediate Laue oscillation fringes. Here, $Q_a a$ denotes the momentum transfer along the lattice direction a, corresponding to the h-direction in reciprocal space. Figure 2.3 illustrates this finite size effect by plotting the structure factor amplitude for varying crystal thicknesses ($N = 4, 8$, and 60). As the number of unit cells N increases, the main Bragg peaks become drastically sharper and more intense, while the relative intensity of the intermediate fringes is highly suppressed. When $N \to \infty$, the structure factor perfectly converges to an infinitely narrow δ-function at the Bragg positions, representing an ideal, point-like diffraction pattern.

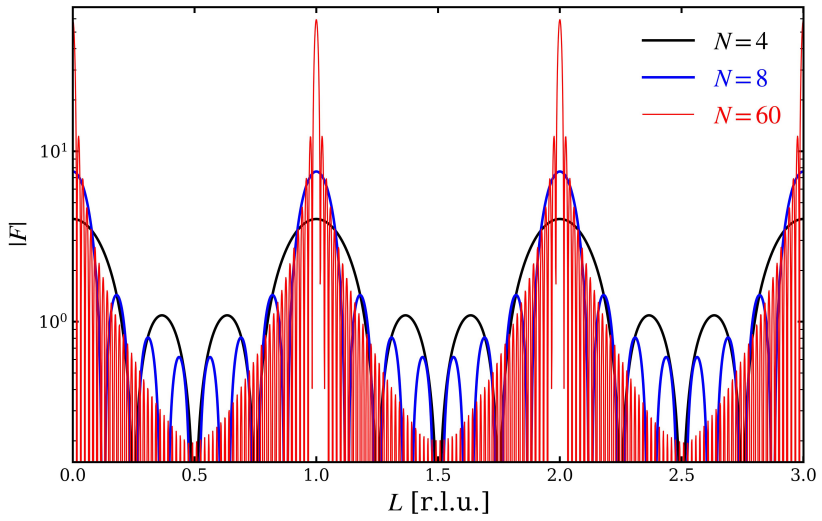


Figure 2.3: Calculated 1D structure factor amplitude $|F|$ demonstrating finite size effects for $N = 4$ (black), $N = 8$ (blue), and $N = 60$ (red) unit cells. As N increases, the intermediate Laue oscillation fringes are suppressed, and the main Bragg peaks rapidly converge toward sharp δ-functions.

2.1.1 Surface X-ray Diffraction (SXRD)

The principles of X-ray scattering are traditionally derived for an ideal crystal with perfect periodicity in all three dimensions. In such a crystal, the interference of scattered waves occurs

coherently in the h, k and l directions, leading to diffraction only at discrete points in reciprocal space, known as Bragg peaks, as illustrated in Figure 2.4(a). This condition is fulfilled when the Laue condition, $\mathbf{G} = \mathbf{Q}$, is strictly fulfilled, as previously mentioned.

SXRD extends this description to a real crystal systems in which three-dimensional translational symmetry is broken by truncation at a surface. When a crystal is truncated to form a surface, periodicity is preserved only within the surface plane, while it is interrupted along the surface normal. This loss of periodicity along l prevents complete destructive interference between atomic layers. Consequently, the scattered intensity does not vanish between Bragg peaks but instead remains finite along CTRs, with intensity maxima still occurring at the Bragg positions, as illustrated in Figure 2.4(b).

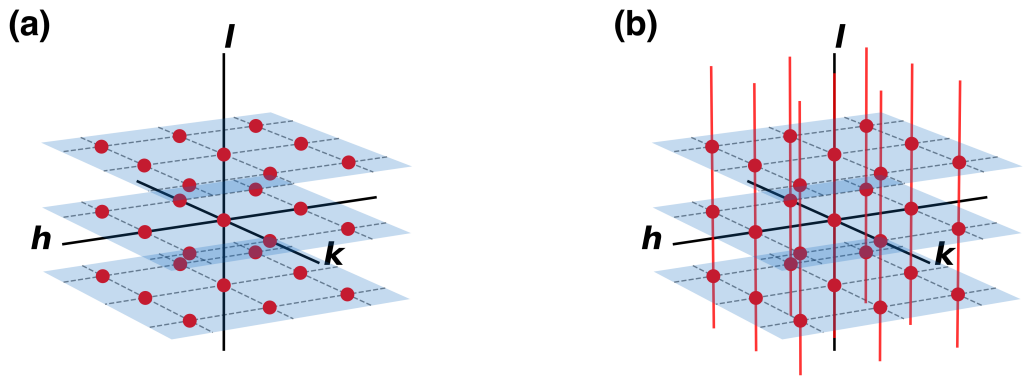


Figure 2.4: (a) In an infinite three-dimensional crystal, periodicity in the h, k and l directions gives rise to constructive interference in reciprocal space, producing diffraction at the Bragg peaks. (b) At the crystal surface, periodicity is interrupted, leading to incomplete interference along l. As a result, the scattered intensity along the CTRs remains non-zero and exhibits maxima at the Bragg peaks.

To model this, we assume an infinitely extended crystal in the directions of the in-plane unit vectors $\mathbf{a}_1$ and $\mathbf{a}_2$, which are parallel to the surface. The scattering amplitude of a single two-dimensional layer is denoted as $A(\mathbf{Q})$. Along the $\mathbf{a}_3$ direction (the z-axis), corresponding to the surface normal, the crystal is truncated, so that the summation over layers can be indexed by j, starts at $j = 0$ at the surface and extends to infinity into the bulk.

Since the X-ray beam is attenuated as it penetrates the crystal, an absorption parameter per layer is introduced by $\beta = a_3\mu/\sin\theta$, where μ is the linear absorption coefficient and θ is the incident angle. The total structure factor of the truncated crystal can then be expressed as a sum over these layers as

$$F_{\mathrm{CTR}} = A(\mathbf{Q}) \sum_{j=0}^{\infty} e^{iQ_z a_3 j} e^{-j\beta} = \frac{A(\mathbf{Q})}{1 - e^{iQ_z a_3} e^{-\beta}} \tag{2.15}$$

To maximize the sensitivity to this weak surface signal, SXRD measurements are typically carried out at or near the critical angle for total external reflection. Under these conditions, the amplitude of the evanescent wave penetrating the crystal is doubled, which leads to an enhancement of the measured diffraction signal by a factor of 4 (when neglecting absorption).

2.1.2 Crystal Truncation Rods (CTR) Analysis

Due to the incomplete destructive interference along the surface normal, the scattered intensity is not confined to discrete reciprocal lattice points but instead extends into continuous streaks perpendicular to the surface normal and passing through the Bragg peaks, as discussed previously as CTRs. Their characteristic intensity profile is illustrated in Figure 2.5, z denotes the fractional change in the spacing of the topmost surface layer relative to the bulk. The case $z = 0$ corresponds to an ideally terminated surface without relaxation, while positive values such as $z = 0.1$ indicate an expansion of the top layer and negative values such as $z = -0.1$ indicate a contraction.

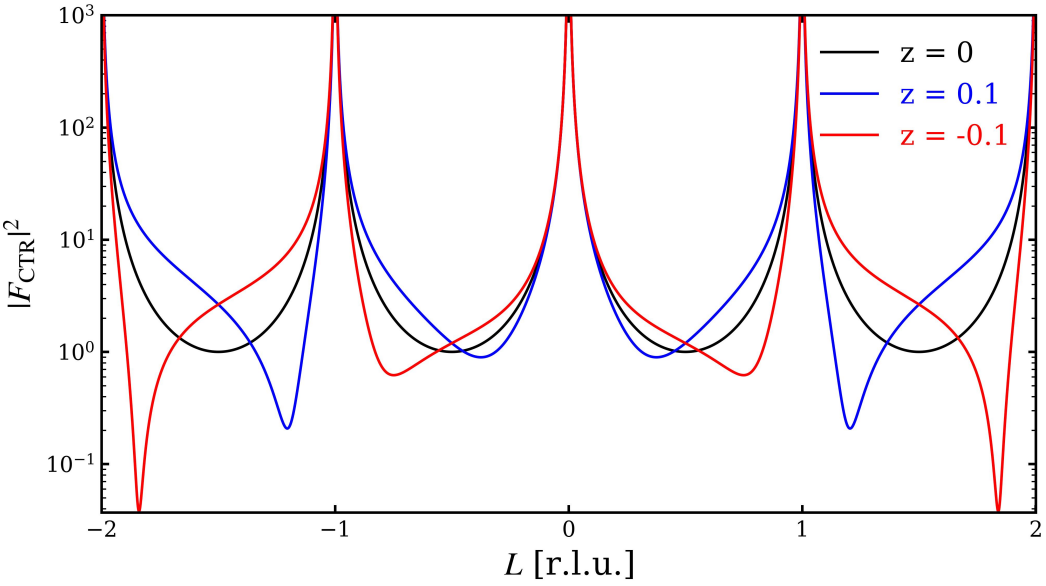


Figure 2.5: Calculated CTR intensity profile as a function of out-of-plane momentum transfer, l, showing the effect of surface relaxation. For an ideally terminated crystal with no surface relaxation ($z = 0$), the intensity decreases smoothly between the Bragg peaks ($l = 0, 1, 2, \ldots$). In contrast, surface expansion ($z > 0$) or contraction ($z < 0$) produces characteristic intensity differences which become more pronounced at higher momentum transfer.

The scattered intensity along a CTR is proportional to the square of the structure factor, as

$$I_{\mathrm{CTR}} = |F_{\mathrm{CTR}}|^2 = \frac{|A(\mathbf{Q})|^2}{(1 - e^{iQ_z a_3} e^{-\beta})(1 - e^{-iQ_z a_3} e^{-\beta})} \tag{2.16}$$

In the ideal case where absorption is negligible ($\beta = 0$), this equation can be simplified to

$$I_{\mathrm{CTR}} = \frac{|A(\mathbf{Q})|^2}{4\sin^2(Q_z a_3/2)} = \frac{|A(\mathbf{Q})|^2}{4\sin^2(\pi l)} \tag{2.17}$$

where the continuous variable $l = Q_z a_3/2\pi$ is introduced, representing the out-of-plane momentum transfer in reciprocal lattice units (r.l.u.). As visualized in Figure 2.5, this intensity function is continuously evaluated away from the Bragg peaks (i.e., where $l \neq 0, \pm 1, \pm 2, \dots$). The intensity reaches its maxima at the Bragg peaks and decreases sharply between them.

The shape and intensity profile of CTRs provide a sensitive fingerprint of the near-surface atomic structure. In real crystals, the surface layer often exhibits different atomic spacings or occupancies compared to the bulk substrate. If we consider a reconstructed top layer with a modified lattice spacing, the total structure factor becomes the sum of the bulk CTR and the top layer contribution.

$$F_{\mathrm{tot}} = F_{\mathrm{CTR}} + F_{\mathrm{top}} \tag{2.18}$$

Substituting the expression derived above and including a fractional change z in the top-layer spacing, the total structure factor then becomes

$$F_{\mathrm{tot}} = \frac{A(\mathbf{Q})}{1 - e^{2\pi i l}} + A(\mathbf{Q}) e^{-2\pi i (1+z) l} \tag{2.19}$$

Close to the Bragg peaks, the strong bulk scattering dominates, making the measurement relatively insensitive to surface modifications. In contrast, far from the Bragg peaks, particularly near the minima of the CTR at $l \approx 0.5, 1.5, \dots$, the effects of the surface-layer spacing (z) and site occupancy become more pronounced. By fitting the experimentally observed intensity profiles to these structure factor models, detailed information about surface relaxation and reconstruction can be extracted. Further details regarding the data analysis can be found in Chapter 2.5.

2.1.3 X-ray Reflectivity (XRR)

X-ray reflectivity (XRR) is based on the interaction between X-ray radiation and matter, as previously introduced. XRR is highly sensitive to changes in electron density along the surface

normal direction. As a result, it is a powerful non-destructive technique for characterizing layered structures with sub-nanometer resolution. It can be used to determine film thickness, surface roughness, and electron density in adlayers and thin films on a substrate.

The complex index of refraction n for X-rays can be described by

$$n = 1 - \delta + i\beta \tag{2.20}$$

The components δ (dispersion) and β (absorption) are intrinsically linked to the material's atomic composition and density. While the scattering phase shift δ is directly proportional to the electron density ρ_e of the material, the absorption term β, given by $\beta = \lambda\mu \,/\, 4\pi$,is related to the linear attenuation coefficient μ, which itself depends strongly on the material's mass density and atomic number. Since X-rays interact primarily with the electron clouds of the atoms in the medium, both δ and β reflect the underlying electron structure and composition of the material. The dispersion term δ can be explicitly expressed in terms of the material's effective scattering density ρ_s as

$$\delta = \frac{\lambda^2}{2\pi} r_e \rho_s \tag{2.21}$$

where λ is the incident X-ray wavelength and r_e is the classical electron radius ($r_e \approx 2.818 \times 10^{-15}$ m). It is important to note that although the scattering density ρ_s is primarily governed by the physical electron density ρ_e, it should be treated as an energy-dependent quantity since it includes anomalous scattering corrections, especially when the incident X-ray energy is close to the absorption edge of the elements. The physical electron density ρ_e can be further expressed in terms of the mass density ρ_m of the material. For a simple element with atomic number Z and atomic mass A, this relationship can be express as

$$\rho_e = \rho_m \frac{N_A}{A} Z \tag{2.22}$$

X-ray wavelengths are extremely short and their interaction with matter is relatively weak. As a result, both values of δ and β are exceptionally small, typically on the order of 10^{-5} or 10^{-6}. Consequently, the real part of the refractive index is slightly less than 1. When X-rays propagate from a medium with a higher refractive index, such as air or vacuum, where $n_1 = 1 - 10^{-6} \approx 1$, into a medium of lower refractive index ($n_2 < 1$), the beam refracts away from the surface normal. As shown in Figure 2.6, the relationship between the incident

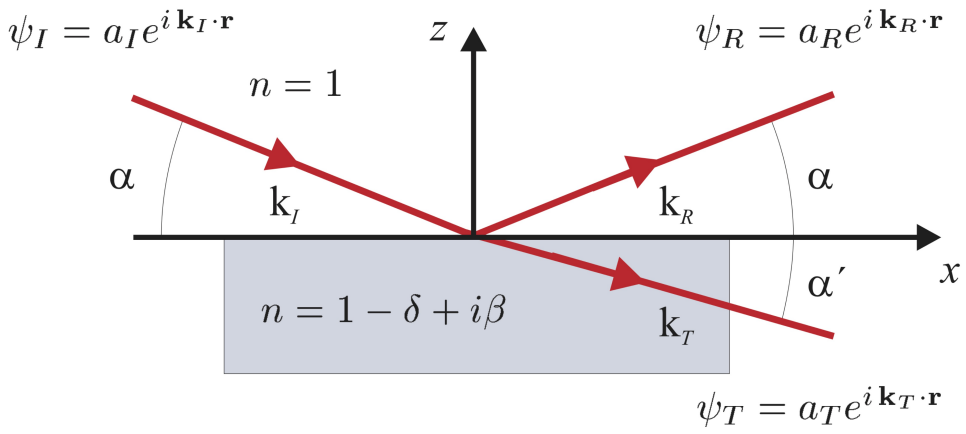


Figure 2.6: Snell's law and the Fresnel equations relate the incident wavevector k_I impinging on a sample surface at a grazing angle α to the reflected and refracted waves, occurring at angles α and α', splitting into a reflected wave at α and a refracted wave transmitted at α', respectively. Adapted from [20, 23].

grazing angle α and the refracted angle α' is governed by Snell's law and can be as written as

$$n_1 \cos\alpha = n_2 \cos\alpha' \tag{2.23}$$

Since the X-ray refractive index is slightly less than 1, total external reflection occurs for all incident angles α_i below a certain level. This level is called the critical angle α_c, and it is defined by the relation $\cos\alpha_c = n$. Neglecting absorption and using a Taylor expansion for small angles, the critical angle can be approximated as

$$\alpha_c \approx \sqrt{2\delta} = \lambda\sqrt{\frac{r_e \rho_e}{2\pi}} \tag{2.24}$$

By measuring this critical angle α_c at X-ray energies away from absorption edges, one can directly determine the electron density ρ_e and, therefore, the mass density ρ_m of the material with high accuracy.

To quantify this specular reflected intensity, the Fresnel equations are introduced. For an ideal, perfectly flat interface between two media, the reflection (r) and transmission (t) coefficients can be derived. By assuming elastic scattering ($|\mathbf{k}_i| = |\mathbf{k}_f| = k$) and applying the small-angle approximation ($\alpha \ll 1$) for grazing incidence geometry, these coefficients simplify to

$$r = \frac{\alpha - \alpha'}{\alpha + \alpha'} \tag{2.25}$$

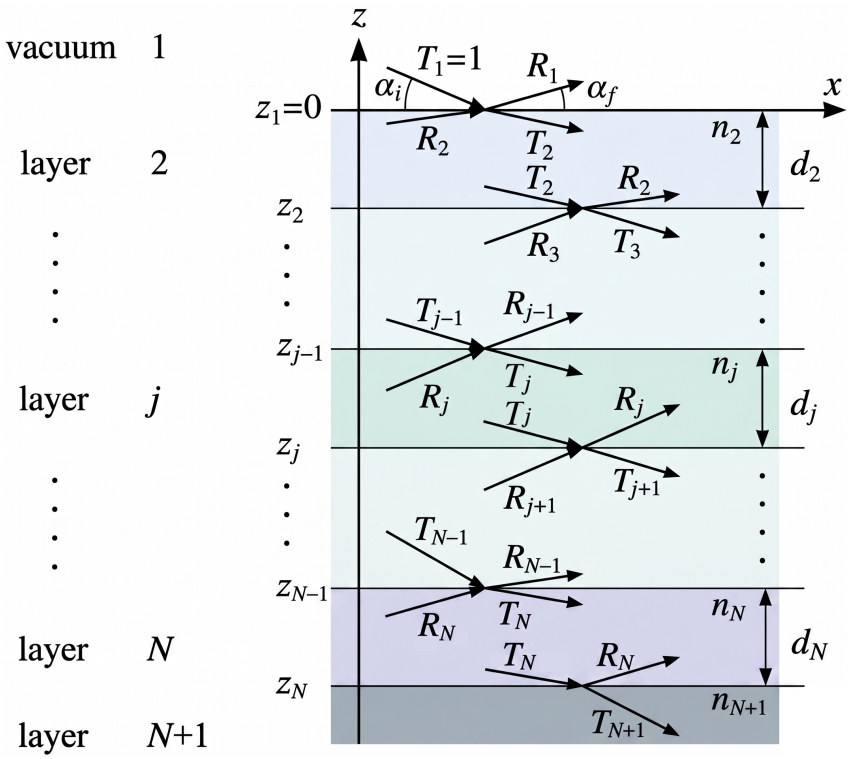


Figure 2.7: Schematic diagram of a multilayer transmission and reflection model consisting of $j+1$ layers and N interfaces. Redrawn from [23].

$$t = \frac{2\alpha}{\alpha + \alpha'} \tag{2.26}$$

where α and α' represent the incident and transmitted grazing angles, respectively. In real materials, the sample is rarely a single semi-infinite medium. Instead, it typically consists of a multi-layer structure with depth-dependent electron densities. When an X-ray beam penetrates such a stack, part of the wave is reflected and part transmitted at each interface between consecutive layers $j-1$ and layer j, as illustrated in Figure 2.7. The experimentally observed reflectivity results from the interference between all these reflected waves. The relative phases of these contributions depend on the path length differences, which are determined by the layer thicknesses and the refractive indices of the individual layers. As a consequence of these varying phase shifts, the reflected waves interfere constructively and destructively as the incidence angle is changed. This interference produces the characteristic oscillatory reflectivity pattern known as Kiessig fringes. [24]

To determine the total reflectivity of these multilayers, the Parratt formalism [25] is commonly introduced. The total reflection coefficient $R_{j-1,j}$ at the interface between the $(j-1)$-th and j-th layer is expressed as

$$R_{j-1,j} = \frac{r_{j-1,j} + R_{j,j+1}e^{2ik_{z,j}d_j}}{1 + r_{j-1,j}R_{j,j+1}e^{2ik_{z,j}d_j}} \tag{2.27}$$

where d_j is the thickness of the j-th layer, and $k_{z,j}$ is the perpendicular component of the wavevector in the specific medium, given by:

$$k_{z,j} = k_0\sqrt{\sin^2\alpha_i - 2\delta_j - 2i\beta_j} \tag{2.28}$$

$$r_{j-1,j} = \frac{k_{z,j-1} - k_{z,j}}{k_{z,j-1} + k_{z,j}} \tag{2.29}$$

This calculation starts at the bottom interface, where layer N meets the semi-infinite substrate $(N + 1)$. Here, the transmitted wave is assumed to be fully absorbed, so no further reflection occurs, which sets the boundary condition $R_{N,N+1} = 0$. The reflectivity is then propagated upward through the multilayers to the top surface. The ideal Parratt formalism assumes perfectly sharp interfaces. To include real surface roughness σ, a Gaussian model for the height fluctuations along the surface normal (the z-axis) is introduced

$$g(z) = \frac{1}{\sqrt{2\pi}\sigma_j}\exp\left(-\frac{z^2}{2\sigma_j^2}\right) \tag{2.30}$$

where σ_j is the roughness of interface j. This statistical height variation smears the electron density gradient, subsequently dampening the reflected intensity. The ideal Fresnel reflection coefficient $r_{j-1,j}$ is modified by

$$\tilde{r}_{j-1,j} = r_{j-1,j}\exp\left(-2k_{z,j-1}k_{z,j}\sigma_j^2\right) \tag{2.31}$$

By fitting experimental XRR curves to this theoretical approach, which is often carried out with specialized software such as FEWLAY or GenX, [26, 27] and by using X-ray optical constants from databases such as the Center for X-ray Optics (CXRO), [28] the model parameters can be extracted. In particular, layer thicknesses, electron densities, and interfacial roughness profiles of the investigated thin films and substrates can be determined with high accuracy.

2.2 Low-Energy Electron Diffraction (LEED)

Low-energy electron diffraction (LEED) is a standard technique for analysing the atomic arrangement and crystalline order of surfaces, including the structure of others adsorbates.

When low-energy electrons impinge on a surface, their strong interaction with matter restricts their penetration to only a few atomic layers. As a result, the resulting diffraction pattern contains highly surface-specific structural information. Unlike SXRD, LEED can be carried out relatively quickly using a compact laboratory instrument under UHV condition, and it allows efficient sampling of a wide portion of the surface reciprocal space. These benefits make LEED a practical tool for routine surface characterization. However, the sample must be sufficiently conductive to prevent charging effects during electron irradiation. A fundamental premise of LEED is the wave-like nature of electron. According to the de Broglie hypothesis, an incident electron with momentum p behaves as a matter wave with a wavelength λ_e that is inversely proportional to its momentum. This relationship is expressed as

$$\lambda_e = \frac{h}{p} = \frac{h}{\sqrt{2Em_e}} \tag{2.32}$$

where the momentum p, the kinetic energy E (typically 20 - 500 eV), the electron mass ($m_e = 9.109 \times 10^{-31}\ kg$) and the Planck constant ($h = 6.626 \times 10^{-34}\ Js$). This leads to electron wavelengths λ_e of around 0.5 - 3 Å, which is in the range of atomic distances and the condition for electron diffraction can be satisfied. [29] Since this energy scale is several orders of magnitude smaller than the rest mass energy of an electron ($m_e c^2 \approx 511$ keV), the electron velocity remains well below the speed of light ($v \ll c$). Consequently, relativistic effects are negligibly small, and the non-relativistic approximation can be safely applied. While fulfilling this wavelength condition makes electron diffraction similar to X-ray diffraction. The fundamental difference between LEED and XRD lies in the interaction strength between the probing wave and the solid. Unlike X-rays, which interact weakly and penetrate deeply, electrons are charged particles and interact strongly with the Coulomb potentials of atomic nuclei and electron clouds.

Due to this strong interaction, incident electrons not only undergo multiple elastic scattering events within the top few atomic layers, but they also frequently undergo inelastic scattering events (such as plasmon excitation or electron-hole pair generation), rapidly losing their kinetic energy. Only the electrons that scatter elastically maintaining their initial energy contribute to the sharp diffraction spots observed in LEED. The characteristic distance an electron can travel through a solid before an inelastic collision occurs is defined as the inelastic mean free path, typically denoted as λ_n as Figure 2.8 shown. [29] This attenuation of

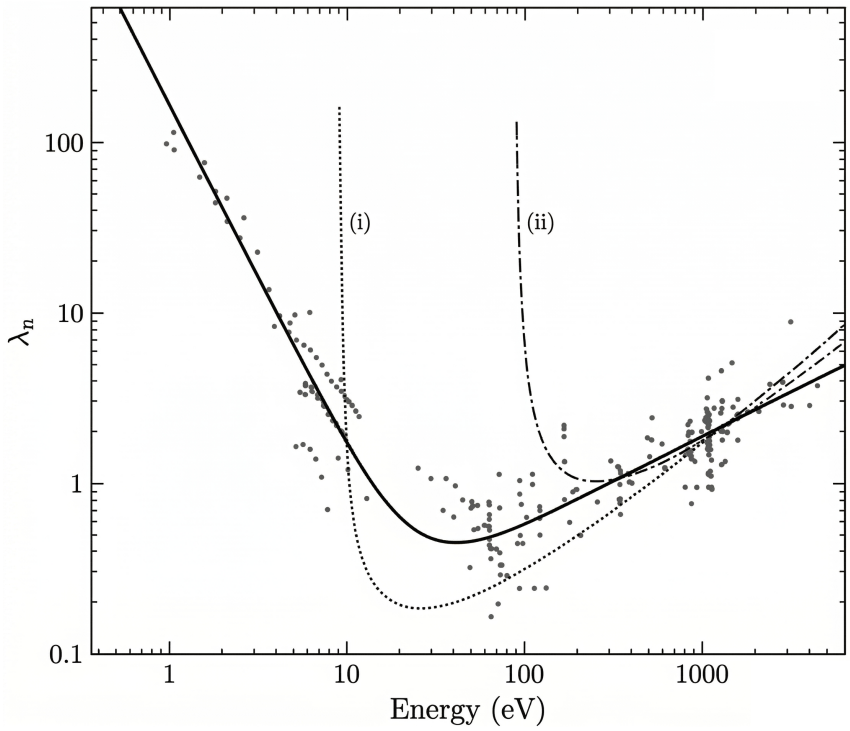


Figure 2.8: Energy-dependent experimental mean free path lengths of electrons in various materials. A universal minimum occurs at electron kinetic energies of around 100 eV, where the mean free path is typically below 1 nm. The dashed curves represent theoretical models from the original study: (i) represents Penn's theoretical relation using mean parameter values, [30] and (ii) represents the least squares fit to the experimental data for energies above 150 eV. Adapted from [29].

the elastically transmitted intensity I as a function of depth d follows an exponential decay,

$$I = I_0 e^{-\frac{d}{\lambda_n}} \tag{2.33}$$

where I_0 is the initial intensity. As demonstrated by the universal curve of the mean free path length, [29] for the typical LEED energy range (30 - 200 eV), λ_n reaches a minimum of merely a few Å. This extremely short probing depth is what gives LEED its exceptional surface sensitivity, ensuring that the measured structural information originates almost exclusively from the outermost atomic layers.

Figure 2.9(left) illustrates the schematic of a typical LEED experimental setup. [31] An electron gun generates a highly monochromatic beam of low-energy electrons, which is directed at the sample under surface normal incidence. The incident electrons are then elastically backscattered from the sample surface toward a hemispherical fluorescent screen. When the electrons strike the screen with sufficient energy, they excite the phosphor and cause it to fluoresce, making the diffraction pattern visible.

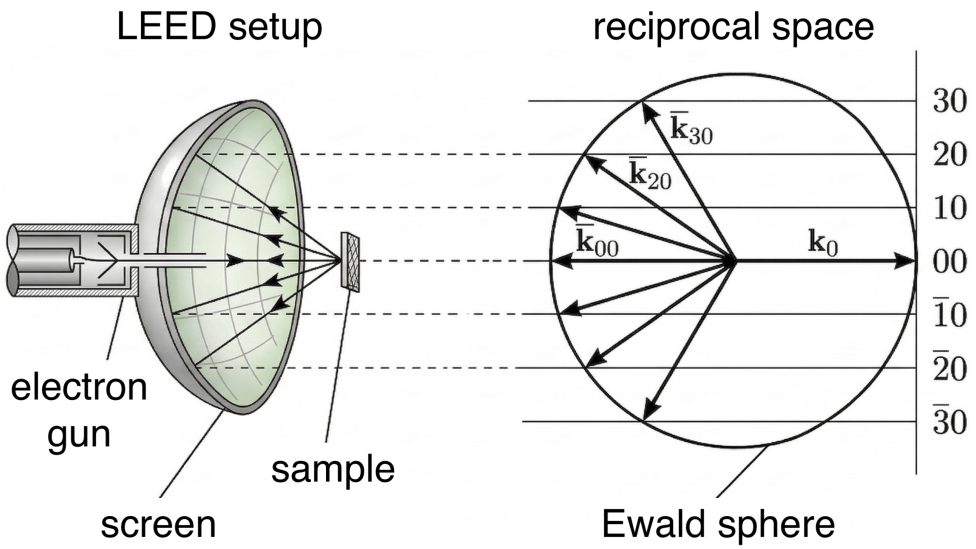


Figure 2.9: Overview of a LEED setup in real space and its corresponding Ewald sphere representation in reciprocal space, showing the crystal truncation rods indexed by (h, k). Adapted from [31].

The corresponding kinematic scattering process can be visualized in reciprocal space using the Ewald-sphere construction, as illustrated in Figure 2.9 (right). [31] The radius of the Ewald sphere is given by the magnitude of the incident electron wave vector $\mathbf{k}_0$. Three-dimensional periodicity of the bulk crystal is interrupted at the surface, the discrete reciprocal lattice points characteristic of an ideal crystal are extended along the surface normal, forming continuous one-dimensional features known as crystal truncation rods (CTRs). The diffracted beams, which appear experimentally as discrete spots on the fluorescent screen, occur precisely at the intersections where the Ewald sphere cuts through these rods ($\bar{3}0, \bar{2}0, \bar{1}0, 00, 10, 20 \ldots$). Moreover, the profile of these rods is highly sensitive to the surface morphology. An ideally flat and perfectly ordered surface lattice produces narrow CTRs, which translate experimentally into well-defined, sharp, and intense diffraction spots on the fluorescent screen. However, surface imperfections such as atomic step edges, point defects, or domain sizes will cause reciprocal broadening of CTRs. Therefore, the sharpness and contrast of the resulting LEED pattern serve as a direct, indicator for overall crystalline quality of the sample surface. Furthermore, by employing high-resolution techniques such as Spot Profile Analysis LEED (SPA-LEED), the broadened profiles of these spots can be evaluated to extract quantitative information regarding specific surface defects and morphological parameters.

In this study, LEED patterns were used to evaluate the quality of the single-crystal surface following the surface-treatment step at approximately 400 °C, as shown in Figure 2.10. These measurements were carried out before the SXRD experiments to confirm that the surface was

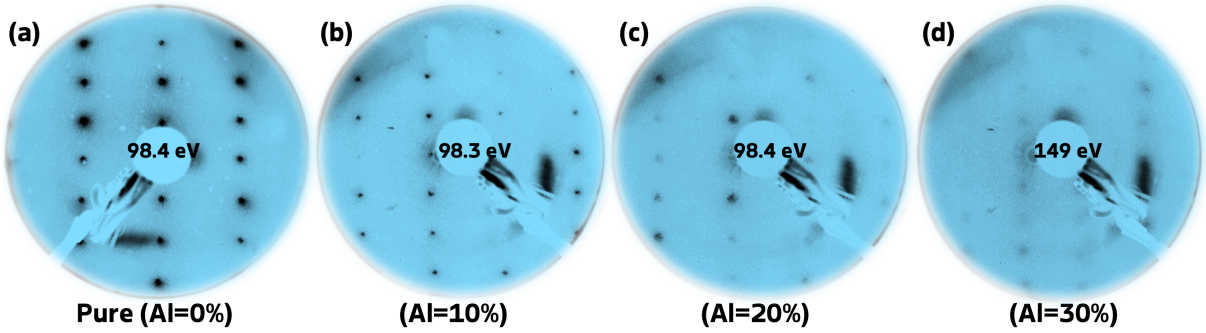


Figure 2.10: LEED patterns of (a) an as-cleaved β-Ga_2O_3(100) single crystal surface ($E = 98.4$ eV), and as-cleaved $(Al_xGa_{1-x})_2O_3$(100) single crystal surface with (b) $x = 0.1$ ($E = 98.3$ eV), (c) $x = 0.2$ ($E = 98.4$ eV), and (d) $x = 0.3$ ($E = 149$ eV). All patterns were acquired after oxygen annealing. With increasing Al content, the diffraction features become increasingly blurred, most likely due to charging effects.

sufficiently well ordered and thus suitable for reliable high-surface-sensitivity measurements.

2.3 Atomic Force Microscopy (AFM)

Atomic Force Microscopy (AFM) is an important technique for nanoscale surface characterization, enabling three-dimensional imaging with sub-nanometer resolution, as shown in Figure 2.11(a) (Bruker Dimension Icon), located at the DESY NanoLab. Unlike conventional optical or electron microscopy, it relies on a nanoscale ultra-sharp tip that physically probes the sample surface. As the tip approaches the surface, short-range interactions, so called van-der-Waals forces develop between atoms at the tip. These forces cause tiny deflections of the flexible cantilever holding the tip. To detect these nanoscale deflections, a laser beam is focused onto the reflective backside of the cantilever and then reflected onto a position-sensitive photo-diode. Even extremely small cantilever bending leads to a measurable shift in the reflected laser spot, effectively converting mechanical motion into an electrical signal. A feedback loop continuously adjusts the tip–sample separation to maintain a constant interaction force. As the tip scans laterally over the surface, a piezoelectric scanner finely modulates the vertical (z-axis) position of either the tip or the sample to keep the laser spot fixed on the detector. By recording these z-axis adjustments at each lateral (x,y) position, the AFM reconstructs a high-resolution, three-dimensional topographical map of the sample surface.

Depending on the nature of the tip–sample interaction and the material properties, AFM can be operated in three principal modes: contact, tapping, and non-contact. Morphology characterization of the as-cleaved gallium oxide single-crystal surfaces was carried out mainly

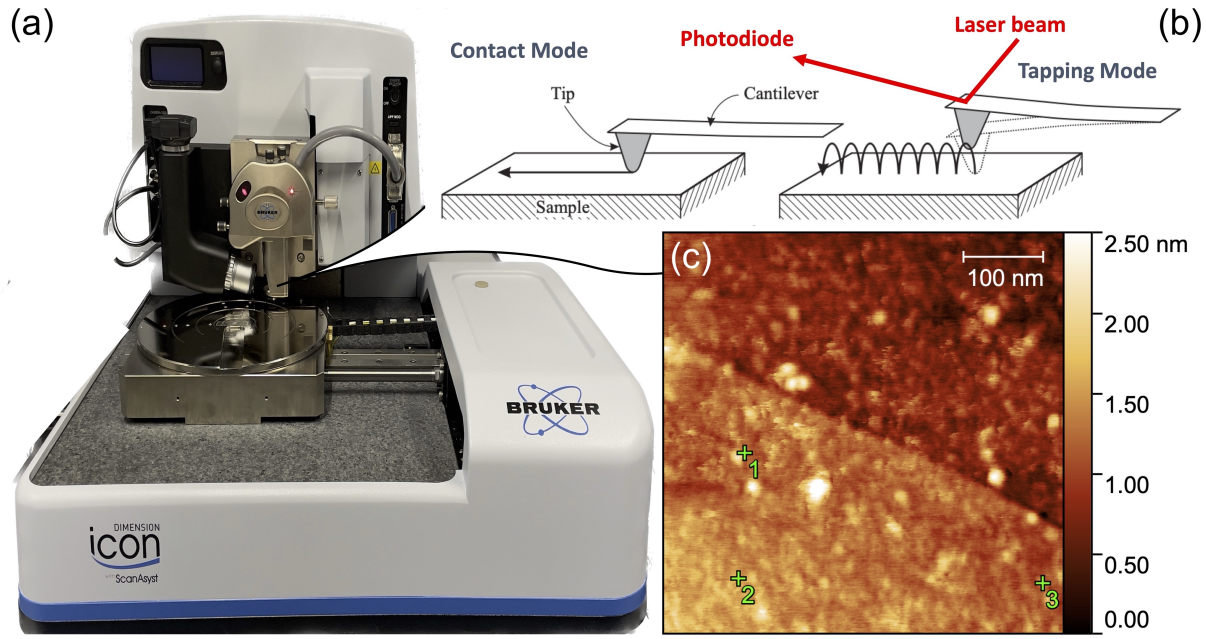


Figure 2.11: Atomic Force Microscopy (AFM). (a) Photograph of the AFM instrument (Bruker Dimension Icon) located at the DESY NanoLab. (b) Schematic illustrations of AFM operation in contact mode and tapping mode. (c) AFM image of an as-cleaved β-Ga_2O_3 single-crystal surface. The schematic illustrations have been adapted and modified from [32].

using tapping mode. Because the freshly cleaved surfaces exhibit delicate step-terrace structures at the atomic scale, operating in conventional contact mode would lead to rapid wear of the cantilever tip and introduce significant lateral forces. These forces could distort or damage the surface including the step edges, as illustrated in Figure 2.11(b). Tapping mode was therefore chosen as the optimal imaging technique. By minimizing lateral friction and operating in an intermediate-contact regime, it enables non-destructive mapping of the cleaved surface morphology. This approach allowed reliable visualization of the characteristic features of the cleavage surfaces and the atomically smooth terraces. As shown in Figure 2.11(c), which depicts a typical cleaved gallium oxide terrace step, this method provided essential structural information for the diffraction measurements and surface analyses discussed later in this work.

2.4 Experimental Setups Overview

This chapter summarizes the experimental methods and data handling procedures used throughout this study. Part of LEED measurements, all AFM measurements and some precharatraization with XRD were carried out in the UHV, Microscopy, X-ray laboratories at the DESY NanoLab. [33] The synchrotron-based SXRD experiments were conducted at the SIXS beam-

line at the SOLEIL Synchrotron in France, [34] while the single-crystal X-ray diffraction (SCXRD) measurements were performed at the P24 beamline at PETRA III, DESY in Germany. [35]

Each subsection provides an overview of the respective instrumental setups, including beamline configurations, measurement strategies, and the specific sample preparation, environments used during data collection. The chapter concludes with a description of the data-acquisition workflow and the analysis procedures conducted to process, refine, analysis and interpret the diffraction data obtained from both synchrotron facilities.

2.4.1 Laboratories at the DESY NanoLab

The DESY NanoLab offers several techniques for cutting-edge surface characterization and UHV-based sample preparation. [33] This section summarizes the specific experimental setups used throughout this thesis. LEED measurements were conducted in the UHV laboratory, which provides controlled conditions for surface characterization. AFM images were acquired using atomic force microscopes in the microscopy laboratory. In addition, GIXRD and XRR measurements were carried out in the X-ray laboratory to pre-characterize the samples, ensuring optimal preparation and evaluation before the valuable synchrotron beamtime.

MBE II chamber (LEED)

The MBE II chamber at the DESY NanoLab is designed for sample preparation and in-situ surface characterization. In this study, several single-crystal surfaces were prepared and analyzed using its LEED function. The system operates at an UHV with base pressure of approximately 10^{-11} mbar and is equipped with precision leak valves for controlled dosing of preparation gases such as argon, oxygen, and hydrogen. A range of tools enables atomic-level surface preparation, an ion sputter gun for contaminant removal, an e-beam heating stage capable of annealing up to 1200 $^{\circ}C$, and integrated evaporators and a thermal cracker for atomic oxygen dosing. A UHV manipulator ensures accurate sample positioning during all preparation and analysis steps, as illustrated in Figure 2.12. In this work, the primary procedures performed before the beamtime were surface cleaning using an ultrasonic bath, annealing at 400 °C under an oxygen partial pressure of 10^{-6} mbar, and LEED characterization.

Microscopy Lab

The Microscopy Lab at the DESY NanoLab features a wide range of advanced surface methods instrumentation. This includes Scanning Auger Microscope (SAM), Focused Ion Beam (FIB), Scanning Electron Microscope (SEM), Optical Polarization Microscope, UHV Scanning Tun-

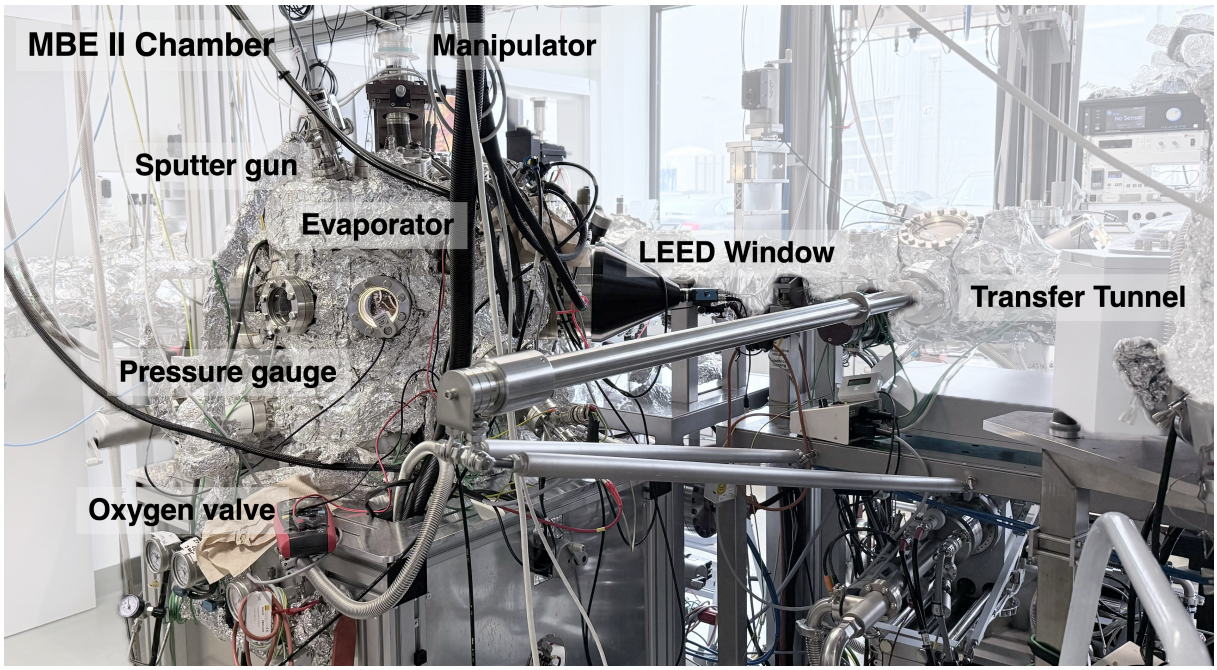


Figure 2.12: The MBE II chamber at the DESY NanoLab is used for surface characterization using LEED. [33]

nelling / Atomic Force Microscope (UHV STM/AFM), and a versatile high-resolution Atomic Force Microscope (AFM).

In this thesis, atomic force microscopy (AFM) was employed to characterize the surface morphology of the as-cleaved single crystal. The measurements were carried out using a Bruker Dimension Icon system, shown in Figure 2.11(a). This instrument is equipped with an XYZ closed-loop scanner that provides a maximum lateral scan range of 90 µm × 90 µm and a vertical range of up to 10 µm. Its exceptionally low drift rate (< 200 pm/min) and minimized noise floor enable highly precise three-dimensional imaging with sub-nanometer vertical resolution. NanoScope software was used for instrument control and initial data acquisition. Subsequent data processing and analysis of the AFM raw images were performed using Gwyddion, an open-source software package designed for the visualization and advanced analysis of scanning probe microscopy data. [36] In this work, Gwyddion was used to level the raw images and to extract the terrace profiles, as Figure 2.11(c) shown. Further data and the discussion of results will be presented in Chapter 4.

X-ray Lab

Surface pre-characterization for this study was carried out via SXRD and XRR in the X-ray Lab at the DESY NanoLab. This facility is equipped with several high-precision Huber diffrac-

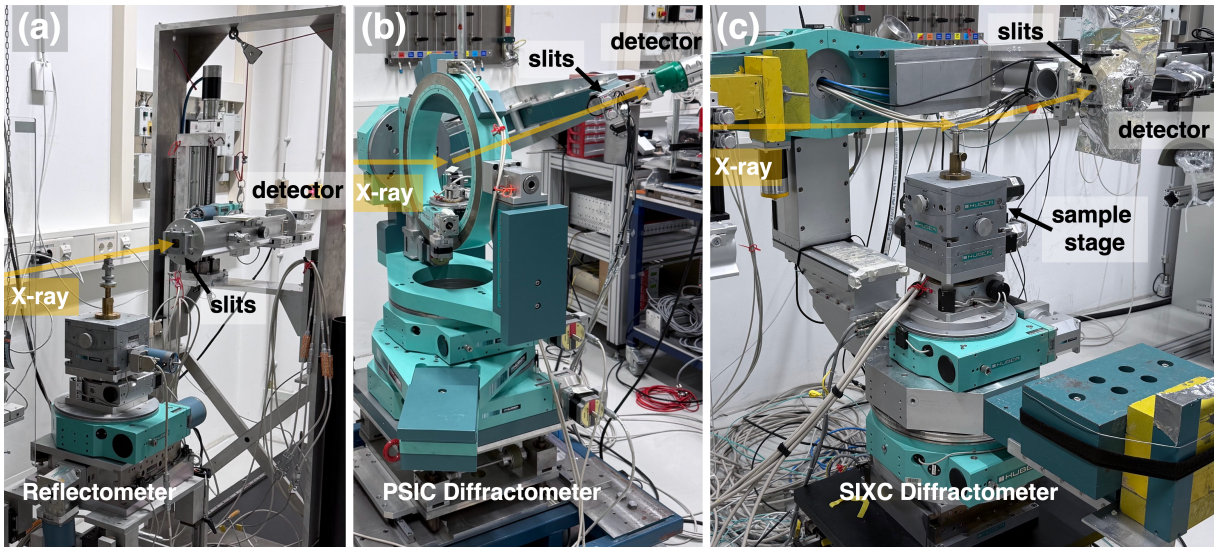


Figure 2.13: (a) Reflectometer, (b) PSIC diffractometer, and (c) SIXC diffractometer available at the X-ray laboratory of DESY NanoLab. [33]

tometers, including a Reflectometer (see Figure 2.13(a)) and two six-circle systems (the PSIC and the SIXC), as shown in Figure 2.13(b) and (c). The Reflectometer is optimized for standard θ-2θ scans and operates with a Mo-K_α source that provides a parallel beam with a spot size of 2×0.9 mm^2 (H $\times$ V). The PSIC diffractometer provides full reciprocal-space access using a Cu-K_α source. Both the Reflectometer and the PSIC are equipped with a point detector, and all instruments are controlled via SPEC.

X-ray pre-characterization measurements mentioned in this thesis were all carried out using the Six-Circle diffractometer (SIXC). It is designed to provide full access to reciprocal space, making it particularly well suited for advanced crystallographic investigations and detailed surface diffraction characterizations. The SIXC operates with a Cu-K_α X-ray source that produces a highly focused beam with a spot size of $0.25 \times 0.25\ mm^2$ (H $\times$ V) and a beam divergence of 5×5 mrad^2 (H $\times$ V). For data acquisition, the system is equipped with a Lambda 2D silicon detector featuring 256×256 pixels, corresponding to an active area of $14 \times 14\ mm^2$. This detector enables precise signal collection with minimal background noise.

2.4.2 SXRD beamtime at SIXS beamline (Soleil Synchrotron)

The experiments were conducted at the Surfaces and Interfaces X-ray Scattering (SIXS) beamline of the SOLEIL Synchrotron in Paris, France. [34] SIXS is dedicated to structural studies of surfaces, interfaces, and nanoscale systems using surface-sensitive X-ray scattering tech-

niques within an energy range of 5-20 keV. The beamline supports methods such as GIXRD, SXRD, CTR analysis, and XRR, allowing detailed investigations of crystalline surfaces and buried interfaces. The X-ray beam at the sample position offers a spot size of approximately $30 \times 30\ \mu m^2$ with a divergence of 600 µrad horizontally and 60 µrad vertically, and the photon flux reaches about 3×10^{12} photons per second at 15 keV, ensuring high-quality scattering measurements.

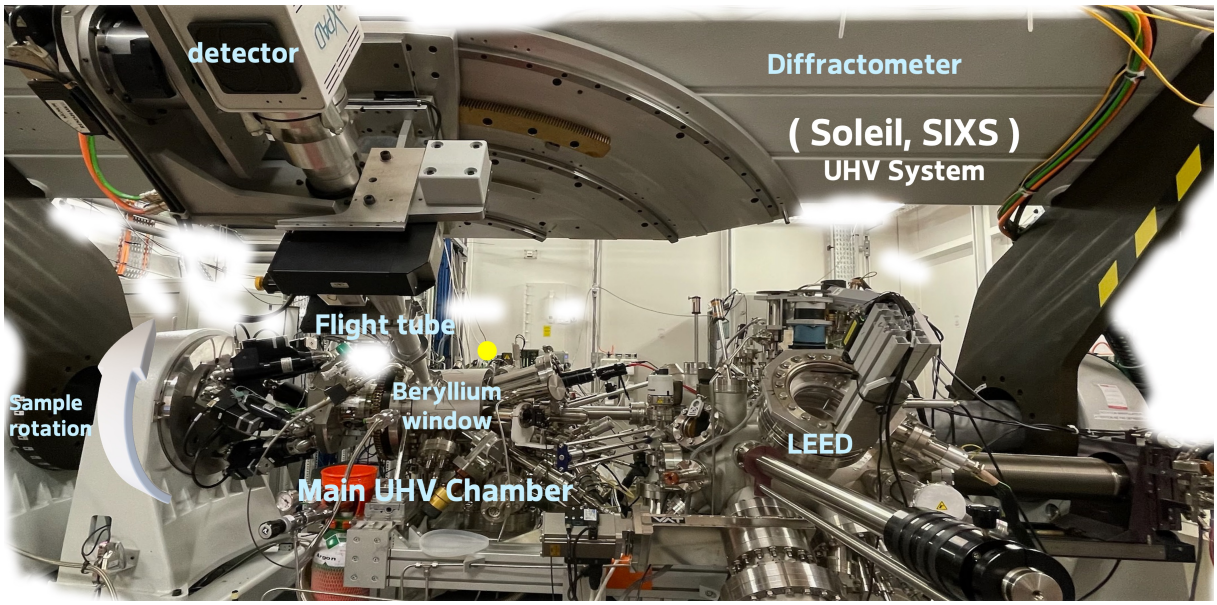


Figure 2.14: UHV hutch endstation at the SIXS beamline at the SOLEIL synchrotron. The UHV system is integrated into the large diffractometer, with the preparation chamber on the right side and the main chamber with the beryllium window for in-situ scattering measurements on the left. The X-ray beam enters from the direction indicated by the yellow dot.

Before the SXRD experiment, the as-cleaved bulk crystal was pre-characterized using LEED in the preparation chamber of the SIXS beamline. The sample was first annealed at 400 °C under an oxygen partial pressure of 10^{-6} mbar for one hour to remove surface contaminants. After this cleaning treatment, the crystal surface was examined by LEED over a range of electron energies to evaluate its structure and confirm the overall crystal quality. Once the surface order and cleanliness were verified, the sample was transferred under vacuum to the main SXRD diffraction chamber for further measurements.

For the CTR measurements, a photon energy of 18.42 keV was used in grazing-incidence geometry. All experiments were carried out in the dedicated UHV hutch, where the SXRD diffractometer is integrated into a stationary assembly of interconnected UHV chambers. This unique setup combines standard UHV chambers, including preparation chambers equipped

with heating stages and a transfer tunnel, with advanced surface-science instrumentation such as LEED and Auger Electron Spectroscopy (AES). This configuration enables complete in-situ sample preparation, characterization, and structural analysis without taking the sample out of the vacuum.

The main diffraction chamber enables in-situ sample heating up to 1000 °C and controlled oxygen dosing. Scattered intensities were recorded using a two-dimensional hybrid photon counting XPAD S140 detector, providing high sensitivity and low noise performance suitable for surface diffraction. Throughout all measurements, both the preparation and experimental chambers maintained pressures in the low 10^{-10} mbar range, ensuring stable and contamination-free conditions. A schematic overview of the SIXS UHV hutch, including the diffractometer and chamber assembly, is shown in Figure 2.14.

2.4.3 Crystallography beamtime at P24 beamline (PTERA III, DESY)

Single crystal X-ray diffraction (SCXRD) experiments were carried out at the P24 Chemical Crystallography beamline at PETRA III (Deutsches Elektronen-Synchrotron, DESY). [35] The measurements were performed in experimental hutch 1 (EH1), which is equipped with a high-precision Huber 4-circle Kappa diffractometer together with a Pilatus 1M CdTe detector for high-resolution data acquisition, as shown in Figure 2.15.

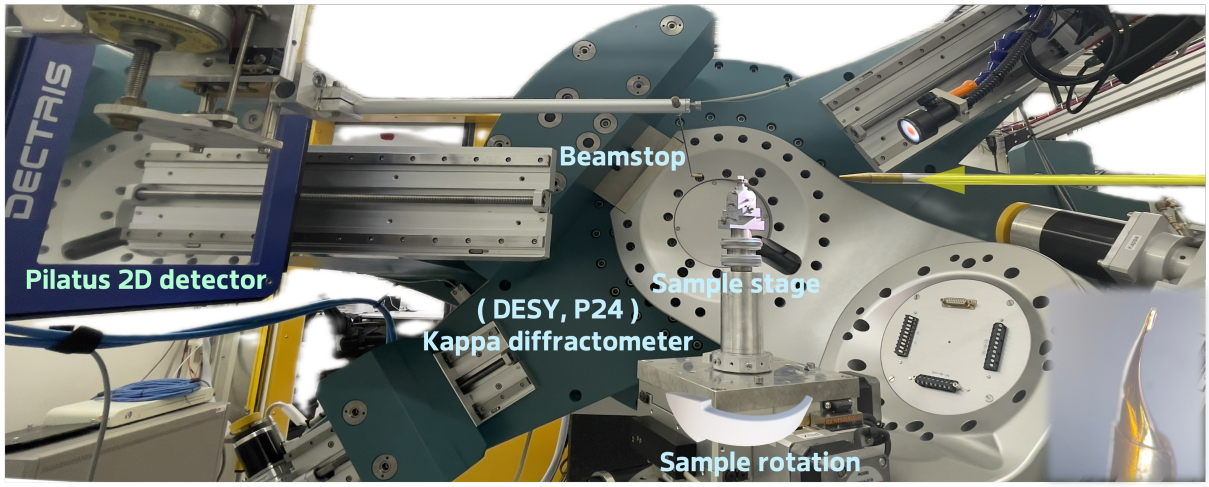


Figure 2.15: EH1 endstation at the P24 Chemical Crystallography beamline of PETRA III (DESY), equipped with a high-precision Huber four-circle kappa diffractometer and a Pilatus 1M CdTe detector for data collection. Bottom right: a β-Ga_2O_3 single crystal prepared to a size of approximately 40 x 40 μm, mounted on a Kapton-based sample loop using Paratone oil for single-crystal X-ray diffraction measurements.

During the beamtime, two primary experimental modes were carried out to investigate the

structural properties of β-$(Al_xGa_{1-x})_2O_3$ single crystals. First, SCXRD was conducted under ambient air conditions using an X-ray energy of 28 keV. This measurements investigated seven (100)-oriented β-$(Al_xGa_{1-x})_2O_3$ bulk single crystals with aluminum concentrations of 0 %, 5 %, 10 %, 15 %, 20 %, 25 %, and 30 %. Due to the microscopic diameter of the incident X-ray beam, dedicated sample preparation was required for this SCXRD measurements. The crystals were cut into cube-shaped specimens of approximately $40 \times 40\ \mu m$ and carefully mounted using Paratone oil onto Kapton-based sample loops from MiTeGen, as shown in the bottom right of Figure 2.15.

For further structural characterization, GIXRD was performed at an X-ray energy of 20keV to capture high-energy diffraction images. These measurements was conducted on a set of $(Al_xGa_{1-x})_2O_3$ thin films samples, all grown on a $5 \times 5\ mm$ pure β-Ga_2O_3 substrates with a thickness of 150 nm, and containing approximately 5%, 8%, and 18% Al in the thin-film. The pure β-Ga_2O_3 (100) substrates featuring a 2° miscut substrate and the other on a 4° miscut substrate. Finally, the pure and Al = 30% bulk single crystals without miscut were also measured under GIXRD geometry (see Figure 2.16) to provide a comparative structural analysis between the bulk and thin-film samples.

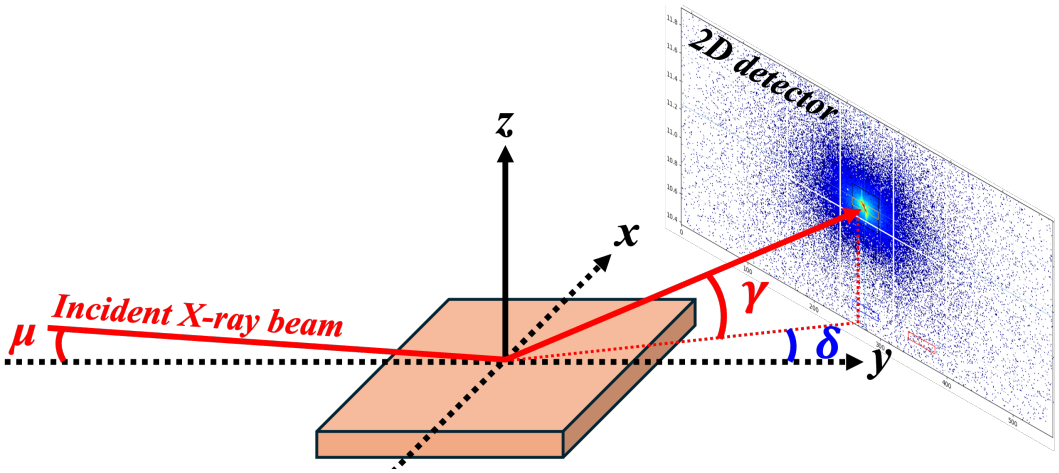


Figure 2.16: Schematic of the GIXRD geometry. μ denotes the grazing incidence angle of the incoming beam with respect to the sample surface (the xz plane), while δ and γ the detector in-plane and out-of-plane angles with respect to the surface normal (z axis).

2.5 Data Acquisition and Analysis Workflows

2.5.1 Surface X-ray Diffraction Data Processing and Analysis

BINoculars Software for Data Reduction

BINoculars is a tool for data reduction and analysis of large sets of surface diffraction data that have been acquired with a two-dimensional X-ray detector. [37] The intensity of each pixel of a two-dimensional detector is binned into a three-dimensional grid in reciprocal-lattice coordinates using a binning algorithm. This transformation converts the massive volume of raw detector images into a unified, 3D space indexed by the reciprocal lattice coordinates H,K, and L, where H denotes the surface normal direction and K and L denote the in-plane directions. Once this 3D volume is generated, the specific data processing workflow to extract the CTR profile proceeds as follows.

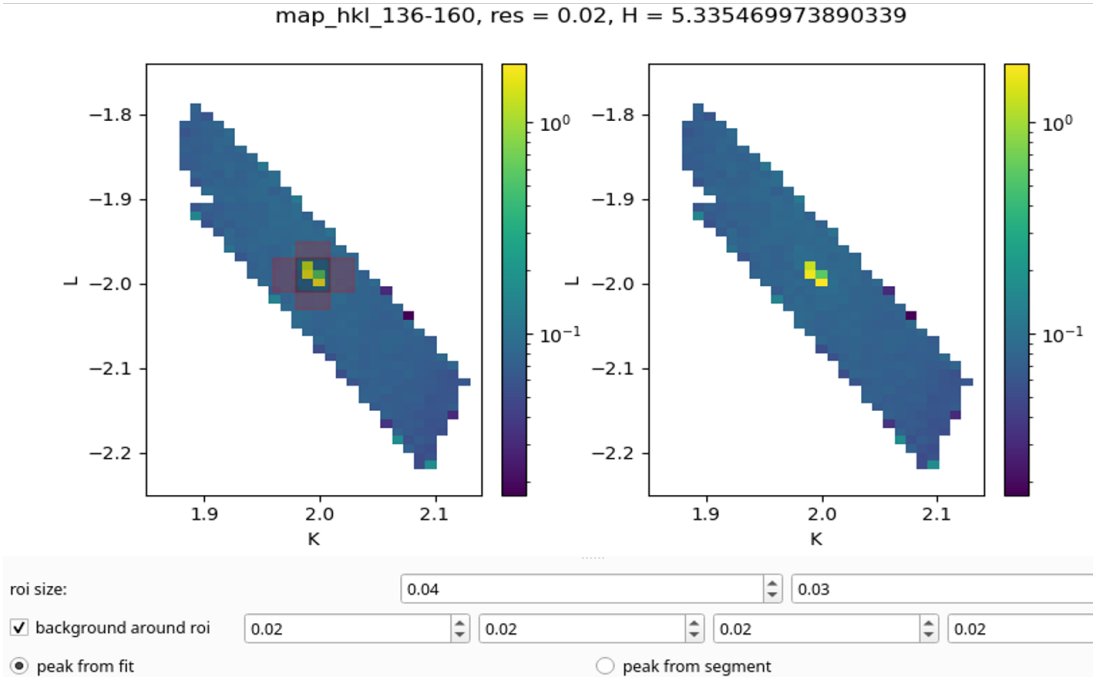


Figure 2.17: Peak integration and background subtraction using BINoculars. A two-dimensional reciprocal-space cross-section shows the defined ROI used for data extraction along the rod (K,L) = (2,2).

The 3D binned dataset was analyzed by extracting 2D cross-section slices at fixed H positions. In these (K, L) maps, localized regions of high X-ray intensity corresponding to the truncation rod were identified. To accurately quantify the true diffracted signal, it must be isolated from surrounding noise, such as air scattering or diffuse background. Figure 2.17 shows the GUI of BINoculars. A region of interest (ROI) is defined to tightly enclose the diffracted signal, including the Bragg peak and the CTR signal, while an outer bounding box is used to estimate the local background intensity.

Using the defined boundaries, the software performs a local background subtraction for the given slice. It calculates the average background intensity from the area between the

inner and outer boxes and subtracts this value from the pixels within the central ROI. The remaining, background-corrected signal is then integrated to determine the structure factor at the corresponding coordinate. The Lorentz correction (L) is strictly required following this integration to compensate for geometric distortions arising from the transformation between detector angles and reciprocal space. For our specific diffractometer geometry where the sample is mounted vertically, the incidence angle is μ, the in-plane detector angle with respect to the sample surface is δ, and the detector angle along the surface normal is γ, as demonstrated in Figure 2.16. The Lorentz factor would conventionally be expressed as

$$L = \frac{1}{\sin(\delta)\cos(\mu)\cos(\gamma)} \tag{2.34}$$

However, since the integration in this workflow is performed directly within the uniform 3D reciprocal-lattice grid (H, K, L) generated by BINoculars. As a result, geometric distortions arising from the experimental geometry are inherently accounted for during the binning process. Therefore, no additional explicit Lorentz correction is applied to the extracted intensities. Furthermore, to account for the horizontal polarization of the synchrotron beam, a polarization correction P_h is applied to compensate for the angular dependence of the scattered intensity.

$$P_h = 1 - [\sin(\mu)\cos(\delta)\cos(\gamma) + \cos(\mu)\sin(\gamma)]^2 \tag{2.35}$$

This ROI definition, background subtraction, and integration procedure is then repeated sequentially along the rod, in our case by varying the H coordinate. The resulting integrated

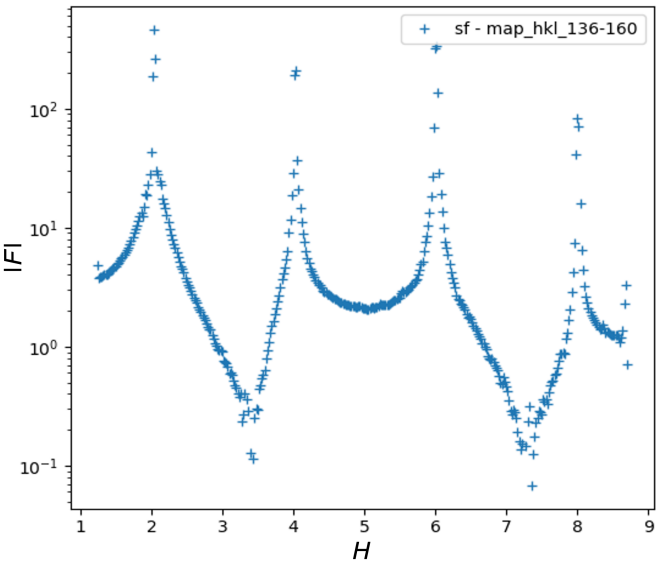


Figure 2.18: CTR Profile. The final output from BINoculars plotting the extracted structure factor as a function of the reciprocal lattice index (H). The sharp, high-intensity spikes correspond to bulk Bragg peaks, while the continuous curves connecting them represent the surface-sensitive truncation rod signals. Every data point reflects an individual integration step along the rod.

intensities are then plotted on a logarithmic scale as a function of reciprocal lattice index to generate the final CTR profile, as shown in Figure 2.18. This profile displays sharp bulk Bragg peaks connected by continuous, surface-sensitive scattering curves. This data reduction was performed directly after data collection at the SIXS beamline at the SOLEIL synchrotron. Finally, each corrected experimental structure factor data set was imported into the ANA-ROD program, where it was fitted against bulk structural models to determine the atomic surface crystal structure. [38]

CTRs Analysis with ANA-ROD

In this thesis, all the SXRD data were obtained from SIXS bealine, SOLEIL. Structural refinement of the SXRD data were performed using the ROD program. [39] The measurements of the β-Ga_2O_3(100) surface are referred to the bulk unit cell, described by the lattice parameters $a = 12.214$ Å, $b = 3.037$ Å, and $c = 5.798$ Å, with lattice angles $\alpha = \gamma = 90°$, and $\beta = 103.83°$ corresponding to the bulk [100], [010], and [001] directions, respectively. Before the fitting, the measured datasets were processed to determine error from merging using the AVE package from the ANA-ROD. By applying the $C2/m$ space group symmetry, the measurements were merged and sorted into their corresponding symmetry-equivalent families of CTRs, as summarized in Table 2.1. In this orientation, the in-plane momentum transfer is defined by the indices (K, L), while H represents the out-of-plane direction. As illustrated in the table, rods related by the symmetry operations of the $C2/m$ space group following the equivalence $(K, L) \equiv (-K, L)$ and $(K, -L) \equiv (-K, -L)$ are grouped into their respective structural families. Averaging these symmetrically equivalent measurements yields dataset, with uncertainties including systematic error from the experiment.

Table 2.1: Symmetry-equivalent CTRs grouped by in-plane momentum transfer families $\{K, L\}$ for the $C2/m$ plane group. The out-of-plane index is denoted by H.

Family $\{K, L\}$	Symmetry-equivalent rods $(H, -K, L)$
$\{2, 2\}$	$(H, 2, 2)$, $(H, -2, 2)$
	$(H, -2, -2)$, $(H, 2, -2)$
$\{2, 1\}$	$(H, 2, 1)$, $(H, -2, 1)$
	$(H, 2, -1)$, $(H, -2, -1)$
$\{0, 2\}$	$(H, 0, 2)$, $(H, 0, -2)$
$\{2, 0\}$	$(H, 2, 0)$, $(H, -2, 0)$
$\{0, 1\}$	$(H, 0, 1)$, $(H, 0, -1)$
$\{1, 0\}$	$(H, 1, 0)$, $(H, -1, 0)$

The momentum transfer vector $\mathbf{Q}$ is defined in reciprocal space as, $\mathbf{Q} = H\mathbf{a}^* + K\mathbf{b}^* + L\mathbf{c}^*$, where $H, K,$ and L are the momentum transfer indices expressed in reciprocal lattice units (r.l.u.). Due to the monoclinic symmetry of the unit cell ($\beta \neq 90°$), the magnitudes of the reciprocal lattice vectors a^* is geometrically defined as $2\pi/a\sin(\beta)$. The subsequent structural refinement optimizes several physical parameters, primarily atomic displacements, site occupancies, and the Debye-Waller (DW) parameter. Because the experimentally derived structure factors are on a relative scale, determined by the incident beam intensity and the effectively illuminated sample volume, a scale factor is applied to the calculated theoretical structure factors for each dataset. This overall scale factor is refined dynamically during the fitting process. The quantitative quality of the fit is evaluated using the reduced chi-squared metric, χ^2_{reduced}, defined as

$$\chi^2_{\text{reduced}} = \frac{1}{N-P}\sum \frac{(F_{\text{experimental}} - SF_{\text{theoretical}})^2}{\sigma^2} \tag{2.36}$$

where $F_{\text{experimental}}$ and $F_{\text{theoretical}}$ represent the experimental and theoretical-calculated structure factors, where S is the scale factor. σ denotes the experimental error associated with each data point (typically at 10 to 15%), N is the total number of data points, and P is the number of parameters in the structural model.

2.5.2 SC-XRD Data Integration and Analysis

Diffraction Refinement using Rigaku CrysAlis^{Pro}

The initial processing of the SC-XRD data obtained from the P24 beamline was performed using the Rigaku CrysAlis^{Pro} software. [40] The data collection was performed via a full 360° rotation scan, generating 1800 images at 0.2° intervals to ensure sufficient sampling of the Bragg peaks. Diffraction patterns were collected in air at room temperature utilizing a Pilatus 1M CdTe area detector with a pixel size of 172×172 μm^2. More details of the experimental method can be found in Chapter 2.4.3. Following this extensive data collection, the complete data reduction workflow was carried out, which including peak hunting, unit cell indexing, and the integration of reciprocal space. These software routines were systematically applied to all single crystal samples in order to determine the precise maximum momentum transfer (Q_{max}) and calculate the specific orientation matrix based on the known monoclinic crystal symmetry.

Following data collection, an advanced automated peak-extraction routine was used to

systematically identify Bragg reflections across the raw two-dimensional detector images. To maximize the extraction of valid reflections without introducing excessive background noise, a smart peak-hunting algorithm was employed, which typically increases the yield of localized diffraction spots by 20–30% compared to standard threshold. The extracted peaks were subsequently indexed to establish the orientation matrix. During this step, the unit cell determination algorithm calculated the best-fit lattice parameters. To optimize the indexing accuracy for the β-Ga_2O_3 samples, peak hunting was constrained by the expected monoclinic $C2/m$ space group symmetry. This step is important for determining the precise orientation matrix. Furthermore, the Ewald^{Pro}, a reciprocal space visualization tool was used to inspect the distribution of reflections in reciprocal space. Such visualization is particularly useful for verifying the overall accuracy of the unit cell indexing across the entire reciprocal volume. After that, the final data reduction was performed, and the fully reduced reflections were compiled and exported into a standard $*.hkl$ file. This final file contains the reciprocal-lattice indices (H, K, L), the corrected integrated intensities, and their corresponding errors, providing the essential quantitative dataset of unmerged reflections required for subsequent symmetry-averaging and surface structure refinement.

Finally, to specifically evaluate the diffraction features, the software's reciprocal-space viewer was used with the unwarp function to generate reconstructed projection images. This tool mathematically transforms the experimental images to reconstruct any desired 2D plane within reciprocal space. Furthermore, the software allows for the creation of integrative precession images by collapsing a thicker slice of reciprocal space into a single composite two-dimensional image. For the analysis of the β-Ga_2O_3 (100) crystal, these integrated unwarp images were critical. They permitted direct visualization and accurate assessment of the reciprocal lattice, making it possible to identify twin crystal. By thoroughly inspecting these 2D slices, this step ensured the correct assignment of intensities and the overall integrity of the data. The typical unwarp images are shown in Appendix A.3 with their corresponding experimental parameters, and are discussed in detail later in Chapter 3.4.5.

Chapter 3

Gallium Oxide - Crystal Structure, Growth, Surface Preparation

In this chapter, a brief overview is provided of the Gallium Oxide and its crystal and surface structure, including the relevant polymorphs of gallium oxide and their phase-transition behavior. The chapter then summarizes the single-crystal growth process based on the Czochralski method. The epitaxial relationship of MOVPE-grown $(Al_xGa_{1-x})_2O_3$ thin films on $4°$ miscut Ga_2O_3 (100) substrates is investigated using GIXRD. In addition, the structure factors of the possible surface terminations of the as-cleaved Ga_2O_3 (100) surface are simulated and further compared with the measured CTRs. Finally, single-crystal X-ray diffraction (SC-XRD) reveals twin domains / twinning within the prepared crystals, highlighting imperfections that complicate the subsequent data analysis.

3.1 Bulk Crystal Structure

Gallium oxide (Ga_2O_3) is highly polymorphic, with five primary crystalline phases experimentally confirmed: α (rhombohedral), β (monoclinic), γ (cubic), δ (cubic), and ϵ (hexagonal, often including κ as an orthorhombic subgroup). As illustrated in Figure 3.1, each polymorph possesses a distinct atomic unit cell structure. Among these, the β-phase is well established as the thermodynamically most stable modification, whereas the α, γ, δ, and ϵ phases remain metastable [41, 42].

Due to their metastable nature, the non-β polymorphs naturally tend to transform into β-Ga_2O_3 when thermal treatment is applied. As summarized in Figure 3.2 by Roy et al., [41] the phase transformation relationships and pathways among the different Ga_2O_3 polymorphs

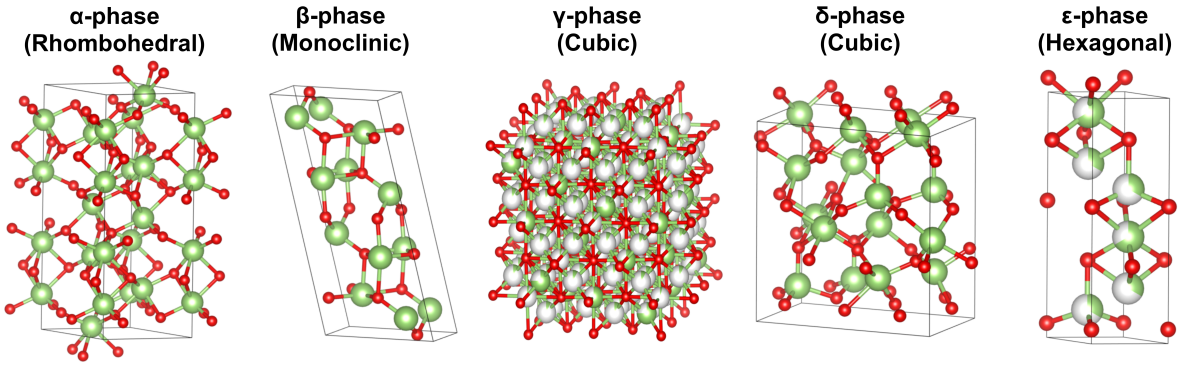


Figure 3.1: Atomic unit cells corresponding to the five known polymorphs of Ga_2O_3, with $\alpha, \beta, \gamma, \delta$ and ϵ occurring as metastable phases and β representing the thermodynamically stable form.

are described. In this pathway, the starting "Gels" refer to gallia-water complexes prepared by precipitating an aqueous solution of gallium nitrate with ammonia, which subsequently age into the gallic diaspore (GaO(OH)) structure. The figure highlights the specific thermal and environmental conditions, such as wet or dry atmospheres and the characteristic temperature thresholds that are required to drive these transitions from metastable phases toward the thermodynamically stable β phase. For example, the ϵ phase converts to the β phase at $870°C$ under dry conditions, while other metastable phases also transform into the β phase when heated to sufficiently high temperatures (for instance, above $> 500°C$ in dry environments or around $300°C$ in wet environments).

This polymorphic diversity offers not only a strong foundation for fundamental materials research but also flexibility for targeted device engineering. In practice, however, the thermodynamically stable β phase is the primary focus for most applications, while the other polymorphs are generally metastable and are explored mainly for their potentially distinct properties. These include the ultra-wide bandgap nature of Ga_2O_3, high breakdown fields, and, in some metastable phases, spontaneous polarization and more favorable lattice matching with certain epitaxial substrates. Together, these attributes continue to drive strong scientific and technological interest in β-Ga_2O_3 and support its growing role in next-generation high-performance electronic and optoelectronic devices. [12, 14, 16, 17]

3.2 Gallium Oxide β-Ga_2O_3 (100) Single Crystal

Beta-type gallium oxide (β-Ga_2O_3) is a transparent UWBG semiconductor, it has a monoclinic crystal structure with space group $C2/m$. The conventional unit cell contains four formula

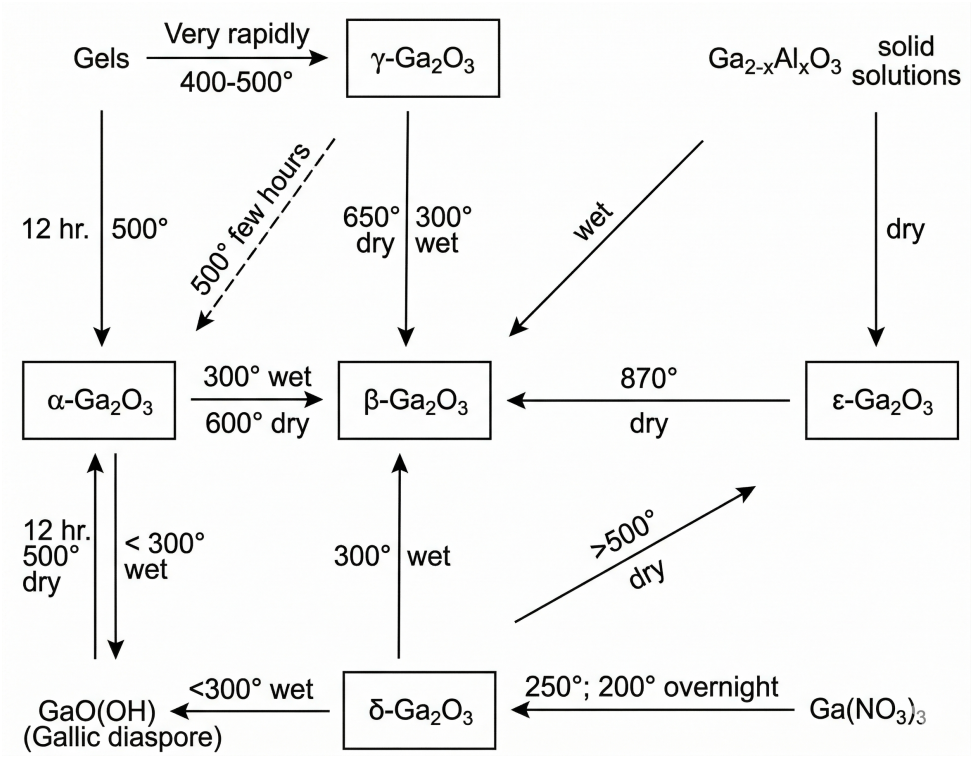


Figure 3.2: Phase transformation relationships and pathways among gallium oxide (Ga_2O_3) polymorphs and its hydrated precursors. The chart illustrates the specific thermal and environmental conditions driving the transitions from metastable phases ($\alpha, \gamma, \delta, \epsilon$) toward the thermodynamically stable β phase. For $Ga_{2-x}Al_xO_3$ solid solutions, wet conversion to β-Ga_2O_3 occurs only when x < 1.3. When x > 1.3, the material forms a β-Al_2O_3 type structure instead of converting to β-Ga_2O_3. Adopted from [41].

units, with gallium atoms (green) occupying both tetrahedral and octahedral coordination sites as shown in Figure 3.4(a). Figure 3.4(b) shows side views along the [100]/[010] directions, and Figure 3.4(c) presents the top view along the [010]/[001] planes. The lattice parameters are a = 12.214 Å, b = 3.037 Å, c = 5.798 Å, α = 90°, β = 103.83°, and γ = 90°. [42–44] Its corresponding fractional coordinates can be found in the Appendix A.1. [43] The high-quality β-Ga_2O_3 single crystals were grown using the Czochralski method, which will be introduced in a later section. These crystals were produced and provided by the Leibniz-Institut für Kristallzüchtung (IKZ) in Berlin, Germany. [18, 45]

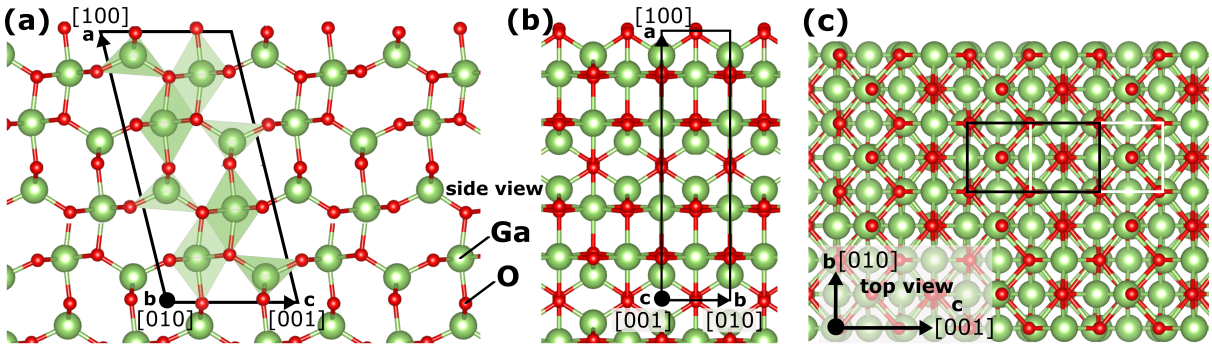


Figure 3.3: Conventional unit cell of β-Ga_2O_3(100). (a) and (b) show side views along the [100]/[001] and [100]/[010] directions, respectively, while (c) shows the top view along the [010]/[001] plane. Gallium atoms are shown in green and oxygen atoms in red.

Among all gallium oxide polymorphs, β-Ga_2O_3 is the thermodynamically most stable phase and the only one that can be grown from the melt. This capability allows the fabrication of large, high-quality bulk single-crystal substrates. Its melt-growth compatibility, together with its intrinsic structural stability and excellent suitability for power electronic devices, has made β-Ga_2O_3 the most widely studied and technologically important form of gallium oxide.

3.3 $(Al_xGa_{1-x})_2O_3$ (100) (x = 0-0.3) Single Crystals

Alloying β-Ga_2O_3 with aluminum to form β-$(Al_xGa_{1-x})_2O_3$ is an effective strategy for tuning the material's electronic properties and enabling precise band-gap engineering for high-power applications. As shown in Figure 3.4, the bandgap energy of $(Al_xGa_{1-x})_2O_3$ increases with Al composition, highlighting the strong portential of alloying for widening the gap across both monoclinic and corundum phases. [7, 15, 46–49] However, the crystallographic details of how

Al and Ga atoms incorporate into the monoclinic unit cell lattice structure remain incompletely understood, and the Al alloying behavior appears to be more complex than expected. In particular, the evolution of site-occupancy preferences and atomic positions. A deeper understanding of these structural characteristics is essential for advancing device fabrication processes, such as thin-film deposition and epitaxial growth. Precise knowledge of atomic configuration and lattice parameters enables accurate strain engineering and lattice-matching predictions, thereby minimizing interfacial defects in UWBG applications. The following section provides an overview of proposed structural models for Al-alloyed β-Ga_2O_3 based on first-principles studies, together with the PXRD-refined model. A more detailed discussion of the fitted and simulated structure factors, based on the Ordered and Non-ordered fractional atomic structures of the bulk models with Al contents of 10%, 20%, and 30% bulk models, as well as their as-cleaved (100) surface, is presented in Chapter 5.

Figure 3.5 illustrates the structural relationships between pure gallium oxide, theta-alumina (θ-Al_2O_3), and three proposed atomic configurations for a 20 % Al-alloyed single crystal. Pure β-Ga_2O_3 shown in Figure 3.5(a) and θ-Al_2O_3 shown in Figure 3.5(b) share the same isostructural monoclinic cell with a $C2/m$ space group, where the lattice constants for θ-Al_2O_3 are slightly smaller. Although the corundum phase (α-Al_2O_3) is the thermodynamically most sta-

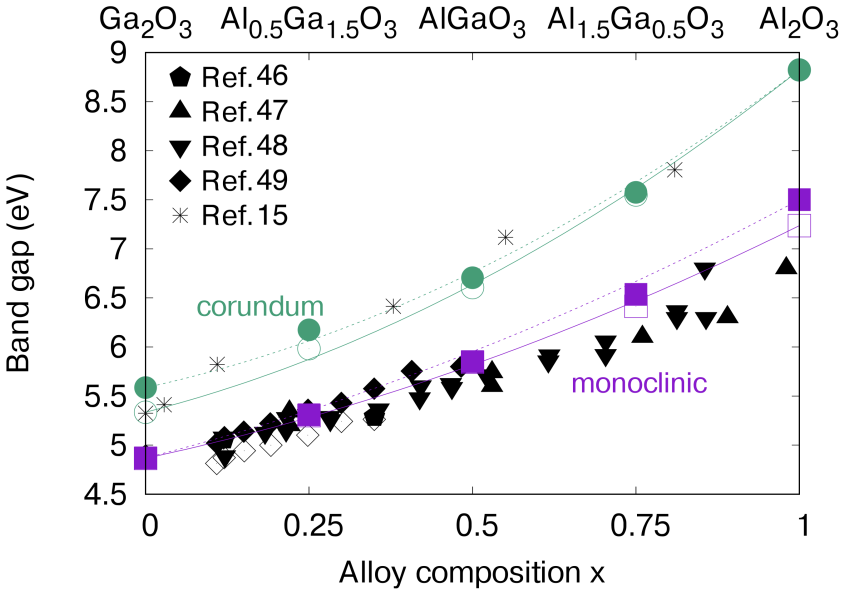


Figure 3.4: Bandgap energy (E_g) of $(Al_xGa_{1-x})_2O_3$ alloys as a function of the Al composition (x). Direct bandgaps are indicated by solid symbols and indirect bandgaps by open symbols for the monoclinic and corundum structures. Solid and dashed lines represent quadratic fits to the indirect and direct bandgaps, respectively. Computed values are shown in color, while experimental values are shown in black. [7, 15, 46–49] This figure is adopted from [7].

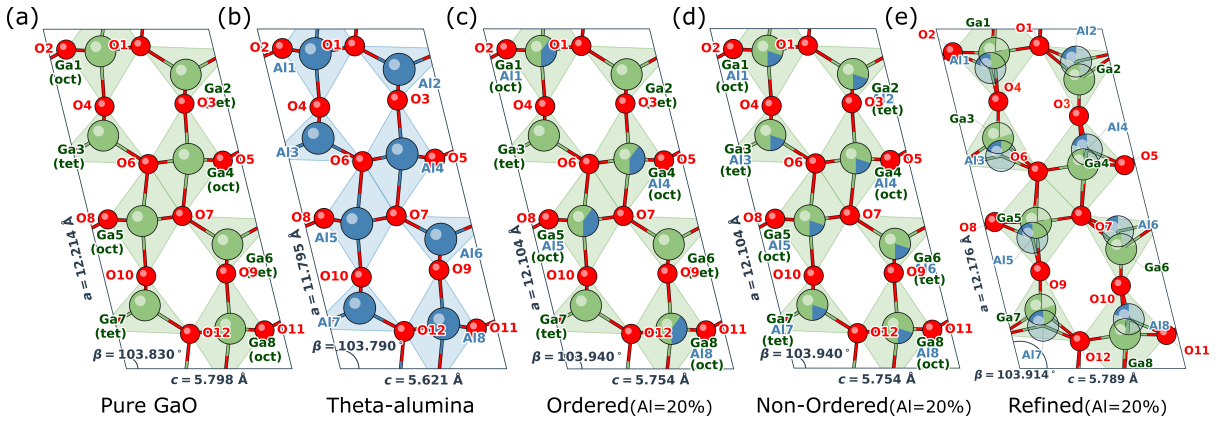


Figure 3.5: Crystallographic models of pure β-Ga_2O_3, θ-Al_2O_3, and three representative 20% Al-alloyed β-Ga_2O_3 structures. (a) Pure β-Ga_2O_3. (b) θ-Al_2O_3. (c) Ordered model with Al occupying only the octahedral sites. (d) Non-ordered alloy model with Al distributed over both octahedral and tetrahedral sites. (e) PXRD-refined model with Ga and Al located at their refined fractional coordinates. Al atoms are shown in blue, Ga in green, and O in red.

ble state of pure aluminum oxide, θ-Al_2O_3 is used as the theoretical fully Al-substituted case for this monoclinic alloy system.

Detailed first-principles studies demonstrate that Al atoms energetically prefer the octahedral sites over the tetrahedral sites in β-Ga_2O_3. This thermodynamic preference may initially seem counterintuitive, since the tetrahedral sites are physically smaller than the octahedral sites and the Al^{3+} ion is smaller than the Ga^{3+} ion. However, Al exhibits a strong chemical preference for six-fold octahedral coordination. As a result, Al preferentially occupies the octahedral sites, while the larger Ga^{3+} ions are forced into the smaller tetrahedral sites. For example, in a $(Al_{0.25}Ga_{0.75})_2O_3$ alloy, placing Al on the tetrahedral site is 79 meV higher in energy than occupying the octahedral site. [1, 7] Peelaers and co-workers also showed that for alloy concentrations below 71% Al, the monoclinic structure remains the most stable phase. They also found that up to 50% Al, Al preferentially occupies the octahedral sublattice in this structure. At exactly 50% Al composition ($AlGaO_3$), this strong site preference leads to a perfectly ordered structure where all octahedral sites are occupied entirely by Al atoms, and all tetrahedral sites are occupied entirely by Ga atoms. This strong site preference further explains the notably stability of the ordered model. [7] However, despite this strong thermodynamic preference, kinetic factors can block Al from reaching its lowest-energy configuration. Calculations of migration barriers reveal that an Al atom on the surface faces a substantial barrier of 1.72 eV to transition from a tetrahedral to an octahedral site, compared to only 0.56 eV for a Ga atom. Within the bulk crystal, Al mobility is even more restricted, making such migration

highly unlikely. [50] Together, these results indicate that although octahedral incorporation is energetically favored, Al can still become trapped on tetrahedral sites due to kinetic limitations during crystallization.

Figures 3.5(c), (d), and (e) illustrate three atomic models regarding the incorporation of Al in the crystal, presented here for the case of Al = 20% (x = 0.2). The Ordered model shown in Figure 3.5(c) indicated a strict site preference, with Al atoms only occupying the octahedral sites within the crystal structure. In contrast, the Non-ordered model presented in Figure 3.5(d) illustrates a statistical distribution, where Al atoms randomly substitute into both octahedral and tetrahedral sites. The PXRD-refined model shown in Figure 3.5(e) is based on experimentally refined data obtained from PXRD analysis performed by our colleague. In this refinement, the positions of the Ga and Al atoms were adjusted to their fractional coordinates. This model provides a more accurate, quantitative representation of the actual atomic positions within the crystal lattice. A first comparison with the pure GaO structure and the θ-Al_2O_3 reveals that Al_1 tends to sit slightly below Ga_1, while Al_2 preferentially positions itself slightly above Ga_2. These positional shifts are primarily driven by the difference in ionic radius between the two cations, as previously mentioned. In a purely ionic picture, due to the Al^{3+} ion is significantly smaller than the Ga^{3+} ion, its optimal metal-oxygen bond lengths are naturally shorter, while the smaller ionic radius of Al^{3+} reduces the average metal–oxygen bond length, any off-center displacement of the Al atom within the rigid octahedral oxygen cage consequently produces a distribution of both shorter and longer individual bonds.

Despite these proposed models, the exact crystallographic cooperation and structural arrangement of Al and Ga within the β-phase lattice remain ambiguous. Bridging this knowledge gap is a primary goal of this study. By investigating the exact crystallographic structuring of β-$(Al_xGa_{1-x})_2O_3$, we aim to clarify these fundamental site-occupancy behaviors. A comprehensive quantitative structural analysis based on experimentally measured CTR datasets, followed by an in-depth discussion of the resulting atomic models, will be presented later in Chapter 5.

3.4 Growth of High-Quality Crystals

The high-quality $(Al_xGa_{1-x})_2O_3$ (x = 0 - 0.3) single crystals investigated in this study were grown by Galazka et al. at the Leibniz-Institut für Kristallzüchtung (IKZ) in Berlin, Germany. [18,45] Maintaining a high level of crystalline perfection is essential for accurate surface-sensitive

scattering measurements and analysis, as well as for the epitaxial growth of thin films. The crystals were grown using the Czochralski (CZ) method, a traditional technique widely used in industry, such as for silicon wafer production. This method is a leading technology for producing large-diameter single crystals with high structural quality at low cost. Obtaining bulk $(Al_xGa_{1-x})_2O_3$ through this technique broadens the available crystal-growth technologies and enables the production of large, high-quality crystals that is suitable for epitaxial layer growth and advanced device fabrication. Comprehensive descriptions of the corresponding growth parameters for $(Al_xGa_{1-x})_2O_3$ single crystals can be found in numerous published studies. [18, 51–57]

3.4.1 Czochralski Method

The Czochralski (Cz) method, discovered in 1916 by Jan Czochralski, [58] originated from his accidental immersion of a pen into molten tin, which produced a thin metallic filament later identified as a single crystal. After World War II, Gordon Teal advanced the technique for industrial semiconductor production, [59] including early applications in laser technology. [57] Today, the Cz method is one of the most important and widely used bulk single crystal growth techniques in both research and the semiconductor industry, with its largest application being the production of silicon single crystals weighing several hundred kilograms and reaching diameters of up to 450 mm. More details about the achievement of Jan Czochralski can be found in this reference. [58]

A typical Czochralski method setup for β-Ga_2O_3 crystal growth is shown schematically in Figure 3.6. It consists of a water-cooled furnace that encloses an iridium crucible, which is heated by an RF induction coil. A (010)-oriented β-Ga_2O_3 seed crystal, aligned nominally on-axis, is fixed to a rotating pull rod equipped with a load cell. After the melt is brought to thermal equilibrium, the rotating seed is lowered until it contacts the molten oxide. When the melt wets the seed, the crystal is gradually withdrawn while rotation is maintained. The growth process is typically performed in an atmosphere of Ar, CO, and/or O at pressures between 1 and 7 bar. Crystal growth is carried out along the [010] direction, which is advantageous because it is parallel to the (100) and (001) cleavage planes. By precisely tuning the pulling speed, the seed is enlarged to the desired diameter and extended into a uniform cylindrical boule. Once the intended length is obtained, the crystal is separated from the melt and cooled down to room temperature. For monoclinic β-Ga_2O_3, this approach allows efficient production of large, high-quality boules that can be sliced into wafers of desired crystallographic

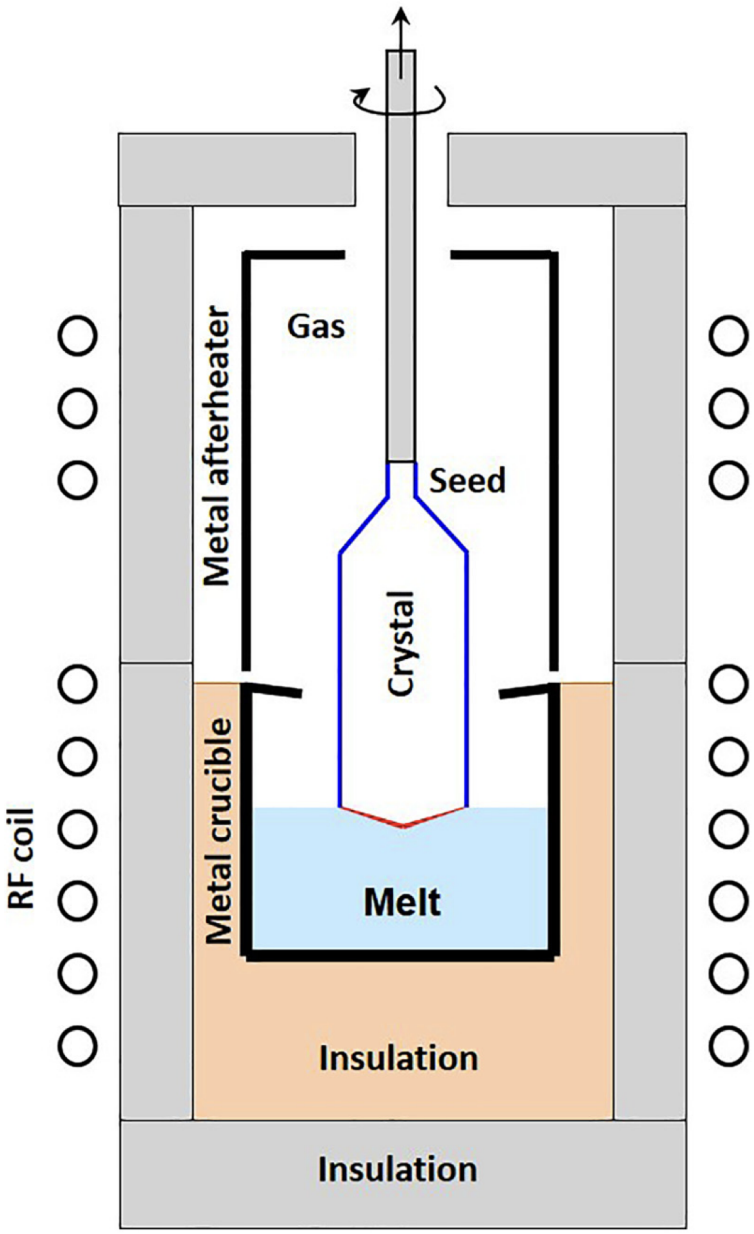


Figure 3.6: Schematic illustration of a general-purpose growth furnace used for producing high-melting-point oxide crystals by the Czochralski method. This figure is adapted from Galazka et al. (2022). [45]

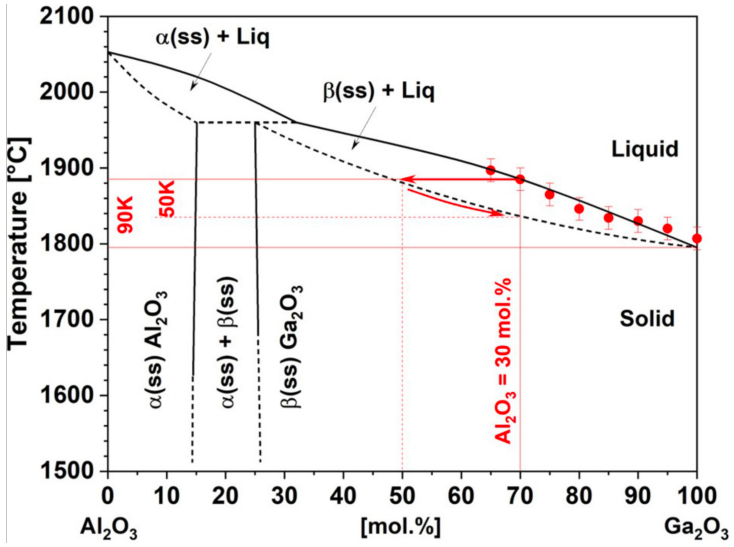


Figure 3.7: Phase diagram of the Ga_2O_3–Al_2O_3 system. The red points indicate experimentally measured melting temperatures of $(Al_xGa_{1-x})_2O_3$ during Czochralski growth. This figure is adapted from Galazka et al. (2023). [18]

orientation. [6]

However, applying this established method to β-Ga_2O_3 introduces significant thermodynamic challenges. Ga_2O_3 becomes thermally unstable as it approaches its melting point (around 1800 °C), and it tends to decompose at such elevated temperatures. As a result, careful control of the thermodynamic environment is essential for successful melt growth. During decomposition, Ga_2O_3 can form several volatile species, including O_2, Ga_2O, GaO, and Ga. Among these, Ga_2O exhibits the highest partial pressure at high temperatures. The relevant high-temperature gas-phase reactions can be given as follows [60]

$$Ga_2O_3(s) \rightarrow 2GaO(g) + \frac{1}{2}O_2(g) \tag{2.1}$$

$$2GaO(g) \rightarrow Ga_2O(g) + \frac{1}{2}O_2(g) \tag{2.2}$$

$$GaO(g) \rightarrow Ga(g) + \frac{1}{2}O_2(g) \tag{2.3}$$

$$Ga_2O_3(s,l) \rightarrow 2Ga(l,g) + 1\frac{1}{2}O_2(g) \tag{3.1}$$

where, s, g, and l denote to the solid, gas, and liquid phases, respectively. These decomposition pathways strongly influence melt stability, the crucible atmosphere, and ultimately the structural quality of the resulting crystal.

When transitioning from the growth of pure β-Ga_2O_3 to the alloy system β-$(Al_xGa_{1-x})_2O_3$,

the growth process becomes considerably more complex. The thermodynamic behavior of the alloy can be understood using the Ga_2O_3-Al_2O_3 phase diagram (see Figure 3.7). This diagram shows that the monoclinic structure remains stable up to approximately 60 to 70 mol% alumina. At the same time, the incorporation of aluminum leads to a systematic increase in the melting point. Growth experiments reported by Galazka et al. confirm this trend, as indicated by the red data points in Figure 3.7. These data indicate a melting temperature of approximately 1885 °C for melts containing about 30 mol% Al_2O_3.

A key feature of the phase diagram is the pronounced separation between the solid (dashed line) and liquid (solid line) phases, which creates a broad two-phase equilibrium region. At 30 mol% Al_2O_3, this solid–liquid gap can reach almost 50 K. Such a large separation promotes constitutional supercooling, causing the first crystallized material to incorporate more aluminum than the nominal melt composition. As indicated by the horizontal red arrow, crystallization from a 30 mol% melt initially. As this Al-enriched solid is removed, the melt becomes progressively depleted in aluminum. Crystallization then follows the liquid curve toward lower temperatures and reduced Al concentrations, shown by the downward red arc, producing a gradual decrease in aluminum content along the length of the grown boule. In contrast, in the lightly alloyed regime where the Al_2O_3 content is below about 10 mol%, the separation between the solid and liquid lines is much smaller. As a result, the difference between the aluminum concentration in the first crystallized material and in the melt is minimal. [18]

To confirm the aluminum content of the different single-crystal substrates, structural characterizations were carried out. XRR measurements performed at SOLEIL and SXRD collected at P24 beamline at DESY were used to analyze crystals grown with nominal Al concentrations of 0 %, 10 %, 20 %, and 30 %. By combining the fitted electron density and critical angle extracted from the XRR profiles with the refined lattice parameters determined from SXRD, the actual aluminum composition (x) in each crystal was accurately quantified. This result will be later introduce in Chapter 5.

3.4.2 Metalorganic Chemical Vapor Phase Epitaxy (MOVPE) Thin Films

Metalorganic Chemical Vapor Phase Epitaxy (MOVPE), a specialized form of the chemical vapor deposition (CVD). It was first introduced in the 1960s and later became a key epitaxial growth technique used to fabricate high-quality semiconductor layers with precise control over thickness, composition, and doping. [61] Its main advantages include excellent material uniformity, precise control of layer composition and doping, scalability for large-area sub-

strates, and suitability for complex multilayer structures. Therefore, MOVPE is widely used in industrial production since it offers high reproducibility and is compatible with many important semiconductor materials, including our $(Al_xGa_{1-x})_2O_3$.

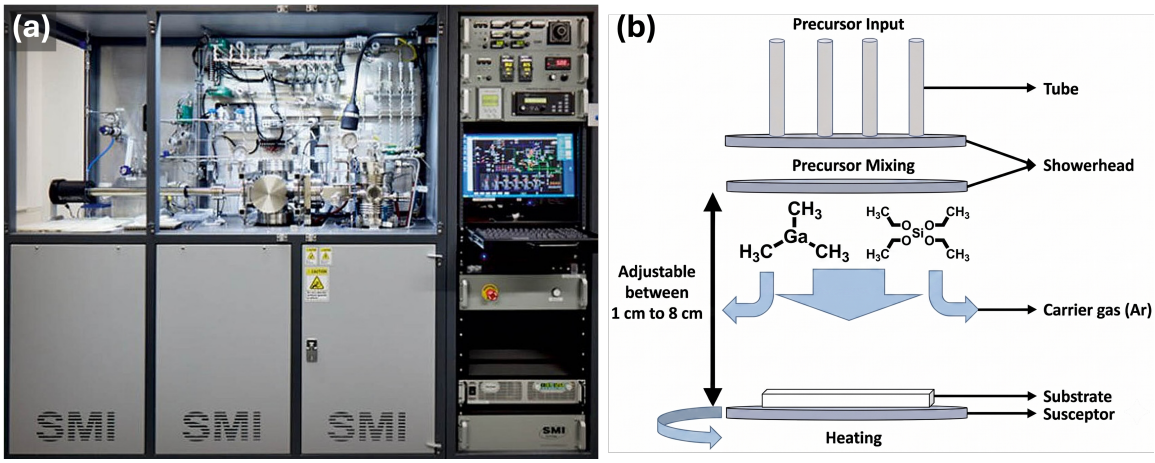


Figure 3.8: (a) An image of the MOVPE system used for the growth of $(Al_xGa_{1-x})_2O_3$ thin films equipped at the Leibniz-Institut für Kristallzüchtung in Berlin. [62] (b) Schematic drawing of the MOVPE growth chamber used for the deposition of our thin-film samples, this figure is taken from [63].

Figure 3.9(a) shows the MOVPE reactor (Structured Materials Industries, Inc., USA) equipped with a rotating susceptor used for the growth of $(Al_xGa_{1-x})_2O_3$ thin films, it located at the Leibniz-Institut für Kristallzüchtung in Berlin. The $(Al_xGa_{1-x})_2O_3$ thin films with the thicknesses around 150 nm were grown on Czochralski-grown (100)-oriented β-Ga_2O_3 substrates with the miscut of 4° toward $[00\bar{1}]$. High-quality β-Ga_2O_3 single crystals were grown by the Czochralski method by Leibniz-Institut für Kristallzüchtung (IKZ), from which CrysTec GmbH Berlin prepared (100) 4° off oriented substrates by applying a dedicated miscut, grinding, and chemical-mechanical polishing. As figure 3.9(b) shows, [63] the Schematic of the MOVPE growth of $(Al_xGa_{1-x})_2O_3$ thin films through precursor delivery, transport, and surface reaction. First, the Triethylgallium (TEGa) and tetraethyl orthosilicate (TEOS) were used as the metalorganic precursors for Ga- and Si-based n-type doping, respectively. Secondly, Oxygen (5N) served as the oxidant, while high-purity argon (5N) acted as the carrier gas. After transport through the reactor, the precursors diffuse through the boundary layer above the heated substrate, where they undergo pyrolysis and contribute to film growth on the substrate surface. The $(Al_xGa_{1-x})_2O_3$ layer layers were grown at temperatures between 800 to 830 °C, at chamber pressures ranging from 5 to 60 mbar, and with a showerhead-to-substrate distance of 8 cm in remote mode. [8, 64–66]

The MOVPE-grown thin-film samples were investigated at the P24 beamline using grazing-

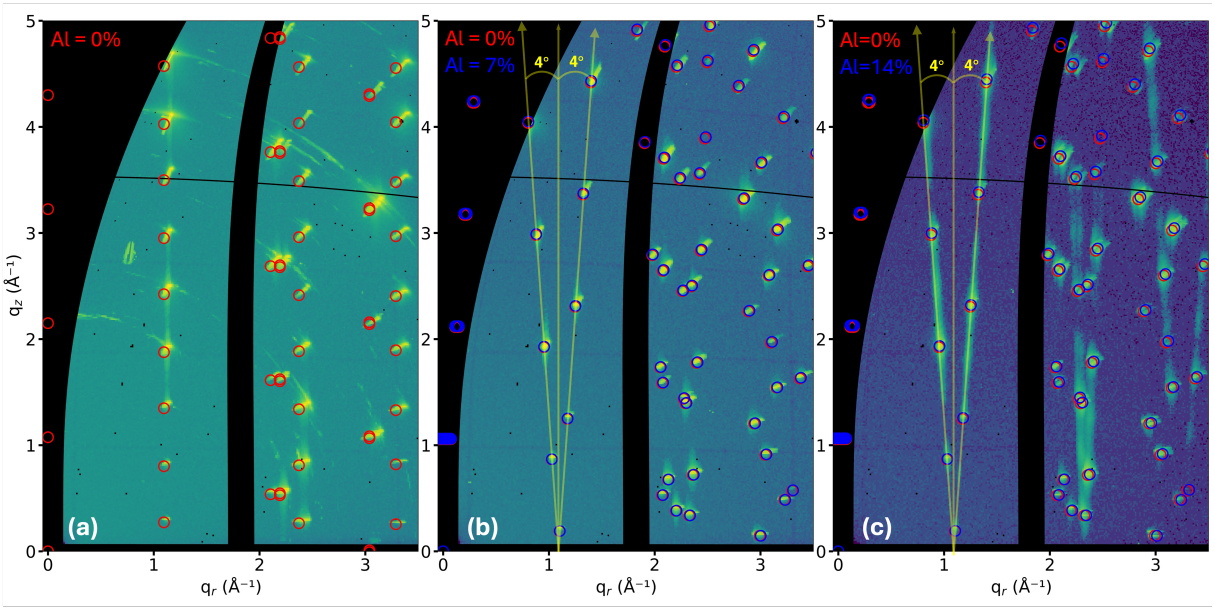


Figure 3.9: Diffraction image highlighting the pixel with the maximum intensity after a full 360° rotation, acquired at the P24 beamline using an X-ray energy of 20 keV. (a) β-Ga_2O_3 (100) single crystal substrate without miscut. (b) $(Al_xGa_{1-x})_2O_3$ with Al contents of 7% thin films grown on (100) β-Ga_2O_3 substrates with the miscut of 4°. (c) $(Al_xGa_{1-x})_2O_3$ with Al contents of 14% thin films grown on (100) β-Ga_2O_3 substrates with the miscut of 4°. The red circles indicate the simulated Bragg positions of the β-Ga_2O_3, and the blue circles indicate the Bragg positions of the $(Al_xGa_{1-x})_2O_3$.

incidence geometry with a 20 keV X-ray beam. Figure 3.9 shows the maximum pixel images (MPI) for (a) a β-Ga_2O_3 (100) single-crystal substrate without miscut, (b) an $(Al_{0.07}Ga_{0.93})_2O_3$ thin film grown on a (100) β-Ga_2O_3 substrate with a 4° miscut, with the thin film thickness of 90 ± 7 nm and (c) an $(Al_{0.14}Ga_{0.86})_2O_3$ thin film grown on a (100) β-Ga_2O_3 substrate with a 4° miscut, with the thin film thickness of 273 ± 6 nm. The red and blue circles indicate the simulated Bragg positions of β-Ga_2O_3 and of the $(Al_xGa_{1-x})_2O_3$ film. Since the measurement was performed in grazing-incidence geometry with an incident angle of approximately 0.15°, the diffraction is strongly surface sensitive. Under these conditions, the effective X-ray penetration depth is only about 65 nm at an X-ray energy of 20 keV. As a result, the recorded diffraction peaks and CTRs signals are dominated by the thin-film, as shown in Fig. 3.9(b) and (c).

To further interpret the diffraction patterns, one can first consider the amount of MOVPE-deposited thin film. Since the substrate is a β-Ga_2O_3 (100) with 4° miscut, its surface is well defined after standard preparation steps such as chemical etching and polishing, resulting in an epi-ready surface. Therefore, the main variables are the film thickness and the Al concentration. The lattice-parameter mismatch between the substrate and the thin film can induce strain, such as tensile or compressive strain. However, this strain cannot be clearly observed

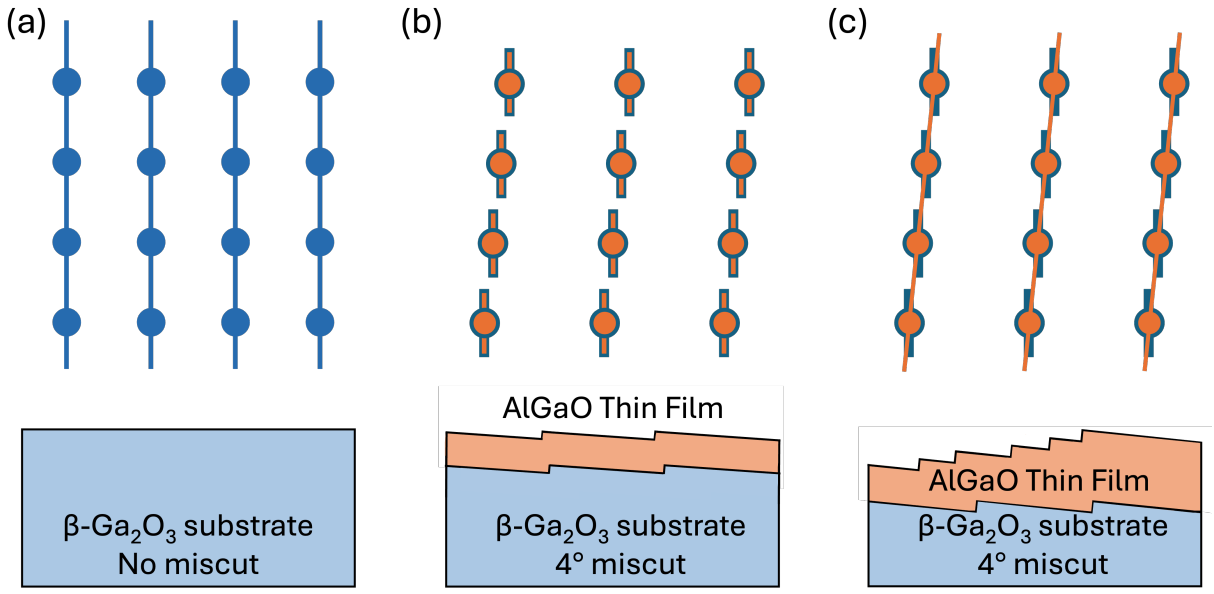


Figure 3.10: Schematic of real and reciprocal space structures for a β-Ga_2O_3 substrate and MOVPE-grown AlGaO thin film, illustrating the influence of surface miscut and step-step correlation. For the thin film samples, the system is aligned with the thin-film surface. (a) An ideal, flat β-Ga_2O_3 substrate with no miscut, producing continuous CTRs perfectly aligned with the crystallographic surface normal. (b) A 4° miscut β-Ga_2O_3 substrate with an ideally thin film on top and a perfectly regular train of steps. A strong step-to-step correlation leads to CTR streaks oriented perpendicular to the crystallographic surface normal, with the Bragg peak signals aligned perpendicular to the stepped surface. (c) A 4° miscut β-Ga_2O_3 substrate with a thicker film (step bunching) on top and weak step–step correlation. The weak correlation causes the CTR signal oriented perpendicular to the crystallographic surface normal, but tilted by 4°. [67] Blue represents the signal contribution from the substrate, and orange represents the contribution from the thin film.

in our diffraction patterns, likely due to the limited penetration depth of the experimental setup. In addition, the lattice-parameter difference between the pure single crystal and Al-alloyed films is relatively small, with a maximum of about 2.5 % for the $(Al_{0.14}Ga_{0.86})_2O_3$ thin film. Hence, the most noticeable difference between the two thin-film samples arises from the amount of material deposited on the substrate. This difference becomes clear when comparing the two MPI images, its Bragg peaks, and the surrounding regions where CTR signals are visible as figure 3.9 shown. While the CTR features may appear similar at first glance, a more careful examination shows that their orientation and continuity can differ from the difference of growth results. For samples with a thinner deposited thickness, the epitaxial layer better follows the substrate steps and the miscut, leading to a surface that is strongly correlated with the underlying miscut substrate, which result in step-flow growth. In this case, the CTRs appear as streaks perpendicular to the crystallographic surface normal. In contrast, for thicker deposited thicknesses the surface is typically less well correlated with the miscut substrate and step-bunching can form on the surface, this result in weak step–step correlation. As a consequence, the CTR streaks remain continuous and reflect a tilt of $4°$, so that they become perpendicular to the step surface (Fig. 3.10). A comparable X-ray effect and its physical origin were previously discussed by E. Vlieg in [67].

3.4.3 Cleavage Planes

β-Ga_2O_3 is the most thermodynamically stable phase of gallium oxide and exhibits pronounced anisotropy in its structural, mechanical, and fracture properties. [5, 42] One of the most characteristic features of β-Ga_2O_3 single crystals is their strong tendency to cleave along specific crystallographic planes. The arrangement and directional nature of the Ga–O bonds create planes of comparatively weak interatomic bonding. [68] As a result, mechanical processing and device fabrication steps must take these preferred cleavage planes into account to avoid unintended fracture.

The two dominant cleavage planes in β-Ga_2O_3 single crystal are the (100) and (001) planes. These planes correspond to regions in the crystal structure where the bond density is low and the connectivity between the Ga–O polyhedra is relatively weak compared to other orientations. [42] When the crystal is treated with mechanical stress, it is energetically most favorable along these planes, producing the smooth, mirror-like cleavage surfaces. Among the two, the (100) plane is widely considered as the primary and easiest cleavage plane.

First-principles calculations confirm that it has the lowest surface energy, meaning that the

(100) surface is the most thermodynamically stable surface. This stability is closely linked to its cleavage behavior: because forming a (100) surface incurs the smallest energy penalty and involves the weakest bonding across the plane, it requires the least mechanical work to fracture. As a result, cracks preferentially propagate along this plane under applied mechanical force. [9] Consequently, β-Ga_2O_3 wafers often cleave along the (100) direction when stress is applied at the edges. While this pronounced cleavage tendency can be advantageous for producing clean, well-defined surfaces but also complicates wafer handling, cutting, and thinning processes. [69]

However, the (001) plane also serves as a second major cleavage plane, it is generally less favorable than the (100) plane. Cleaving along (001) may occur when stress is applied near edges or along directions that promote crack initiation in this orientation. While the resulting fracture surfaces are likewise smooth, initiating cleavage on the (001) plane typically requires higher mechanical stresses.

A detailed understanding of these cleavage planes is essential for crystal growth, substrate preparation, and device fabrication. The cleavage behavior influences how crystals can be cut into wafers without introducing cracks or defects. In microfabrication, laser dicing, scribing, and polishing processes must be carefully aligned with the cleavage directions to minimize chipping. Furthermore, the existence of preferred cleavage planes affects the long-term reliability of devices, particularly in high-voltage or high-power applications where mechanical stress may arise from thermal cycling or packaging.

Overall, the (100) and (001) cleavage planes are defining features of β-Ga_2O_3 and play a crucial role in both its mechanical behavior and its technological applications. A thorough understanding and control of cleavage phenomena are therefore essential for optimizing β-Ga_2O_3-based electronic and optoelectronic devices, ensuring both structural stability and high performance. In this thesis, all single crystals surfaces investigated are (100)-oriented, which are the thermodynamically lowest-surface-energy plane.

3.4.4 Termination of the (100) Surfaces

The monoclinic β-Ga_2O_3 crystal cleaves primarily along the (100) plane, which is widely considered the most thermodynamically stable and lowest-energy surface, as discussed in the previous section. Determining the precise atomic arrangement of this as-cleaved (100) surface is of fundamental importance, since the specific surface termination strongly influences the surface properties that are crucial for subsequent semiconductor processing and epitaxial

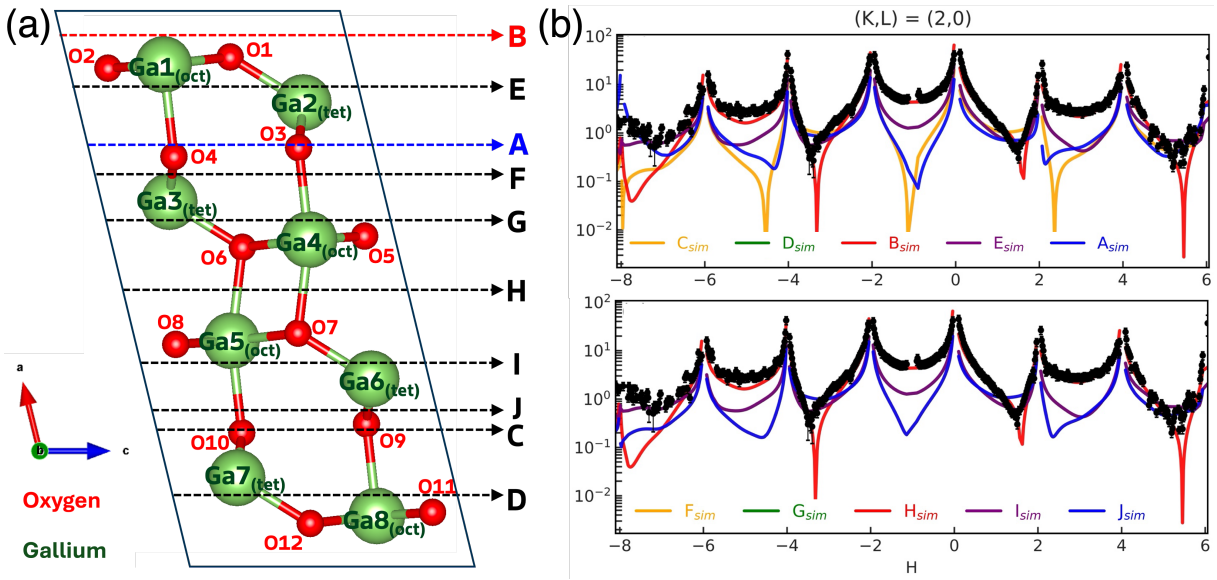


Figure 3.11: (a) All possible surface terminations of the as-cleaved β-Ga_2O_3 (100) surface. Terminations B, E, A, F, and G are symmetry-equivalent to terminations H, I, J, C, and D. (b) Experimental measured data (symbols) and simulated structure factors (solid line) for the different (100) surface terminations. The curves for terminations D & E, F & J, and G & I are fully overlap to each other because the two terminations are symmetry-equivalent and therefore produce identical structure factors.

growth.

Recent Density Functional Theory (DFT) studies provide a deeper understanding of this cleavage behavior by evaluating the surface energies of possible cleavage planes, as the thermodynamic cost of fracture propagation is determined by the energy required to create new surfaces. [9] These calculations show that the (100)B termination has the lowest surface energy, followed by the (100)A termination, as illustrated for all (100) surface terminations in Figure 3.11(a). Due to the bulk crystal lattice symmetry, several of these geometries are structurally related. For example, terminations B, E, A, F, and G are symmetry-equivalent to terminations H, I, J, C, and D, respectively. Structurally, the A-termination corresponds to a cleavage plane that cuts through corner-sharing oxygen octahedra and tetrahedra, producing an oxygen-terminated surface. In contrast, the thermodynamically preferred (100)B termination results from cleavage through edge-sharing oxygen octahedra, leaving oxygen atoms that remain bonded to two adjacent gallium atoms. The average broken bond lengths for the (100)A and (100)B terminations are 1.94 Å and 2.00 Å, respectively. The (100) surface can be classified as a Tasker II-type surface, where the specific atomic arrangements cause the (100)A termination to be polar and the (100)B termination to be non-polar. The Tasker classification provides a framework for describing the stability of these cleavage planes. In this model, ionic surfaces

are categorized according to the charge distribution within their atomic layers: a Tasker I-type surface is strictly neutral, with each plane containing equal numbers of anions and cations, while a Tasker II-type surface consists of charged planes arranged in a symmetric stacking sequence that cancels any net dipole moment perpendicular to the surface. [70, 71]

While theoretical models and DFT calculations strongly indicate that the B-termination is the preferred cleavage plane of the (100) surface, this conclusion is further supported by Figure 3.11(b), which demonstrates excellent agreement between the simulated structure factors and the experimental CTRs. The full analysis of the surface terminations and atomic structure, including CTR measurements and advanced characterization of the cleaved crystal surfaces, will be presented in Chapter 4.

3.4.5 Twin Domain in β-$(Al_xGa_{1-x})_2O_3$ Single Crystals

During the initial stages of crystal growth, twinning, as well as planar and point defects, can form relatively easily. This is particularly common in lower-symmetry monoclinic systems such as β-Ga_2O_3, which are more sensitive to growth-induced stresses and can more readily develop complex defect structures than cubic materials. When multiple twin domains coexist within the measured crystal volume, the resulting diffraction patterns exhibit superimposed sets of reflections from each individual domain. Identifying the characteristics of the twin domains and determining the type of twinning is essential for reliable structural analysis.

As illustrated by the atomic model in Figure 3.12(a), a twinned crystal can be represented as mirroring of the unit cell, where the primary domain is outlined in red and the twin domain in blue. The corresponding simulated reciprocal space map is presented in Figure 3.12(b), where the size of the plotted points reflects the relative intensity of the Bragg's signals. When the crystal is twinned, two superimposed sets of simulated diffraction spots (red and blue) appear, while an untwinned (single-domain) crystal shows only one set. Throughout this thesis, the reciprocal space axes H and L are used consistently to denote the directions of all structure factor data, including the experimental diffraction patterns as Figure 3.13 and Figure 3.14 shows. The real-space crystal direction labeled as *surf.*, which is corresponding to the c-axis, [001], of the monoclinic unit cell.

A closer examination of the simulated reciprocal space diffraction pattern reveals that the twin operation is not an exact symmetry of the lattice, but is very close to one. As a result, the lattices of the different twin domains nearly identical in reciprocal space, leading to diffraction patterns that are not perfectly overlapped. This leads to Bragg reflections that appear either

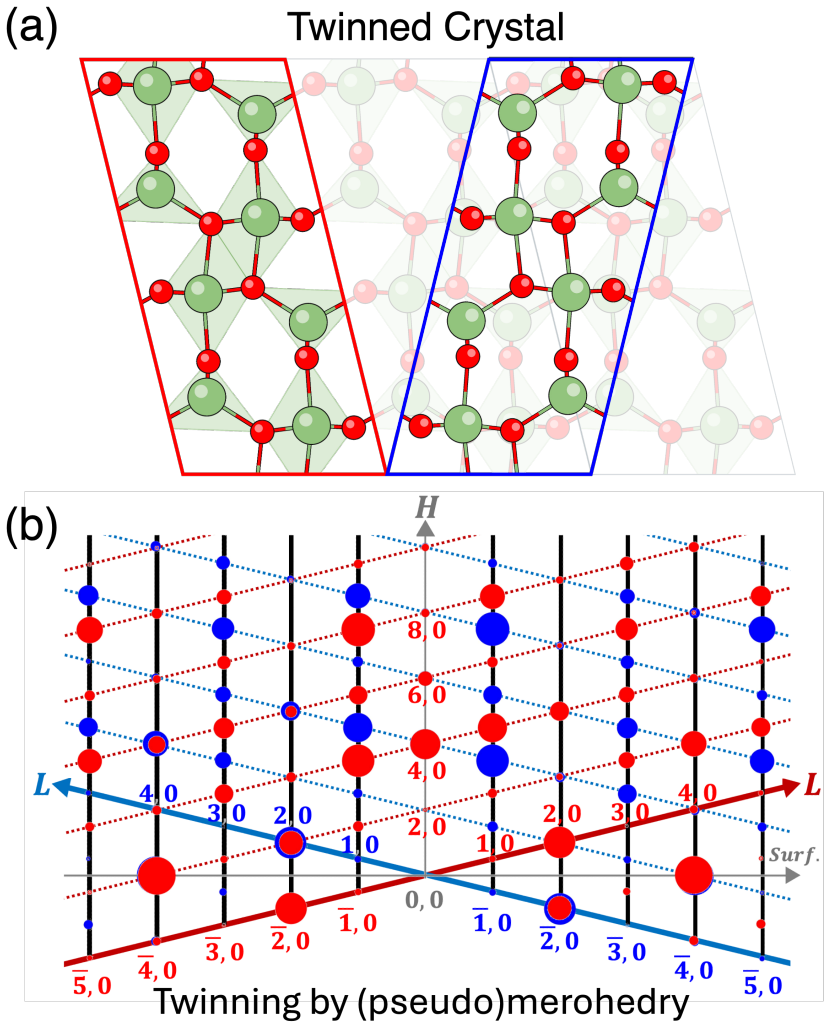


Figure 3.12: Schematic of the twinned structure. (a) Real-space illustration of the twinned crystal, with the primary and twin domains shown in red and blue, respectively. (b) Simulated reciprocal space map demonstrating **twinning by (pseudo)merohedry**. A twinned crystal exhibits two superimposed sets of diffraction spots (red and blue), where an untwinned single domain shows only one set. The reciprocal space axes H and L are used consistently throughout this thesis to label all diffraction data, including CTRs. The indicated real-space crystal direction labeled as *surf.* corresponds to the c-axis, [001], of the unit cell.

superimposed or slightly split, reflecting the fact that the twin domains differ only marginally in orientation and symmetry, as illustrated in Figure 3.12(b). This behavior is characteristic of twinning by pseudo-merohedry (or more specifically, reticular pseudo-merohedry, depending on the twin index). [72–75]

To understand the origin of the diffraction spot splitting observed in our experimental data, it is useful to point out pseudo-merohedry with true merohedry. [73] In twinning by true (reticular) merohedry, the twin operation is fully compatible with the crystal lattice or an exactly

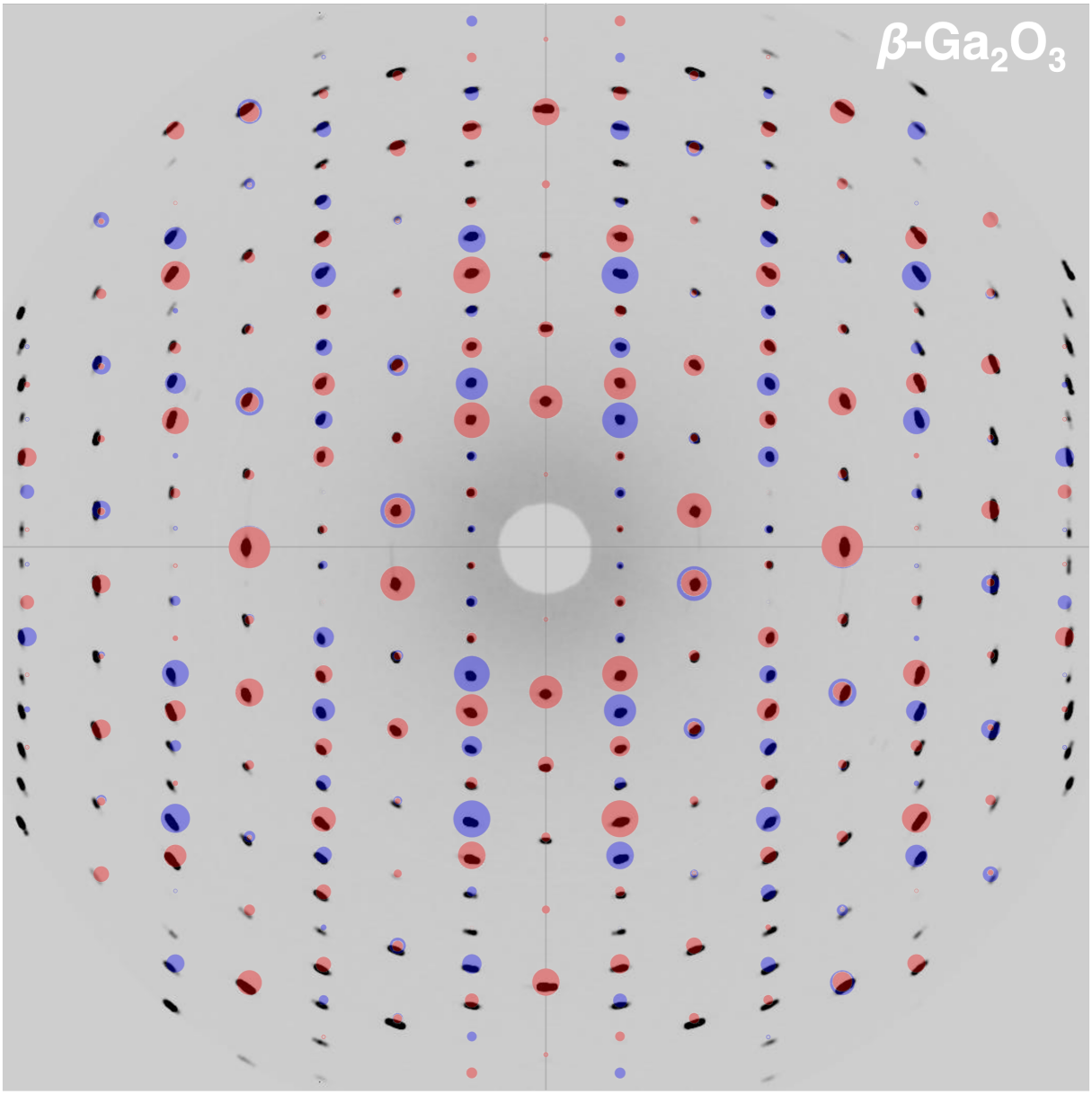


Figure 3.13: Reconstructed $H0L$ reciprocal space plane of twinned β-Ga_2O_3 (100) single crystal. The experimental X-ray diffraction data (black spots) are overlapped with simulated reflections corresponding to the primary domain (red) and the twin domain (blue).

restored sublattice. The lattice points of the twin individual are overlap perfectly with those of the primary domain, and the reciprocal lattices coincide exactly. Consequently, no splitting of Bragg reflections occurs. For the structure refinement of the crystals investigated in this work, this true merohedry twinning was taken into account during data processing. Specifically, the twin operation relating the reciprocal lattices of the two domains was incorporated into the SHELXL refinement using the following transformation matrix as

$$\begin{pmatrix} 1 & 0 & 1 \\ 0 & -1 & 0 \\ 0 & -1 & -2 \end{pmatrix} \tag{3.2}$$

In contrast, twinning by pseudo-merohedry occurs when the crystal lattice only approximates a higher symmetry. Under the twin operation, the reciprocal-lattice points of the twin domain do not coincide exactly with those of the reference lattice but are instead only quasi-aligned. As a result, the reciprocal-lattice axes of the two domains are slightly misoriented. Although both share a common origin at (0,0,0), the difference in their Bragg angles becomes increasingly pronounced at higher scattering vectors. Within the $(H, 0, L)$ plane, this geometric mismatch leads to a gradual separation of the corresponding reciprocal-lattice points, so that the distance between the superimposed reflections (e.g., the red and blue spots in the simulated model) increases systematically with increasing L.

This defining pseudo-merohedry splitting feature is clearly observed in our SCXRD data. Figure 3.13 presents the unwarp $(H, 0, L)$ plane diffraction pattern of twinned β-Ga_2O_3 crystal. The black spots correspond to the experimentally measured dataset unwarp using the Rigaku CrysAlis^{Pro} software, [76] while the overlapping blue and red spots represent the simulated reciprocal space map originating from the two domains. As expected for pseudo-merohedry twins, the spatial splitting between the corresponding diffraction spots becomes more pronounced at higher L values, reflecting the increasing misorientation between the two domains in reciprocal space. Conversely, Figure 3.14 shows an untwinned 20% Al-doped $(Al_xGa_{1-x})_2O_3$ crystal, where no such splitting effect is observed. In this case, the reciprocal space map exhibits a single, well-defined set of Bragg reflections associated exclusively with the primary domain, indicated in red. The absence of additional reflection sets (in blue) or gradual separation confirms that the crystal contains no detectable pseudo-merohedry twin domains. This demonstrates that the reciprocal-lattice axes remain perfectly aligned without any detectable divergence in their Bragg angles and that the crystal is indeed untwinned. All

unwarped images and the analyzed data processed using Rigaku CrysAlis^{Pro} can be found in Appendix A.3.

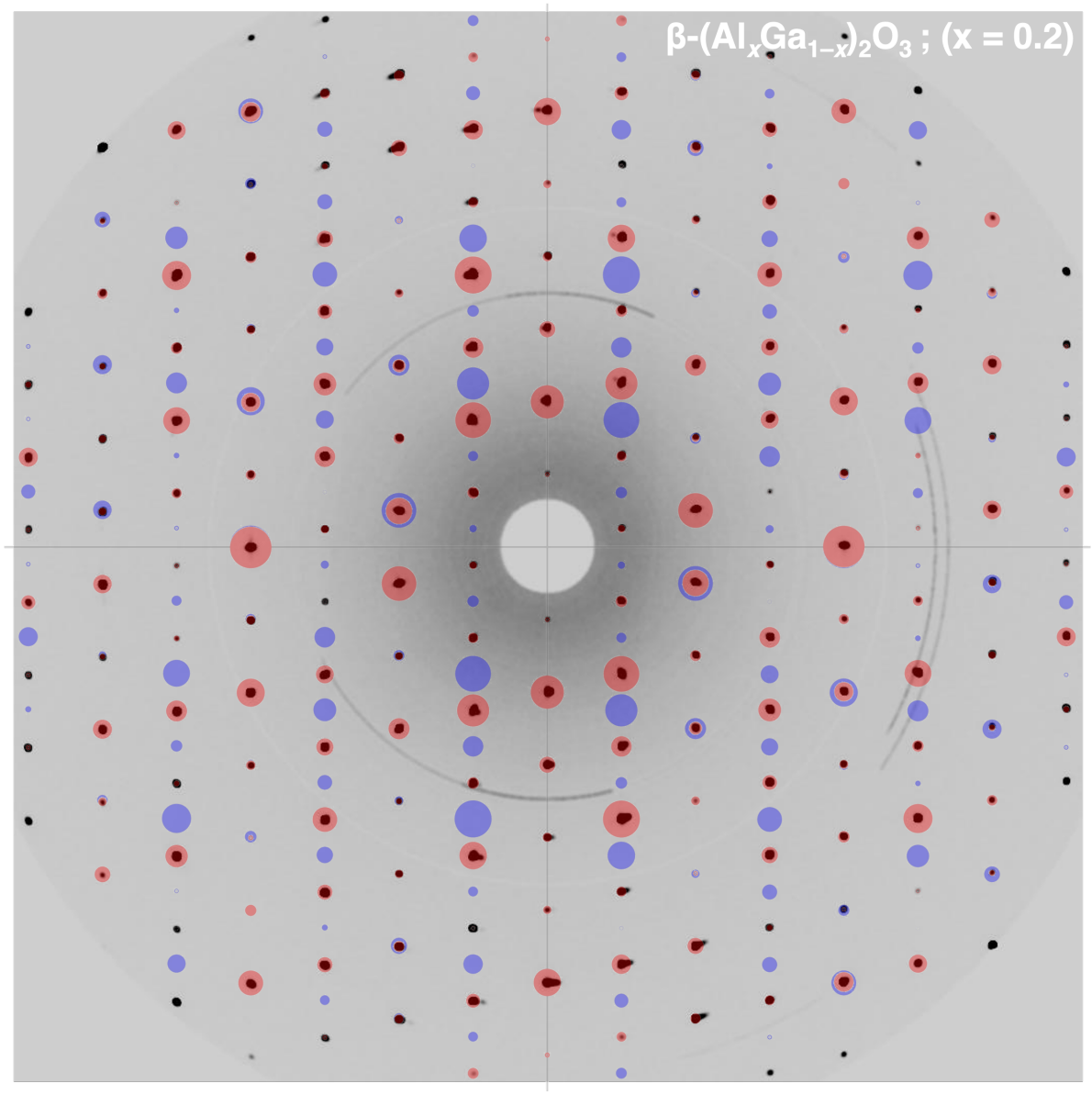


Figure 3.14: Reconstructed $H0L$ reciprocal space plane of untwinned 20% Al-doped β-Ga_2O_3 (100) single crystal. The experimental X-ray diffraction data (black spots) are overlapped with simulated reflections corresponding to the primary domain (red) and the expected twin domain (blue). The absence of experimental diffraction spots at the blue twin positions confirms the untwinned nature of the crystal.

Chapter 4

Surface Crystallography of As-cleaved β-Ga_2O_3(100) Crystals

This chapter is based on a research article published open access in *Applied Physics Letters*, volume 128, issue 7 (February 17, 2026), available at doi.org/10.1063/5.0309937. The supporting information is available in Appendix A.1.1.

4.1 Surface Termination of β-Ga_2O_3(100) As-cleaved Single Crystals

Abstract

The surface of β-Ga_2O_3 single crystals cleaved along their (100) plane is investigated using surface X-ray diffraction and atomic force microscopy. The results show the surface to consist of a single, so-called B-termination, which means that the crystal cleaves at planes formed by edge-sharing oxygen octahedra, thereby breaking the longest and weakest Ga-O bonds. Refinement of the atomic positions result in small displacements from the bulk structure, at most approx. 0.01 Å. Atomic force microscopy suggests that relatively large terraces form together with steps of half the a-axis length of approx. 0.6 nm, which means that terraces have the same atomic termination, related by the crystal symmetry. These results are important as a fundamental property of β-Ga_2O_3 when being processed or used in various semiconductor applications.

Introduction

Methods

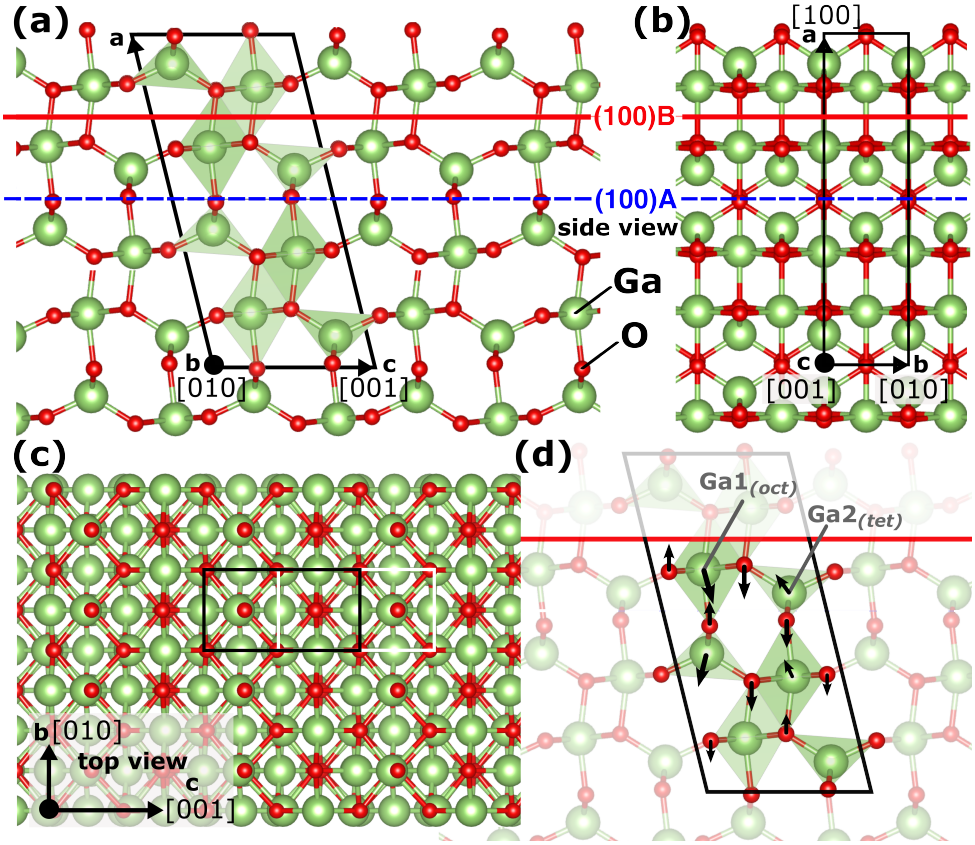


Figure 4.1: Two possible surface terminations of β-Ga_2O_3(100) are indicated by red and blue dashed lines. The A-termination is a plane through the corner-sharing oxygen octahedra and tetrahedra. The B-termination is a plane through edge-sharing oxygen octahedra. The average broken bond length for B-termination is slightly higher than for the A-termination. The unit cell is shown in the (a) [100]/[001], (b) [100]/[010], and (c) [010]/[001] planes. (d) The fitted displacements of gallium atoms at the octahedral (Ga_{oct}) and tetrahedral (Ga_{tet}) sites, as well as the oxygen atoms, for the B-terminated surface are shown. The length of the displacement arrows are proportional to the magnitude of the displacement, but it is scaled up by a factor of approximately 100 to enhance visibility.

High-quality β-Ga_2O_3 single crystals were grown using the Czochralski method at the Leibniz-Institut für Kristallzüchtung (IKZ). [18, 45] β-Ga_2O_3 has a monoclinic crystal structure with space group $C2/m$. The conventional unit cell contains four formula units, with gallium atoms (green) occupying both tetrahedral and octahedral coordination sites as shown in Fig. 5.4. The lattice parameters are a = 12.214 Å, b = 3.037 Å, c = 5.798 Å, α = 90°, β = 103.83°, and γ = 90°. [42–44] All fractional coordinates listed in Table S3 and used for CTR fitting are defined with respect to this unit cell.

The single crystals were cleaved along the (100) plane under ambient conditions, [18, 45] and their surfaces were used for all subsequent measurements without further polishing or chemical etching. The samples were prepared to dimensions of 10 mm × 10 mm and the thickness around 0.1 mm. Prior to use, all surfaces were cleaned in an ultrasonic bath with

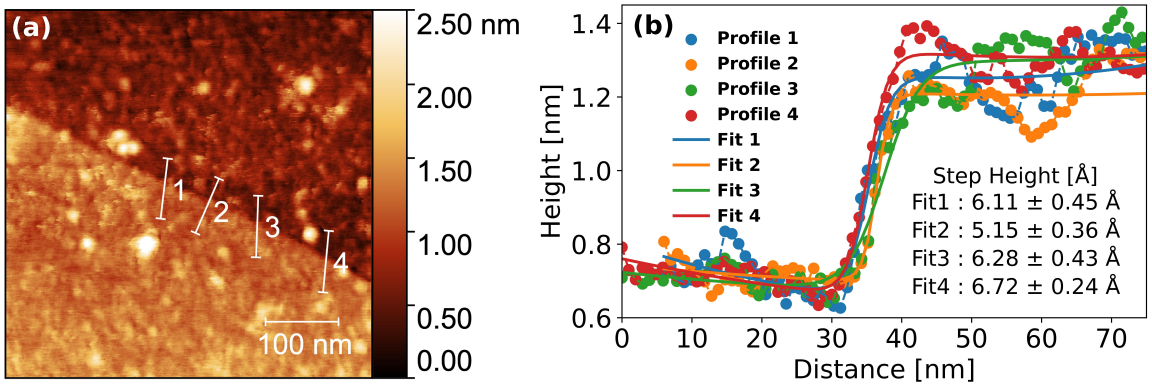


Figure 4.2: (a) AFM image of the as-cleaved β-Ga_2O_3(100) single crystal, showing the surface morphology and step structure. Four representative line profiles are indicated on the image. (b) Height profiles corresponding to the four indicated lines in (a), together with their fits. The profiles reveal a step height of approximately half the unit cell.

ethanol and isopropanol for 30 minutes.

Atomic force microscopy (AFM) was performed in air using tapping mode with a silicon cantilever at the DESY NanoLab. [33] The nominal tip radius was 8 nm, the resonance frequency was 301.6 kHz, and the scan rate was 0.5 kHz. The data were analyzed using Gwyddion software, [77] as described in detail in Fig. S1 and Tab. S1.

Crystal truncation rod (CTR) data were collected at the *Surfaces and Interfaces X-ray Scattering* (SIXS) beamline of the French synchrotron facility SOLEIL, using a photon energy of 18.42 keV. The measurements were performed in grazing incidence geometry using a diffractometer hosting an UHV chamber, which enables in situ experiments with sample heating up to 1000 °C and controlled oxygen dosing. Scattered intensities were recorded using a two-dimensional hybrid photon-counting detector XPAD S140. [78] Both the preparation and measurement chambers maintained background pressures in the low 10^{-10} mbar range. Structure factors (SF) were obtained by integrating the measured data with the BINoculars package. [37] Subsequent surface structure refinement was conducted using the ROD program from the ANAROD package. [39]

Surface X-ray diffraction (SXRD) is a powerful technique for determining the atomic structure of crystal surfaces with sub-angstrom precision. The abrupt ending of a crystal's periodic atomic arrangement at its surface results in additional diffracted intensity in between the Bragg peaks in the surface normal direction, known as Crystal Truncation Rods (CTRs). [79] The intensity along these rods is calculated by evaluating the structure factor, which contains information about the atomic positions, site occupancies and Debye-Waller factors. [39] In general, the best CTR data quality is obtained for very smooth surfaces since its intensity is

Figure 4.3: LEED patterns and in-plane reciprocal space maps of the β-Ga_2O_3(100) single crystal after annealing. (a) LEED pattern recorded at an electron energy of 98.4 eV. (b) Two-dimensional in-plane reciprocal space map, acquired at an X-ray energy of 18.42 keV. Both figures are indexed by (K, L).

affected by surface roughness. [80]

Pre-characterization of the as-cleaved bulk crystal was performed using low-energy electron diffraction (LEED) at the SIXS beamline. The sample was annealed at 400 °C in an oxygen partial pressure of 10^{-6} mbar for one hour to effectively remove contaminants. After cleaning, the crystal was characterized by LEED over a range of electron energies to verify its structure and overall crystal quality. Then, the sample was transferred in vacuum to the main diffraction chamber for the SXRD measurements.

RESULTS AND DISCUSSION

Cleaned as-cleaved β-Ga_2O_3(100) surface

The surface morphology of the cleaned, as-cleaved β-Ga_2O_3(100) surface was investigated using AFM and Fig. 4.2(a) presents a typical image. The most obvious feature is a step, separating two terraces. Detailed analysis by fitting a Boltzmann bent step function across the step at several positions (see Fig. 4.2(b)) reveals a step-height of approximately 0.6 nm, which represents half the unit cell along the a-axis. Such step heights have also been reported previously. [81,82] The average step density on such a cleaved surface is expected to be very low and scanning the surface at a random position has a low probability of capturing a step. This is similar to the structurally related oxide crystal muscovite mica, which also exhibits a monoclinic structure and also contains an easy cleave plane, resulting in millimeter-sized terraces. [83] Apart from such steps, the AFM images show the presence of many particle-like features. The nature and origin of these features is at present still unclear, but similar structures are also visible in high-quality substrates prepared by polishing and annealing for epitaxial growth. [81, 84] Such epi-ready substrates with well-defined miscuts show a clear step-and-terrace structure whereby these particle-like features seem to accumulate at the steps, in contrast to the as-cleaved surface studied here where they appear randomly over the entire surface. Nevertheless, the analysis of the AFM images shows that the as-cleaved surfaces exhibit a flat and smooth terrace structure, which is a prerequisite for SXRD experiments as described hereafter.

Figure 4.3(a) shows the LEED image of the as-cleaved (100) surface. A clear pattern of spots, which reveal the rectangular surface cell is observed, indicating a well-ordered crystalline structure. Similarly, an in-plane reciprocal space map, recorded with SXRD (see Fig. 4.3(b)),

also shows a well-defined crystal structure. The SXRD data also clearly show mosaicity, which indicate that rotated grains exist. Nevertheless, within the arcs of intensity there is one clear most intense component, which indicates the presence of one large single-crystal-like block.

Surface terminations

The obtained experimental CTRs (see Fig. 4.4) are compared with the various possible surface terminations, as further detailed in Figs. S2–S4. A first comparison by evaluating the χ^2 values are listed in Table S2, based on CTR simulations assuming a bulk termination, i.e. no further atomic relaxations and only optimizing the overall scale factor, clearly favors the (100)B surface with a significantly smaller difference between the other terminations. A density functional theory study [9] ranked the (100)B surface to have the lowest and the (100)A the second lowest surface energy, which leads us to compare these two terminations in more detail. The A-termination consists of singly-bound O atoms resulting in a mainly oxygen-terminated surface, which cuts through a plane of corner-sharing oxygen octahedra and tetrahedra. The (100)B termination consists of O atoms bound to two Ga atoms and corresponds to a plane cutting through edge-sharing oxygen octahedra. The average broken bond length for terminations (100)A and (100)B are 1.94 Å and 2.00 Å respectively. [43] The (100) surface can be classified as a Tasker II-type surface [85] where the details of the surface structure lead to the (100)A being polar and (100)B non-polar. [86]

Refinement against the CTR data of the atomic positions in the topmost layers leads to by far the best fit for the B termination (χ^2 = 1.2) than for A (χ^2 = 12.1). Actually, the fit using the A termination does not converge within the maximum displacement limits of approx 1 Å, as set in the software. The atomic positions of the Ga atoms were fitted along the [100] and [001] directions, thereby following the underlying monoclinic symmetry as present in the bulk crystal. For the oxygen atoms, which have a much lower scattering power, it was found that only refinement along the out-of-plane direction was stable and therefore the in-plane positions were kept fixed at their bulk values. The maximum displacements from the bulk position in the case of termination B is about 0.1 Å, which shows that it is a nearly bulk-terminated surface. The best CTR fit result for termination B is shown in Fig. 4.4. Schematically, the atomic displacements from their bulk positions are shown in Fig. 5.4 and the final fractional co-ordinates as well as the Debye-Waller factors are listed in Table S3.

The refined atomic positions agree very well with the density functional theory study by Mu et al. [9] In particular, the CTR analysis shows that the topmost octahedrally co-ordinated

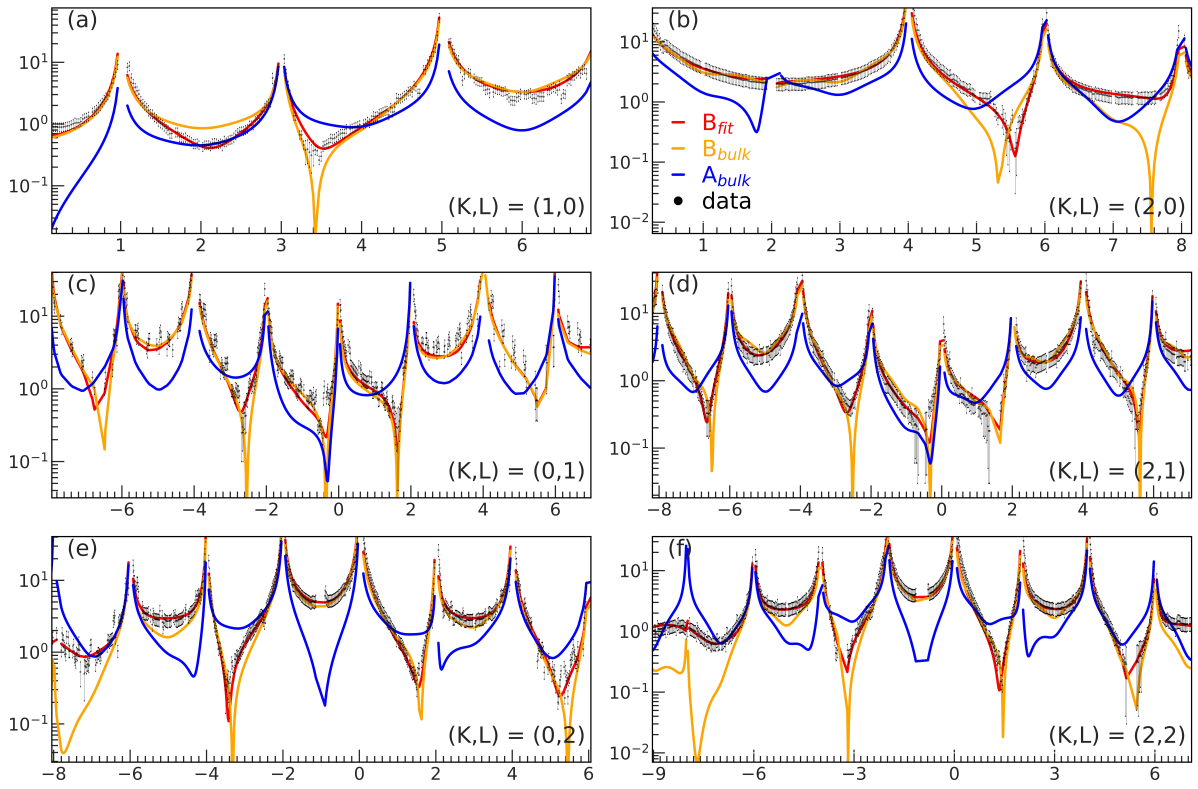


Figure 4.4: Comparison of experimental, simulated, and fitted CTR data. The bulk structure factor (F) are shown as black circles with error bars. Simulated CTRs for terminations A and B are represented by blue and yellow lines. Fitted CTRs for termination B is indicated by red line. Each CTR is indexed by (K, L) and plotted as a function of H.

Ga atom ($Ga1_{oct}$) relaxes inward by approximately 0.1 Å and the topmost tetrahedrally coordinated atom ($Ga2_{tet}$) outward by approx. 0.04 Å, resulting in a less buckled Ga-plane. Similar relaxations were also found by another DFT study by Bermudez et al. [87], however in that study these were found to extend to deeper layers. In particular the relaxation of Ga3 seems significant, although our CTR analysis finds an almost negligible displacement from its bulk position. Overall, it can be concluded that there is good agreement with the DFT calculations given that relatively small differences between the two methods can be understood by considering experimental uncertainties of the order of 0.01-0.02 Å and possible systematic differences, such as different lattice parameters, between the models used in the DFT study and the present experiment. Although the CTRs are not particularly sensitive to the oxygen positions, there is also an overall good agreement between theory and experiment, in particular with respect to the oxygens atoms surrounding the topmost $Ga2_{tet}$ and $Ga1_{oct}$ showing the largest displacements in the range of 0.05–0.1 Å. Table S4 shows in detail the atomic distances between Ga an O atoms in the topmost layer as found by Bermudez et al. [87] and our study and shows a maximum deviation of about 0.05 Å. The uncovered (100)B termination is also in agreement with previous experimental studies, either on cleaved bulk crystals [88] or on an ultrathin Ga_2O_3 layer, grown by selective oxidation of a CoGa(001) single crystal. [89, 90] The results of a recent photo-electron diffraction study [91] is not in good agreement with our and the previously mentioned DFT studies. Although that study also favors the (100)B termination, the atomic positions found disagree. For example, Kilian et al. find that the distance along the surface normal direction between the$Ga1_{oct}$ and $Ga2_{tet}$ atoms is 1.17 Å, thereby enlarging the bulk value by 41%. This is not at all in accord with the nearly bulk-terminated structure found in this study, where the typical displacements from the bulk are of the order of 1%.

CONCLUSIONS

In summary, we have comprehensively characterized the as-cleaved β-Ga_2O_3(100) by combining AFM, LEED, and SXRD. The surface morphology indicates that the cleaved surface is single terminated, most likely with terrace sizes exceeding the typical AFM scan area of the order of several μm^2. LEED and in-plane reciprocal space mapping by SXRD reveal a well-ordered unreconstructed surface. Surface crystallography by CTR measurement and fitting enables to obtain a high-resolution structure, consisting of the so-called (100)B termination with relatively small (maximum 0.1 Å) atomic relaxations from bulk positions. This structure is in excellent agreement with a DFT study and is in line with other experimental studies

on similar surfaces. Such a nearly bulk-terminated surface, formed along a cleave plane, is also the most obvious when considering that the longest (and weakest) Ga-O bonds are broken and that it constitutes a non-polar surface. The high-resolution crystallographic surface structure determined in this study is important for fracture properties of β-Ga_2O_3, thin film growth on β-Ga_2O_3(100) substrates and electronic surface properties of such substrates or exfoliated flakes. In addition, the accurate determination of the single crystal surface structure, as presented in this study, is essential for future investigations on gas adsorption, particularly when β-Ga_2O_3 is employed in gas sensing applications. A comprehensive understanding of adsorption mechanisms requires precise knowledge of the surface structure. These insights are expected to play a significant role in the development of advanced sensors based on our observation.

See the supplementary material A.1.1 for the bulk and fitted fractional atomic positions, as well as the analysis of the experimental data.

This project is funded by the Deutsche Forschungsgemeinschaft (DFG, German Research Foundation) under the project number 491040331. We acknowledge SOLEIL for provision of synchrotron radiation facilities and we would like to thank beamline staffs for assistance in using beamline SIXS under proposal 20230826. We also acknowledge DESY (Hamburg, Germany), a member of the Helmholtz Association HGF, for the provision of experimental facilities. Parts of this research were carried out at DESY NanoLab.

The full published document is available at https://doi.org/10.1063/5.0309937

Chapter 5

X-ray Study of $(Al_xGa_{1-x})_2O_3$ Single Crystals and Their (100) Cleave Plane

This chapter is based on a manuscript draft of a research article that will be published open access in *APL Materials*,(2026). The corresponding supporting information is provided in Appendix A.2.1.

Abstract

Alloying β-Ga_2O_3 with aluminium has been identified as a viable route for band-gap engineering of this promising wide band gap semiconductor. Here we present results of X-ray diffraction studies of single crystals and their (100) surfaces prepared by cleaving, grown at the Leibniz-Institut für Kristallzüchtung. By combining the average electron density, as obtained by X-ray reflectivity, and the lattice parameters from X-ray diffraction, the aluminium content can be determined with an accuracy of within approximately 1 %. Crystal truncation rod data and their analysis are presented for the $(Al_{0.2}Ga_{0.8})_2O_3$ (100) surface. The influence of different bulk structure models on the obtained surface structure are discussed and it is concluded that the crystal cleaves at the so-called B-termination, just as β-Ga_2O_3.

Introduction

Beta-type gallium oxide (β-Ga_2O_3) is a transparent, wide-bandgap semiconductor with a band gap of approximately 4.85 eV. [2, 4, 7] This property makes it highly promising for high-power electronic devices [12, 14, 92–94] and ultraviolet photodetectors. [15–17] Its high critical electric field strength, [12] estimated to be three times higher than those of silicon carbide (SiC) and gallium nitride (GaN), gives β-Ga_2O_3 significant potential to outperform these established

materials in high-power switching applications. As a result, it is considered a strong candidate for the next generation of power systems, as it can enable more efficient energy transmission and contribute to the reduction of CO_2 emissions.

To further tune the properties of β-Ga_2O_3, it is possible to alloy it with aluminum, which leads to an almost linear increase in the band gap from 4.85 to 7 eV. [5,15,44,95,96] While tuning the band gap is advantageous, it is also essential to preserve high crystal quality and sufficient electron mobility. Pure β-Ga_2O_3 demonstrates an electron mobility of around 150 cm^2/Vs, which is critical for device performance. Achieving these characteristics relies on precise control of the crystal growth process and a detailed understanding of the effects of alloying on both surface and bulk properties. [1–3, 7]

Previously, we investigated the surface termination of as-cleaved pure β-Ga_2O_3 (100) single crystals. [97] Our studies confirmed that the termination consists of oxygen atoms bonded to two gallium atoms, corresponding to a plane intersecting edge-sharing oxygen octahedra. This surface termination is widely recognized as the most stable and energetically favorable surface for cleaved pure β-Ga_2O_3 (100), due to its minimal surface energy. In this present study, our focus shifts to $(Al_xGa_{1-x})_2O_3$ (100) single crystals with aluminum concentrations up to x = 0.3. We systematically examine how aluminum incorporation influences the lattice parameters, surface termination, and electron density. Our results are relevant as an all X-ray, non-destructive characterization method of the atomic scale quality of $(Al_xGa_{1-x})_2O_3$ substrates to be used for thin film growth.

Experimental Methods

High-quality $(Al_xGa_{1-x})_2O_3$ (100) single crystals with x = 0 to 0.3 were grown using the Czochralski method at the Leibniz-Institut für Kristallzüchtung (IKZ). [18,45,53,54,98,99] The β-phase gallium oxide adopts a monoclinic structure with space group of C2/m, and this symmetry is maintained when alloying with Al. Crystals were cleaved along the (100) plane under ambient conditions and used as-cleaved, [2] with no further surface treatment such as polishing or chemical etching. The cleaved single crystals were prepared to dimensions of 10 mm × 10 mm and the thickness around 0.1 mm. Prior to characterization, all cleaved crystals were cleaned by immersion in an ultrasonic bath with ethanol and isopropanol for 30 minutes to ensure removal of surface contaminants.

Separate samples were prepared for the bulk single crystal X-ray diffraction (SC-XRD) experiments, which were carried out at the P24 Chemical Crystallography beamline at PETRA

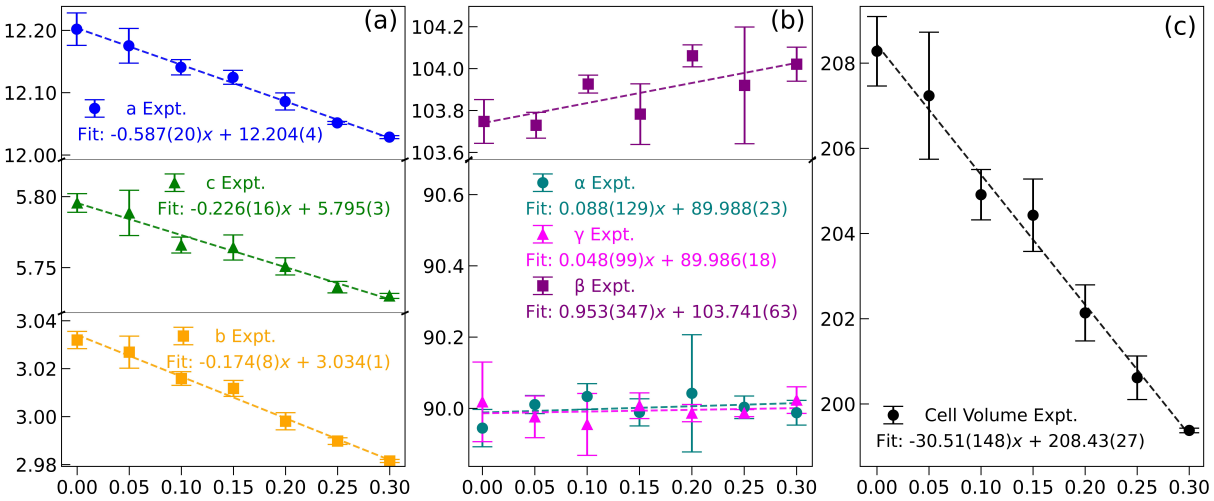


Figure 5.1: Cell parameters of $(Al_xGa_{1-x})_2O_3$ single crystals as a function of Al content (x = 0 to 0.3): (a) lattice parameters a, b, and c (in Å); (b) lattice angles α, β, and γ (in degrees). (c) unit cell volume (in $Å^3$). Experimental data measured in air are shown as symbols with error bars, while dashed lines show linear fits to the measured data.

III (DESY), Germany. [35] In order to bathe the crystals completely in the 100 × 100 μm^2 X-ray beam, dedicated sample preparation was required for the SC-XRD measurements. Very small single crystals, approximately 40 × 40 μm in size, were prepared to ensure uniform illumination. All crystals were mounted using Paratone oil on Kapton-made microloops and positioned on the goniometer of the kappa four-circle diffractometer. Diffraction patterns were collected in air at room temperature with a Pilatus 1M CdTe area detector (172 × 172 μm^2 pixel size) for high-resolution data acquisition. A full 360° rotation scan was performed, generating 1800 images at 0.2° steps to all crystals. This well-established approach is the standard for robust structure determination in crystallographic studies. A photon energy of 28 keV was used to minimize absorption and extinction effects. To further improve data quality, the detector energy threshold was set to 50% of the photon energy, effectively suppressing background from Ga Kα fluorescence (9.2 keV). Data processing was carried out using Rigaku CrysAlis^{Pro} software. [76]

Surface X-ray diffraction (SXRD) and X-ray reflectivity (XRR) experiments were conducted at the *Surfaces and Interfaces X-ray Scattering* (SIXS) beamline at SOLEIL Synchrotron, France. [34] A photon energy of 18.42 keV was used in grazing-incidence geometry. All experiments were carried out in the dedicated UHV hutch, where the SXRD diffractometer is integrated into a stationary assembly of interconnected ultra-high vacuum (UHV) chamber. This setup allows for in situ experiments with sample temperatures up to 1000°C and controlled oxygen dosing.

All SXRD and XRR measurements were performed on as-cleaved, unpolished (100) bulk crystal surfaces, which were all mildly annealed at 400 °C in an oxygen partial pressure of 10^{-6} mbar for 1 h before the measurement. Crystal truncation rod (CTR) and XRR datasets were collected using a two-dimensional silicon-based XPAD S140 detector. Structure factor (F) were obtained by integrating the measured data with the BINoculars software package. [37] Surface structure refinement was carried out using the ROD program from the ANAROD package. [39] All XRR data were analysed using the GenX software. [27]

RESULTS AND DISCUSSION

Cell parameters of $(Al_xGa_{1-x})_2O_3$ crystals

To study aluminum incorporation in $(Al_xGa_{1-x})_2O_3$ single crystals, we examined how the lattice parameters evolve with aluminum composition (x = 0 to 0.3). While Galazka et al. [18] previously studied these trends using standard laboratory powder X-ray diffraction (PXRD) technique with a Cu-K$\alpha_{1/2}$ radiation source, we bypassed the limitations of powder techniques by utilizing synchrotron-based SC-XRD with an X-ray energy of 28 keV. Data reduction and unit-cell determination were carried out using CrysAlis^{Pro} software (Rigaku). [76] After peak hunting identified thousands of strong, well-defined reflections, the primitive unit cell was determined using the program's automatic indexing routine. The monoclinic Bravais lattice was verified by evaluating the metric symmetry of the reduced Niggli cell, confirming $\alpha \approx \gamma \approx 90°$ while $\beta \neq 90°$, and by the satisfactory merging of symmetrically equivalent reflections. Final lattice parameters were obtained by cell refinement using typically 2000 to 3000 indexed reflections, depending on the sample-to-detector distance, with strict monoclinic constraints. As shown in Fig. 5.1(a), this high-precision analysis reveals a systematic and monotonic decrease in all three lattice parameters (a, b, and c) with increasing Al content. This lattice reduction is also reflected in the unit-cell volume as shown in Fig. 5.1(c), which decreases progressively with Al substitution. In contrast, the lattice angles (α, β, and γ), as shown in Fig. 5.1(b), remain virtually unchanged over the entire compositional range studied, indicating that the monoclinic symmetry of β-Ga_2O_3 is preserved despite increasing Al content. [18] The absence of significant angular distortion suggests that the crystal structure can accommodate at least 30% Al substitution without any loss of crystal symmetry. Thus, Al incorporation primarily influences the lattice dimensions, while the overall crystal structure remains largely unaffected. This is fully consistent with the results obtained by Galazka et al. using PXRD. [18] It not only confirms the compositional dependence of cell parameters but

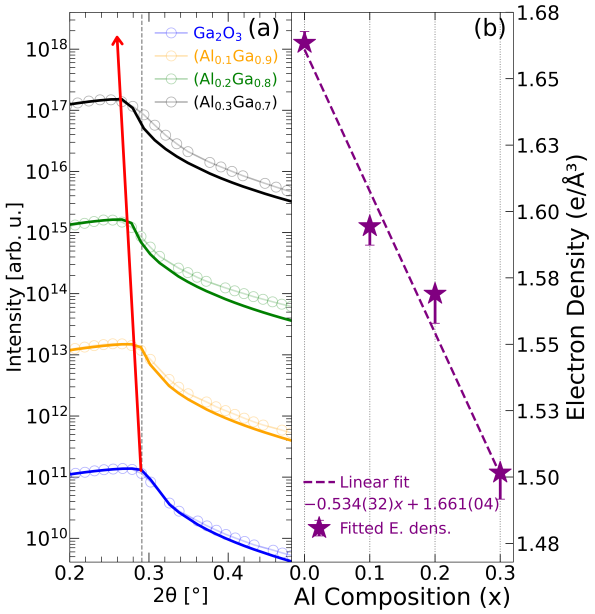


Figure 5.2: X-ray reflectivity (XRR) profiles and fitted electron density (ρ_{el}) of $(Al_xGa_{1-x})_2O_3$ (100) bulk single crystals with varying aluminum content (x = 0 to 0.3). (a) Specular reflected intensity as a function of the reflection angle (open circles) and the fitted profile (solid line). Magnified view of the critical-angle region showing the shift of the 2θ (open circles) values toward lower angles for pure β-Ga_2O_3 (blue), $(Al_{0.1}Ga_{0.9})_2O_3$ (yellow), $(Al_{0.2}Ga_{0.8})_2O_3$ (green), and $(Al_{0.3}Ga_{0.7})_2O_3$ (black). The systematic shift with increasing Al content, as indicated by the red arrow, is consistent with the decrease in mass density. (b) Fitted average electron density (purple stars) as a function of Al content, obtained from XRR fits. The dashed purple line represents a linear fit to these fitted electron densities.

also highlights the reproducibility and reliability of the observed lattice trends across different growth batches and characterization methods.

Electron density as a Function of Al Concentration

Following the analysis of the lattice parameter evolution, we investigated how increasing Al content affects the electron density, and surface morphology of $(Al_xGa_{1-x})_2O_3$ (100) single crystals. These measurements were conducted using XRR technique at an X-ray energy of 18.42 keV. Figure 5.2(a) presents the magnified view of the specular reflected intensities as a function of the reflection angle 2θ for samples with varying Al concentrations, overlaid with fitted profiles. The full 2θ range of reflectivity profiles are provided in Fig. S4, and the fitting parameters extracted from the reflectivity curves are summarized in Table S1. All measured XRR curves exhibit a smooth Fresnel reflectivity profile, indicating that the surface is an ideal, perfectly smooth cleaved surface. However, for the $(Al_{0.1}Ga_{0.9})_2O_3$ sample, slight oscillation (Kiessig) fringes were observed as the 2θ angle increased. [24] Analysis of the 2D detector images revealed that only this sample exhibited a subtle shift with increasing 2θ. This phe-

nomenon is likely due to the crystal imperfections, and it is confirmed with the fabrication quality of this batch of samples. Apart from this sample, all other samples exhibit a very smooth surface morphology. From these measured reflectivity profiles, the critical angle θ_c for each sample was directly fitted. In XRR, the critical angle is intrinsically linked to the real part of the refractive index decrement δ via the approximation $\theta_c \approx \sqrt{2\delta}$. Since δ is directly proportional to the scattering density ρ' according to the relation: [25, 100]

$$\delta = \frac{r_e \, \rho' \, \lambda^2}{2\pi} \tag{5.1}$$

where λ is the X-ray wavelength and r_e is the electron radius. The fitted value of θ_c allows for the determination of the electron density of the material. A clear trend is observed in the critical angle region, as highlighted in Fig. 5.2(a) red arrow. With increasing Al content, the critical angle shifts systematically towards lower 2θ values. This shift indicates a decrease in the overall density of the material, as the critical angle in XRR is directly related to the density of a material. Figure 5.2(b) presents the fitted electron density as a function of the nominal Al composition. A clear and systematic decrease in electron density is observed with increasing Al incorporation. Although the substitution of Ga by Al leads to a reduction of the unit cell volume V_{uc} (see Fig. 5.1c), which would tend to increase the density, this effect is dominated by the substantial reduction in the number of electrons. Since the decrease in the total electron count dominates over the reduction in volume, the net average electron density within the lattice decreases. This behavior is fully consistent with the expected compositional dependence of the real part of the refractive index and highlights the sensitivity of the XRR technique. Table 5.1, summarizes the linear fit results for the cell parameters and electron density as a function of nominal Al composition.

Table 5.1: Summary of linear fit results for the cell parameters and electron density as a function of nominal Al composition (x = 0 to 0.3). Fits were performed using the linear relation $y = m\,x + b$.

Parameter (y)	**Units**	**(m)**	**(b)**
Electron Density (ρ_e)	e/Å^3	-0.511	1.659
a-axis	Å	-0.587	12.204
b-axis	Å	-0.174	3.034
c-axis	Å	-0.226	5.795
β angle	°	0.953	103.741
Unit Cell Volume (V_{uc})	Å^3	-30.510	208.430

The experimentally determined Al composition (x) is calculated using two experimental inputs, the electron density extracted from the fit of XRR and the unit-cell volume calculated

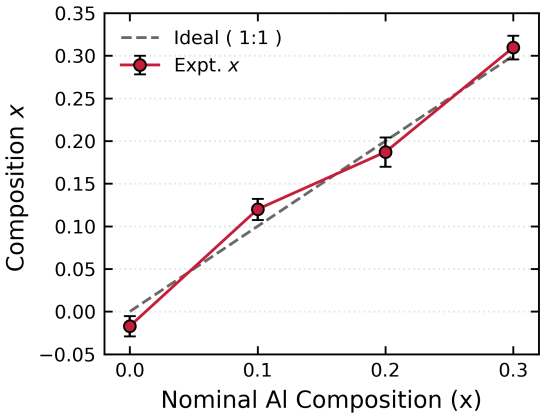


Figure 5.3: Experimentally determined Al composition (x) of $(Al_xGa_{1-x})_2O_3$ (100) single crystals, derived from fitted electron densities and lattice parameters, as a function of the nominal Al composition. The experimentally determined Al compositions are shown as red points with error bars, and the dashed line indicates the ideal 1:1 relationship with x.

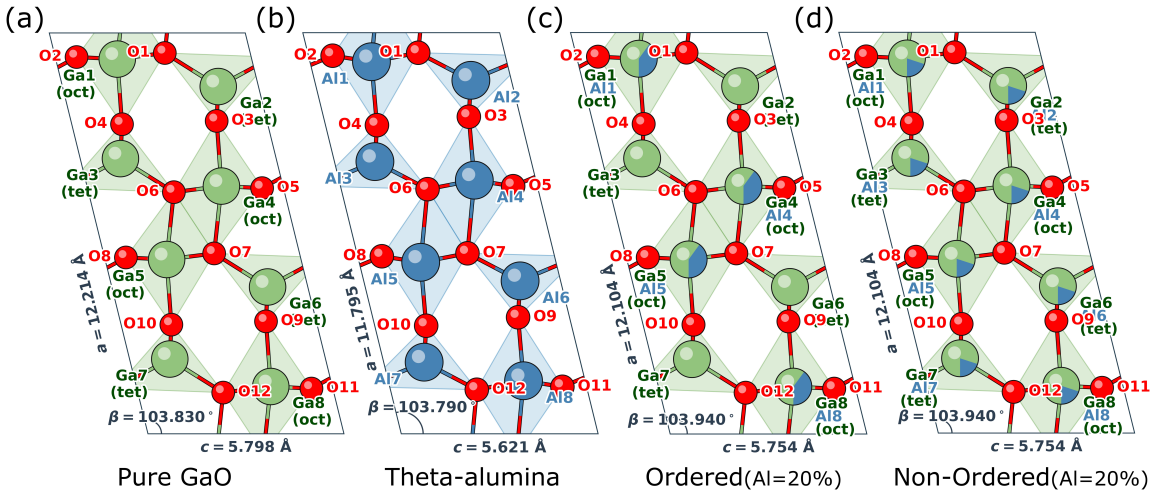


Figure 5.4: Crystallographic models of pure β-Ga_2O_3, θ-Al_2O_3, and two representative $(Al_xGa_{1-x})_2O_3$ structures with Al content of $x = 0.2$. (a) Pure β-Ga_2O_3. (b) θ-Al_2O_3. (c) Ordered model with Al occupying only the octahedral sites. (d) Non-ordered model with Al distributed over both octahedral and tetrahedral sites. Al atoms are shown in blue, Ga in green, and O in red.

from the lattice parameters obtained by SC-XRD. Figure 5.3 presents the experimentally determined Al composition as a function of the nominal Al composition (x). The electron density obtained from the XRR fit, ρ_e, represents the concentration of electrons per unit volume, while the unit-cell volume V_{uc} defines the physical space of the unit-cell. By multiplying these two experimental quantities, we obtain the total number of electrons present in a single unit cell. Since aluminum atoms have 13 electrons, while gallium atoms have 31 electrons, substituting Ga with Al systematically decreases the total electron count. Therefore, the solid composition x can be extracted directly by equating this experimentally derived electron count to the theoretical number of electrons expected for a monoclinic $(Al_xGa_{1-x})_2O_3$ unit cell, which contains four formula units. Furthermore, the composition x can be expressed as a function of the experimentally determined electron density (ρ_{el}) and unit cell volume (V_{uc}) as

$$\rho_{el} V_{uc} = 8\, x\, Z_{\mathrm{Al}} + 8(1-x)\, Z_{\mathrm{Ga}} + 12\, Z_{\mathrm{O}} \tag{5.2}$$

where Z_i denotes the atomic number of element i. However, as discussed above, X-ray reflectivity fundamentally probes the effective scattering density ρ' rather than the pure electron density (ρ_{el}). To properly account for anomalous dispersion effects at the specific incident X-ray energy, the atomic number Z_i must be replaced by the dispersion-corrected atomic scattering factor Z_i', defined as $Z_i' = Z_i + f_i'$. Therefore, the composition x derived from the XRR measurements is more accurately expressed as

$$x = \frac{12Z'_{\mathrm{O}} + 8Z'_{\mathrm{Ga}} - V_{uc}\,\rho'}{8Z'_{\mathrm{Ga}} - 8Z'_{\mathrm{Al}}} \tag{5.3}$$

The details of the total standard error in the composition, $\sigma(x)$, are provided in the Supporting Information.

Surface Structural Model with Al Incorporation

Until now it is still unclear how Ga and Al are distributed among the fractional positions. However, first-principles calculations indicate that Al has a strong preference for the octahedral sites in β-Ga_2O_3. [9] Peelaers et al. reported that for Al concentrations below 71 %, [7] the monoclinic structure remains the most stable phase, and Al predominantly occupies the octahedral positions. [1] This strong site preference also explains the unusual stability of the ordered alloy model. Despite this clear thermodynamic preference, Al does not always reach the lowest energy configuration during growth. Kinetic limitations can prevent Al from mov-

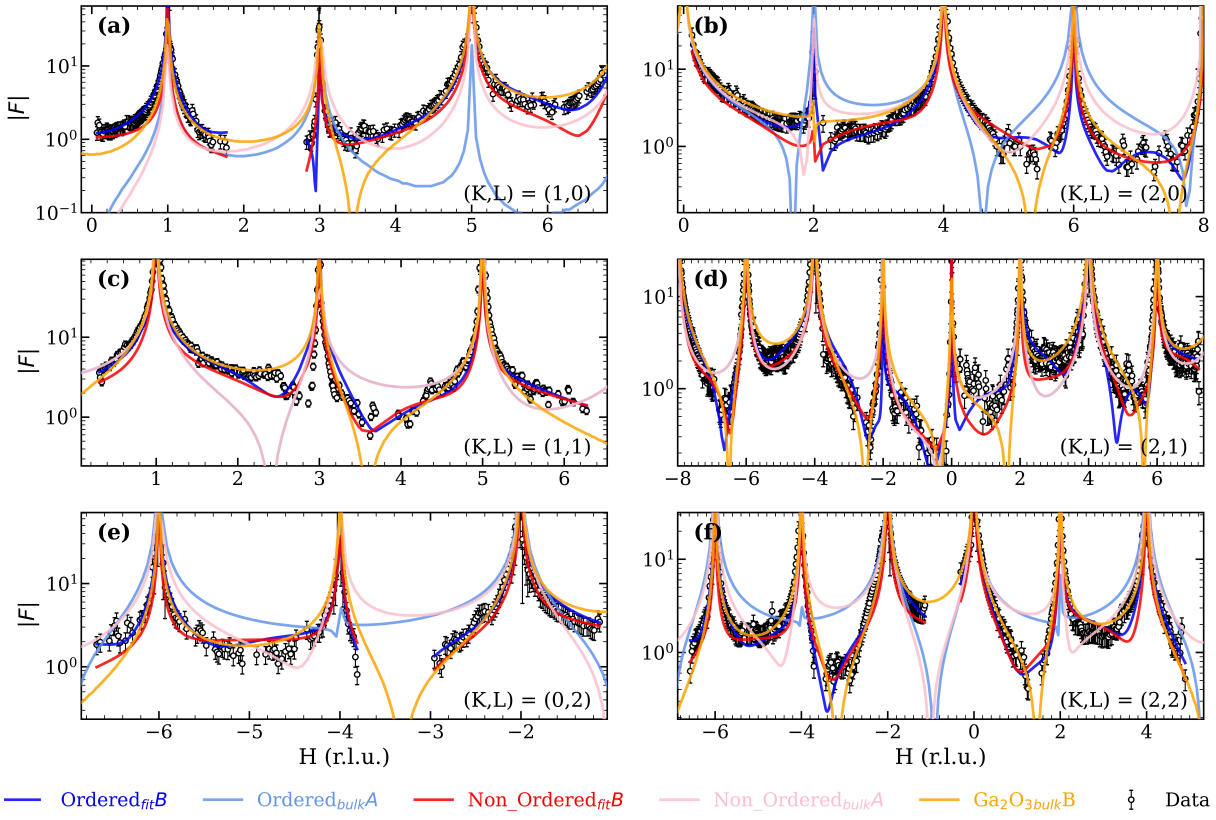


Figure 5.5: Comparison of simulated and fitted CTR data for the $(Al_xGa_{1-x})_2O_3$ (100) single crystal with Al content of $x = 0.2$. The fitted and simulated structure factor (F) for the B-terminated surface of the Ordered$_{fit}$ (blue), Non-Ordered$_{fit}$ (red), and the pure Ga_2O_{3bulk} (yellow) model. The simulated structure factor (F) for the A-terminated surface of the Ordered$_{bulk}$A (light blue), Non-Ordered$_{bulk}$A (light red) model. Experimental structure factors are shown in black with corresponding error bars. Each rod is indexed by (K, L) and plotted as a function of the out-of-plane momentum transfer in reciprocal space, H. A and B refer to the two possible surface terminations of the (100) surface.

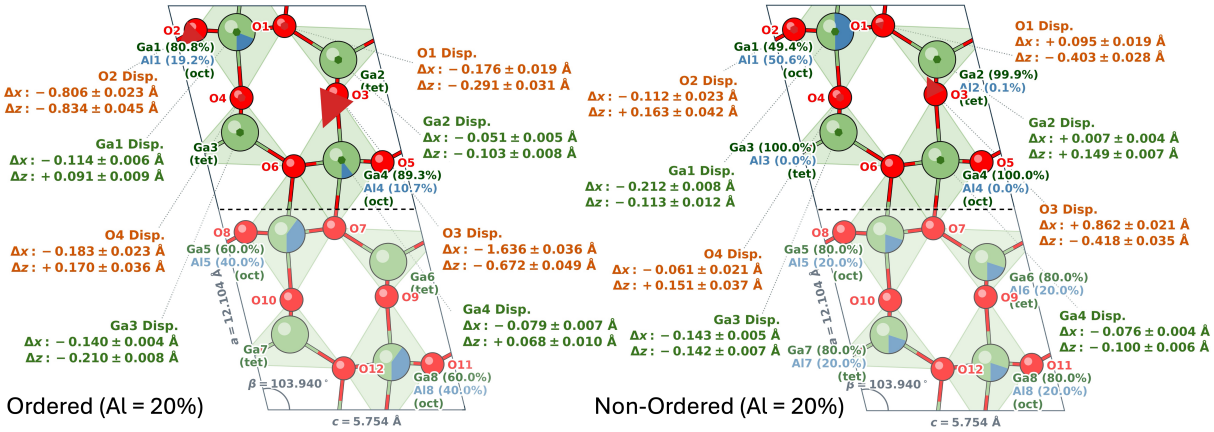


Figure 5.6: Visualization of the fitted atomic displacements (in Å) and the site occupancy (in %) results using the Ordered$_{fit}$ (left), Non-Ordered$_{fit}$ (right) model for a $(Al_xGa_{1-x})_2O_3$ (100) single crystal with the Al content of $x = 0.2$. The atomic displacements of the Ga/Al and O atoms were fitted along the [100] directions as Δx and [001] directions as Δz. The arrows indicate the displacement direction, and their lengths are proportional to the displacement magnitude, but are scaled up for clarity.

ing to octahedral sites. Migration barrier calculations show that an Al atom at the surface faces a high barrier of 1.72 eV when attempting to move from a tetrahedral to an octahedral site, while Ga requires only 0.56 eV. [50] In the bulk the mobility of Al is even more restricted, making such transitions very unlikely. While surface reconstructions and kinetic constraints during epitaxial growth can readily trap Al on tetrahedral sites, the single crystals investigated in this study were grown by the Czochralski melt-growth method. The near-equilibrium conditions and high temperatures of 1800 to 1900°C during crystal growth of $(Al_xGa_{1-x})_2O_3$ by the Czochralski method, strongly favor the stable incorporation of Al into the energetically preferred octahedral sites.

In this study, the SXRD results were analyzed by constructing several Al-alloyed surface structural models. To accurately describe the scattering from the truncated crystal surface, the total structure amplitude $|F_{tot}|$ was modeled as the scattering from the semi-infinite bulk lattice and the surface layers, as

$$|F_{tot}| = \left| \frac{F_{bulk}}{1 - \exp(i2\pi H)} + F_{surf} \right| \tag{5.4}$$

F_{bulk} is the structure factor of the underlying bulk unit cell, which was fixed to the assumed bulk structure. The fractional index H represents the momentum transfer along the surface normal. The term F_{surf} represents the structure factor of the surface layers. The atomic positions and occupancies within this region were the fitted parameters to the experimental

data.

Figure 5.4 illustrates the structural relationships between pure gallium oxide, theta-alumina (θ-Al_2O_3), and two proposed atomic configurations for Al-alloyed bulk crystal with Al content of $x = 0.2$. Pure β-Ga_2O_3 shown in Figure 5.4(a) and θ-Al_2O_3 shown in Figure 5.4(b) are isostructural with monoclinic C2/m space group, where the lattice constants for θ-Al_2O_3 are slightly smaller. Consequently, θ-Al_2O_3 can be viewed as the fully Al-substituted structural model. Figures 5.4(c) and (d) illustrate two atomic models regarding the incorporation of Al in the crystal, presented here for the case of Al-alloyed bulk crystal with Al content of $x = 0.2$. The Ordered model shown in Fig. 5.4(c) indicated a strict site preference, with Al atoms only occupying the octahedral positions within the bulk crystal, as suggested by previous first-principles studies. [9] In contrast, the Non-ordered model presented in Fig. 5.4(d) illustrates a statistical distribution, where Al atoms randomly substitute into both octahedral and tetrahedral sites. A first comparison with the unit cells of pure β-Ga_2O_3 and the θ-Al_2O_3 reveals that Al_1 tends to sit slightly below Ga1, while Al_2 preferentially positions itself slightly above Ga_2 along the surface-normal direction [100]. These positional shifts are primarily driven by the difference in ionic size between the two cations. Since the Al^{3+} ion is significantly smaller than the Ga^{3+} ion, it naturally prefers shorter metal–oxygen bond lengths. However, the surrounding oxygen network of the $(Al_xGa_{1-x})_2O_3$ lattice cannot contract symmetrically to fully accommodate the smaller dopant, causing the Al atom to shift off-center. This asymmetric relaxation allows Al to achieve its energetically favored shorter bond lengths with a specific subset of the coordinating oxygen atoms, resulting in non-equivalent bond lengths within the polyhedron.

Simulated structure factors (F_{bulk}) show that the B-terminated models agree very well with the experimentally obtained CTR datasets of Al-alloyed bulk crystal with Al content of $x = 0.2$, whereas the A-terminated models do not reproduce the measured data, as shown in Fig. 5.5 and S5. This suggests that the crystal cleaves to produce a single termination, exclusively adopting the (100)B surface. This conclusion is strongly corroborated by our AFM analysis (see Fig. S1–3), which reveals uniform terrace step heights of approximately 12 Å. Since this step height corresponds exactly to half of the unit-cell height, i.e., the spacing between two equivalent (100)B cleavage planes, it provides direct evidence against a single-terminated surface. This observation is also consistent with our previous study of the pure Ga_2O_3 (100) single-crystal surface. [97] Based on these results, we applied two proposed B-terminated models to fit the CTR data and refine the atomic positions of the topmost layers. The positions of

Ga, Al, and O atoms were refined along the [100] and [001] directions, following the same procedure as in our recent publication. [97] As shown in Fig. 5.5(a)–(f), both refined model for ordered and non-ordered B-termination reproduce the experimental structure factors well and yield low, comparable chi-square values. In contrast, the simulated using A-terminated surface, which is corresponding to the second-lowest surface-energy configuration, [9] is clearly inconsistent with the data (light blue and light red profile in Fig. 5.5).

The fitted atomic displacements and site occupancies for the structural models are summarized in Fig. 5.6. The Ga atoms exhibit only modest displacements, on the order of 0.1 Å, which is consistent with a normal surface relaxation rather than a major structural reconstruction or segregation. In contrast, the fitted O atoms show larger displacements, in some cases approaching 1 Å. However, these oxygen values should be considered as less reliable. Since X-ray scattering is dominated by the heavier Ga atoms rather than oxygen, the refined O positions are much more weakly constrained by the data and therefore carry larger uncertainties. As a result, the O displacements are more sensitive to correlations in the fit and should be interpreted with caution. However, clear trends in the refined occupancies appear across the two models. Aluminum does not prefer to occupy the tetrahedral sites. Even in the non-ordered model, where Al is expected to be distributed evenly among all sites, the fit shows a preference for the octahedral positions. All fitted results, as well as the fitted Debye-Waller factors, are listed in Table S2. The fitting was performed by allowing the top half of the surface unit cell to vary, while the remaining half was constrained to the bulk structure. This observation agrees well with results from first-principles studies. [9] However, the exact fractional position of Al is still not fully resolved in our analysis, because the scattering power of Al atoms is significantly lower than Ga atoms. As a result, small shifts in the Al position have only a minor influence on the overall diffraction intensity, which limits the sensitivity of the fit to subtle variations in the Al coordinates. The fitted and simulated results for the aluminum content of the x = 0.1 to 0.3 crystals are also shown in Fig. S6–S8 and listed in Table S3.

CONCLUSIONS

In summary, we have comprehensively characterized as-cleaved $(Al_xGa_{1-x})_2O_3$ (100) single crystals with aluminum content ranging from $x = 0$ to 0.3 using SC-XRD, SXRD, and XRR techniques. The monoclinic lattice parameters of all Al-alloyed samples were accurately refined, and the XRR and AFM results confirm that the cleaved surfaces are smooth, single-terminated, defect-free, and suitable for quantitative surface-sensitive analysis. By combining

the SC-XRD obtained lattice parameters with the electron density results, we derived the actual Al compositions of the crystals. These values deviate only slightly from the nominal compositions with minimal error $\sigma(x)$ within approximately 1 %, demonstrating that the X-ray methods are sufficiently sensitive to detect changes in electron density, as reflected in the systematic shift of the critical angle with increasing Al concentration. Structure factor simulations and AFM analysis confirm that all cleaved samples exhibit bulk-terminated (100)B surfaces, consistent with our previously reported results for cleaved β-Ga_2O_3. [97] Furthermore, CTR analysis reveals the atomic positions and occupancies of the $(Al_xGa_{1-x})_2O_3$ (x = 0.1 to 0.3) bulk crystal. The best fit results using the two proposed ordered and non-ordered models show that Al prefers octahedral sites over tetrahedral sites, which is in excellent agreement with DFT calculations. However, to further validate the bulk fractional coordinates and site occupancies of Ga and Al, complementary investigations using techniques such as PXRD and advanced electron microscopy are necessary.

The supplementary material available in A.2.1 provides the fitted atomic displacements, site occupancies, and Debye-Waller factors for both models, as well as the simulated structure factors for all A- and B-terminated surface models and the AFM analysis.

Acknowledgments

This project is funded by the Deutsche Forschungsgemeinschaft (DFG, German Research Foundation) under the project number 491040331. We acknowledge SOLEIL for provision of synchrotron radiation facilities and we would like to thank the beamline staff for assistance in using beamline SIXS under proposal 20230826. [34] We also acknowledge DESY (Hamburg, Germany), a member of the Helmholtz Association HGF, for the provision of experimental facilities, and we thank the P24 beamline staff at PETRA III for their support during beamtime under proposals 11018789/20231216. [35] Parts of this research were carried out at DESY NanoLab. [33]

Data Availability Statement

The data that support the findings of this study are available from the corresponding author upon reasonable request.

Chapter 6

Summary and Conclusion

The bulk and atomic surface structures of both pure β-Ga_2O_3 and Al-alloyed $(Al_xGa_{1-x})_2O_3$ single crystals, with Al compositions ranging from x = 0 to 0.3, cleaved along the (100) plane, were investigated in this thesis. In addition, $(Al_xGa_{1-x})_2O_3$ thin films grown on β-Ga_2O_3 (100) cleaved single-crystal substrates with 4° miscut were also studied. Since alloying β-Ga_2O_3 is a highly promising approach for band-gap engineering in ultra-wide-bandgap semiconductors, with potential applications in high-power electronics or gas sensing. Therefore, a detailed understanding of how Al incorporation influences the crystal lattice and its exact surface structure is essential for epitaxial growth, substrate preparation, and device processing.

To obtain high-quality crystallographic information, a comprehensive set of state-of-the-art synchrotron-based techniques was employed. Single-crystal X-ray diffraction (SC-XRD) and grazing-incidence X-ray diffraction (GIXRD) were performed at the P24 Chemical Crystallography beamline at PETRA III, Deutsches Elektronen-Synchrotron (DESY), Germany. [35] Surface X-ray diffraction (SXRD/CTR) and X-ray reflectivity (XRR) measurements were carried out at the SIXS beamline of the SOLEIL Synchrotron in France. [34] Most of the pre-characterization measurements were conducted at the DESY NanoLab at the Deutsches Elektronen Synchrotron (DESY) in Hamburg, [33] including LEED patterns, AFM images, and some XRD measurements.

First, we investigate the atomic surface structures of pure β-Ga_2O_3 (100) as-cleaved single crystals. This study showed that the cleaved single-crystal surface consists of a single-, bulk-terminated surface, namely the B-termination. This termination arises because the crystal naturally fractures along this plane and formed by edge-sharing oxygen octahedra, where cleaving breaks the longest and at the same time weakest Ga–O bonds in this monoclinic crystal structure. In addition, the refinement of atomic positions revealed that the surface atoms

deviate only slightly from their ideal bulk positions, indicating extremely small surface relaxation, with a maximum displacement of about 0.01 Å. AFM measurements further confirmed that the cleaved surface is composed of relatively large, flat terraces separated by step heights of about 6 Å, which corresponds to exactly half the length of the unit-cell a-axis. Owing to the crystal symmetry, this step height preserves the same B-terminated atomic structure across all terraces.

Secondly, the investigation focused on the bulk structure of the Al-alloyed $(Al_xGa_{1-x})_2O_3$ single crystals, with Al compositions ranging from x = 0 to 0.3. The monoclinic lattice parameters and the crystal quality of all Al-alloyed single crystals were accurately refined and verified using SC-XRD, together with the electron density derived from XRR, demonstrated that the actual aluminum content in the crystals can be determined with high accuracy, with an error of only about 1 %. This makes the X-ray-based approach a valuable and reliable method for determining the actual aluminum content. In addition, AFM analysis showed that the cleaved (100) surfaces are smooth and consist of terraces with step heights of about 12 Å, and that they are single-terminated with the B-termination. This shows that Al alloying does not alter the natural cleavage behavior compared with pure β-Ga_2O_3. Furthermore, CTR analysis reveals the atomic positions and occupancies of the $(Al_xGa_{1-x})_2O_3$ bulk crystal. The best fit results using the two proposed ordered and non-ordered models revealed a preference of Al occupancy at octahedral sites over tetrahedral sites, which is in excellent agreement with Density Functional Theory (DFT) calculations. However, to further validate the bulk fractional coordinates and site occupancies of Ga and Al, complementary investigations using techniques such as PXRD and advanced electron microscopy are still necessary.

Finally, MOVPE-grown $(Al_xGa_{1-x})_2O_3$ thin films on β-Ga_2O_3 (100) cleaved single-crystal substrates with 4° miscut were also studied at the P24 beamline using grazing-incident geometry. By analyzing the diffraction images, the growth mode of the films could be evaluated non-destructively from the shape and orientation of the crystal truncation rod (CTR) signals. For thin films, the CTRs remained parallel to the crystallographic surface normal, indicating strong step-step correlation and resulting in step-flow growth on the miscut substrate. In contrast, for thicker films, the CTRs tilted by approximately 4°, becoming perpendicular to the miscut surface and reflecting step-bunching as well as weaker correlation with the underlying substrate steps. Therefore, the CTR orientation provided a direct fingerprint of the film growth behavior and surface morphology.

In summary, this thesis systematically investigated all $(Al_xGa_{1-x})_2O_3$ single crystals and

bridges fundamental crystallography with the advancement of ultra-wide-bandgap semiconductor applications by achieving three of our research goals. First, it establishes the highly stable, B-terminated (100) cleaved surface of pure β-Ga_2O_3 single crystals as a reliable foundation for applications such as solar-blind UV photodetectors, which require well-defined surface conditions. Second, it demonstrates that aluminum-alloyed $(Al_xGa_{1-x})_2O_3$ single crystals preserve the crystal symmetry, structural quality, and cleavage-plane's surface termination, confirming that alloying is a structurally viable route for band-gap engineering and further device fabrication. Finally, it shows that non-destructive X-ray diffraction techniques can be used to observe step-correlation and growth modes in $(Al_xGa_{1-x})_2O_3$ thin films. This provides a powerful tool for optimizing epitaxial growth for next-generation high-power device fabrication.

Appendix A

Appendix

A.1 Surface Crystallography of As-cleaved β-Ga_2O_3(100) Crystals

A.1.1 Supporting Information : Paper I

Supplementary Information
Surface termination of β-Ga_2O_3(100) as-cleaved single crystals

Ming-Chao Kao[1,2,*], Lukas Paul Schewe[3], Arub Akhtar[4], Alina Vlad[5], Thomas F. Keller[1], Karsten Henkel[3], Saud Bin Anooz[4], Andreas Popp[4], Zbigniew Galazka[4], Jan Ingo Flege[3], Andreas Stierle[1,2], Vedran Vonk[1]
[1]Centre for X-ray and Nano Science (CXNS), Deutsches Elektronen-Synchrotron DESY, Notkestraße 85, 22607 Hamburg, Germany
[2]Fachbereich Physik, Universität Hamburg, Jungiusstraße 9, 20355 Hamburg, Germany
[3]Applied Physics and Semiconductor Spectroscopy, Brandenburg University of Technology Cottbus–Senftenberg, Cottbus, Germany
[4]Leibniz-Institut für Kristallzüchtung, Max-Born-Straße 2, D-12489 Berlin, Germany
[5]Synchrotron SOLEIL, L'Orme des Merisiers, 91190 Saint-Aubin, France

[*]Corresponding author: vedran.vonk@desy.de

January 7, 2026

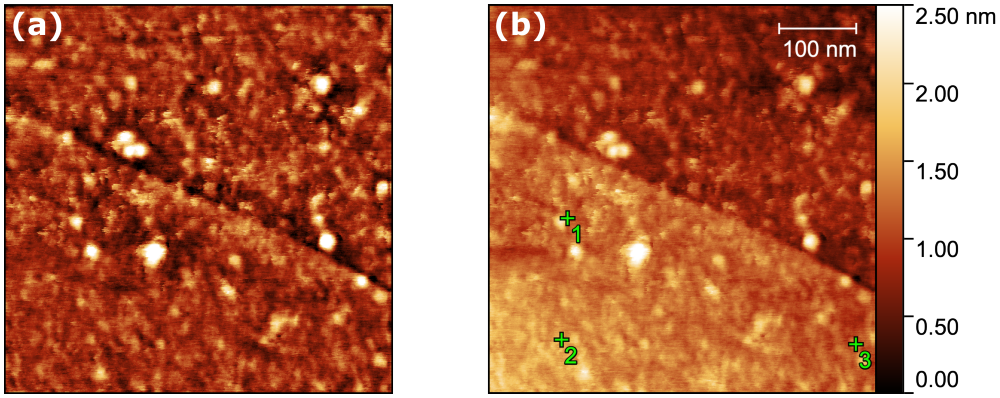


FIG. S1: (a) AFM raw image of a terrace on the as-cleaved surface before processing. (b) The same AFM image after processing. Three points on a single plane, corresponding to features at the same height, were manually selected (indicated by green markers). As the upper and lower planes are not parallel and exhibit an inclined trend, levelling was performed by defining the reference plane using these three points on the chosen terrace.

The raw images were flattened, corrected for tilting and levelled using the Gwyddion software.[1] Levelling was done by manually selecting three points at the same height on a single terrace (indicated by green markers). For the analysis of step height line profiles, a Boltzmann bent step function is employed, which can be expressed as follows:

$$y(x) = y_0 + \frac{h}{1+\exp\left(\frac{x-x_0}{w}\right)} + \alpha x + \beta x^2 \tag{S1}$$

In the Boltzmann bent step function, the parameter x_0 represents the position along the x-axis at which the center of the step occurs, while y_0 sets the baseline offset of the function on the y-axis. The width of the step transition is given by w, with smaller values indicating a sharper, steeper step and larger values a more gradual change. The step height h determines the difference in function value from the lower to the upper plateau at the step. The parameters α and β account for background trends in the data, with α correcting for any linear (sloped) baseline and β capturing any quadratic (parabolic) curvature in the background outside of the step region. Together, these parameters allow the model to accurately represent a step-like feature as our step height data, even in the presence of non-flat backgrounds. The particle-like features occur with a surface coverage, which we estimate to be in the range 5-10%, which makes their contribution to the CTRs minor. This is also evident from the fitting procedure which does not explicitly include a deviation from a perfect surface; SXRD is in principle sensitive to such imperfections, albeit for large coverage.

Figures S3 and S4 demonstrate that the CTRs for the symmetry-related terminations (D, G) in green and (E, I) in purple are identical in both figures and overlap completely. Similarly, the CTRs for terminations (B, H) are also identical due to their symmetry. The symmetry is also evident in the matching χ^2 values listed in Table S2. The slight variations in the second decimal place of the χ^2 values are attributed to numerical rounding or computational precision. This also shows that neighboring terraces, separated by steps of half the unit cell length along the a-axis, produce exactly the same CTR signals.

TABLE S1: Fitting parameters of step height line profiles using the Boltzmann bent step function.

Parameter	Profile 1	Profile 2	Profile 3	Profile 4
x_0	293.35 ±3.39Å	304.07 ±2.97Å	375.21 ±4.21Å	351.57 ±1.90Å
y_0	8.54 ±0.11Å	9.55 ±0.10Å	9.89 ±0.11Å	7.86 ±0.07Å
w	31.37 ±6.65Å	19.47 ±5.53Å	51.36 ±8.21Å	29.85 ±3.57Å
h	6.11 ±0.05Å	5.15 ±0.36Å	6.28 ±0.04Å	6.72 ±0.24Å
α	-0.00193 ±0.00111	-0.00067 ±0.00089	-0.00054 ±0.00080	-0.00173 ±0.00050
β	6.18 ±1.87Å	1.55 ±1.73Å	2.01 ±1.32Å	3.35 ±0.93Å

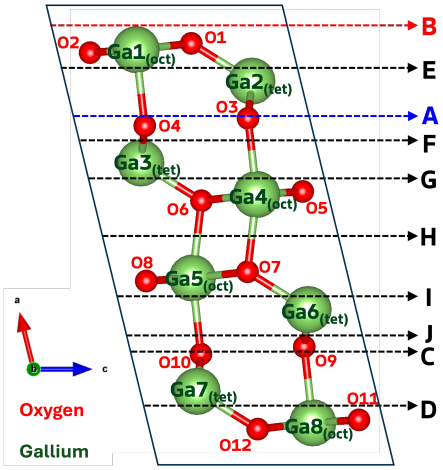


FIG. S2: All possible surface terminations of the β-Ga_2O_3(100) surface, where terminations B to G are related to H to D due to symmetry.

The CTR fitting was performed using the ROD software package.[2] The quality of the fit was obtained by calculating the χ^2 value, as shown in Table S2, which measures the agreement between the observed and calculated intensities based on the current set of fit parameters, as

$$\chi^2 = \frac{1}{N-\mathbf{p}} \sum_{i=1}^{N} \left(\frac{|F_i^{\text{obs}}| - s|F_i^{\text{calc}}|}{\sigma(F_i^{\text{obs}})} \right)^2 \tag{S2}$$

And the R-factor, which quantifies the relative difference between the observed and calculated structure factor amplitudes, is define as

$$R = \frac{\sum_{i=1}^{N} \left| |F_i^{\text{obs}}| - s|F_i^{\text{calc}}| \right|}{\sum_{i=1}^{N} |F_i^{\text{obs}}|} \tag{S3}$$

where

- N is the total number of measurements,
- s is the overall scale factor,
- **p** is the number of fit parameters,
- σ_i is the standard deviation of F_i^{obs},
- $|F_i^{\text{obs}}|$ is the observed structure factor amplitude,
- $|F_i^{\text{calc}}|$ is the calculated structure factor amplitude, also dependent on the parameter.

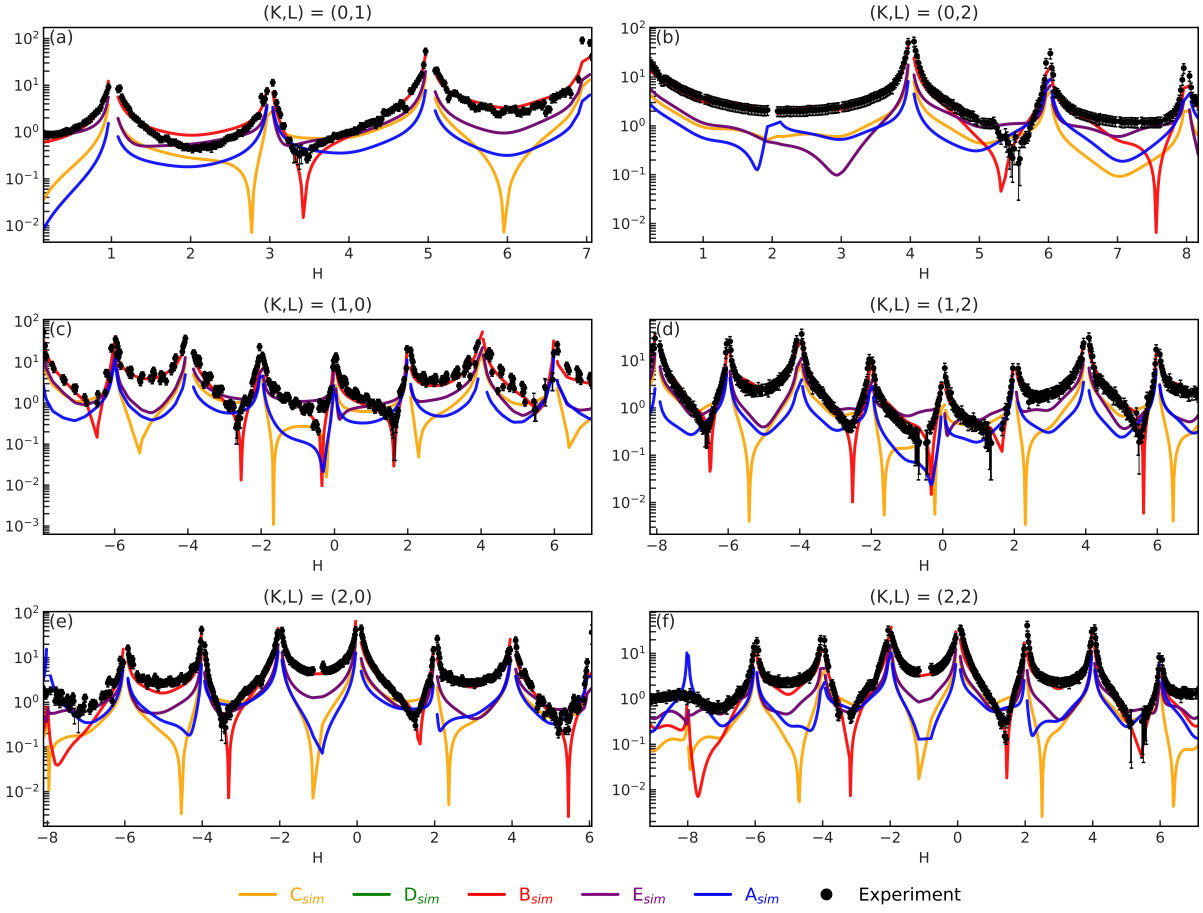


FIG. S3: Experimental (symbols) and simulated CTRs (lines) for different (100) surface terminations, as indicated in Fig. S2. The curves for terminations D and E completely overlap because they correspond to exactly identical CTRs due to surface terminations which are related by symmetry.

Termination	Chi-square	Normalized	R-factor
B	9492.8584	3.4283	0.2640
E	26017.2773	9.3959	0.6460
A	40843.5820	14.7503	0.8000
F	37586.6484	13.5741	0.7500
G	26014.4785	9.3949	0.6460
H	9492.8574	3.4283	0.2640
I	26017.2813	9.3959	0.6460
J	37588.0430	13.5746	0.7500
C	37342.9922	13.4861	0.7510
D	26014.4785	9.3949	0.6460

TABLE S2: Comparison between the different bulk-terminations A to J and the experimental CTR data. The listed χ^2 and R values are obtained by fitting only the scale factor s, as defined in Eqs. S2 and S3

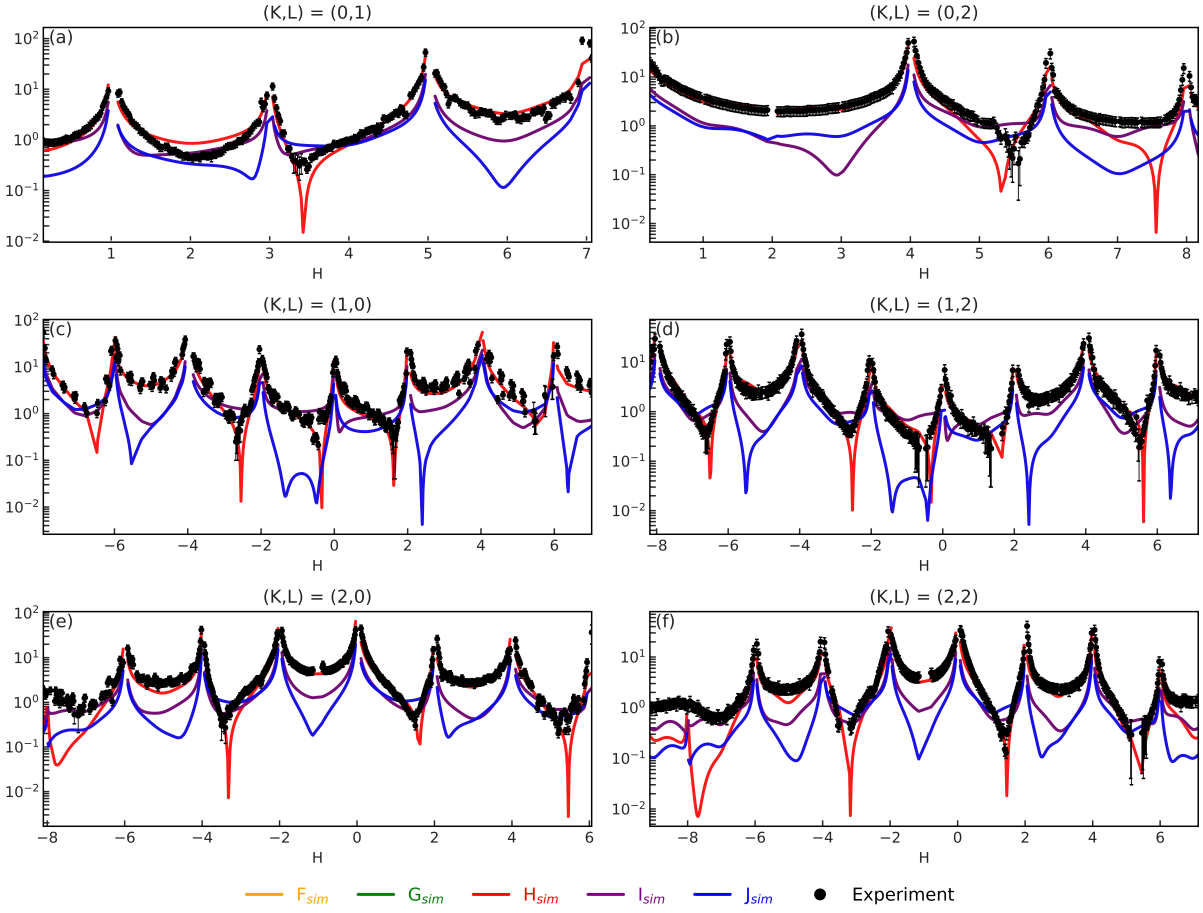


FIG. S4: Experimental (symbols) and simulated CTRs (lines) for different (100) surface terminations, as indicated in Fig. S2. The curves for terminations F J and G I completely overlap because they correspond to exactly identical CTRs due to surface terminations which are related by symmetry.

Bulk unit cell				B-termination					
Atom	x	y	z	x (surface normal)	y	z	DW (Å^2)	x-displacement (Å)	z-displacement (Å)
O1	1.000	0.5	0.564	0.9934 ± 0.0013	0.5	0.5490 ± 0.0028	0.522 ± 0.041	-0.0807	-0.0868
O2	0.990	0.5	0.109	0.9945 ± 0.0011	0.5	0.1138 ± 0.0025	0.522 ± 0.041	0.0561	0.0279
Ga1(oct)	0.985	0.0	0.314	0.9765 ± 0.0003	0.0	0.3163 ± 0.0009	1.066 ± 0.176	-0.1034	0.0132
Ga2(tet)	0.916	0.5	0.795	0.9196 ± 0.0003	0.5	0.7912 ± 0.0008	1.066 ± 0.176	0.0441	-0.0223
O3	0.831	0.0	0.744	0.8293 ± 0.0011	0.0	0.7330 ± 0.0025	0.42	-0.0208	-0.0640
O4	0.822	0.0	0.256	0.8252 ± 0.0012	0.0	0.2544 ± 0.0028	0.42	0.0387	-0.0095
Ga3(tet)	0.737	0.5	0.205	0.7332 ± 0.0003	0.5	0.1974 ± 0.0008	0.31	-0.0462	-0.0438
Ga4(oct)	0.668	0.0	0.686	0.6684 ± 0.0003	0.0	0.6818 ± 0.0007	0.31	0.0045	-0.0242
O5	0.663	0.5	0.891	0.6633 ± 0.0010	0.5	0.891	0.42	0.0038	
O6	0.653	0.5	0.436	0.6457 ± 0.0010	0.5	0.436	0.42	-0.0887	
O7	0.500	0.0	0.564	0.5042 ± 0.0010	0.0	0.564	0.42	0.0509	
O8	0.490	0.0	0.109	0.4863 ± 0.0009	0.0	0.109	0.42	-0.0455	
Ga5(oct)	0.485	0.5	0.314	0.485	0.5	0.314	0.31		
Ga6(tet)	0.416	0.0	0.795	0.416	0.0	0.795	0.31		
O9	0.331	0.5	0.744	0.331	0.5	0.744	0.42		
O10	0.322	0.5	0.256	0.322	0.5	0.256	0.42		
Ga7(tet)	0.237	0.0	0.205	0.237	0.0	0.205	0.31		
Ga8(oct)	0.168	0.5	0.686	0.168	0.5	0.686	0.31		
O11	0.163	0.0	0.891	0.163	0.0	0.891	0.42		
O12	0.153	0.0	0.436	0.153	0.0	0.436	0.42		

TABLE S3: Fractional positions (x, y, z) and isotropic Debye-Waller parameters (DW) of the atoms in the bulk β-Ga_2O_3 unit cell and fitted positions of the atoms in the near-surface of the B-termination as indicated in Fig. S2B. The DW parameters (without error bar) are taken from literature.[3] All fractional co-ordinates are defined with respect to a monoclinic cell with: a = 12.214 Å, b = 3.037 Å, c = 5.798 Å, $\alpha = 90^\circ$, $\beta = 103.83^\circ$, and $\gamma = 90^\circ$. Please note that the x-direction is along the surface normal. The chi-square of the fit B is 3297.77, the normalised chi-square is 1.20, and the R-factor is 0.199.

Bond distance	Bermudez et al. (Å)	This study (Å)
$Ga2_{(tet)}$–O1	1.844	1.84
$Ga2_{(tet)}$–O2	1.843	1.88
$Ga2_{(tet)}$–O3	1.839	1.87
$Ga1_{(oct)}$–O1	1.974	2.01
$Ga1_{(oct)}$–O2	1.978	1.96

TABLE S4: Bond distances for the topmost gallium atoms $Ga1_{oct}$ and $Ga2_{tet}$ to their nearest oxygen neighbors, compared with the values reported by Bermudez et al.[4] The 3σ error bar on the experimental values is estimated to be 0.02 Å.

References

[1] D. Nečas and P. Klapetek, Open Physics **10**, 181 (2012).
[2] E. Vlieg, "A concise rod manual," (2001).
[3] J. Åhman, G. Svensson, and J. Albertsson, Crystal Structure Communications **52**, 1336 (1996).
[4] V. Bermudez, Chemical Physics **323**, 193 (2006).

A.2 X-ray study of $(Al_xGa_{1-x})_2O_3$ single crystals and their (100) cleave plane

A.2.1 Supporting Information : Paper II

Supplementary Information
Surface termination of β-Ga_2O_3(100) as-cleaved single crystals

Ming-Chao Kao,[1,2,*] Lukas Paul Schewe,[3] Arub Akhtar,[4] Luis Felipe Mochalski,[1,2] Luisa Wartner,[1,2] Carsten Paulmann,[1,2] Alina Vlad,[5] Karsten Henkel,[3] Saud Bin Anooz,[4] Andreas Popp,[4] Zbigniew Galazka,[4] Jan Ingo Flege,[3] Andreas Stierle,[1,2] Vedran Vonk,[1]

[1]Centre for X-ray and Nano Science (CXNS), Deutsches Elektronen-Synchrotron DESY, Notkestraße 85, 22607 Hamburg, Germany
[2]Fachbereich Physik, Universität Hamburg, Jungiusstraße 9, 20355 Hamburg, Germany
[3]Applied Physics and Semiconductor Spectroscopy, Brandenburg University of Technology Cottbus–Senftenberg, Cottbus, Germany
[4]Leibniz-Institut für Kristallzüchtung, Max-Born-Straße 2, D-12489 Berlin, Germany
[5]Department of Earth System Sciences, University of Hamburg, Grindelallee 48, 20146 Hamburg, Germany
[6]Synchrotron SOLEIL, L'Orme des Merisiers, 91190 Saint-Aubin, France

[*]Corresponding author: vedran.vonk@desy.de

June 19, 2026

AFM Analysis

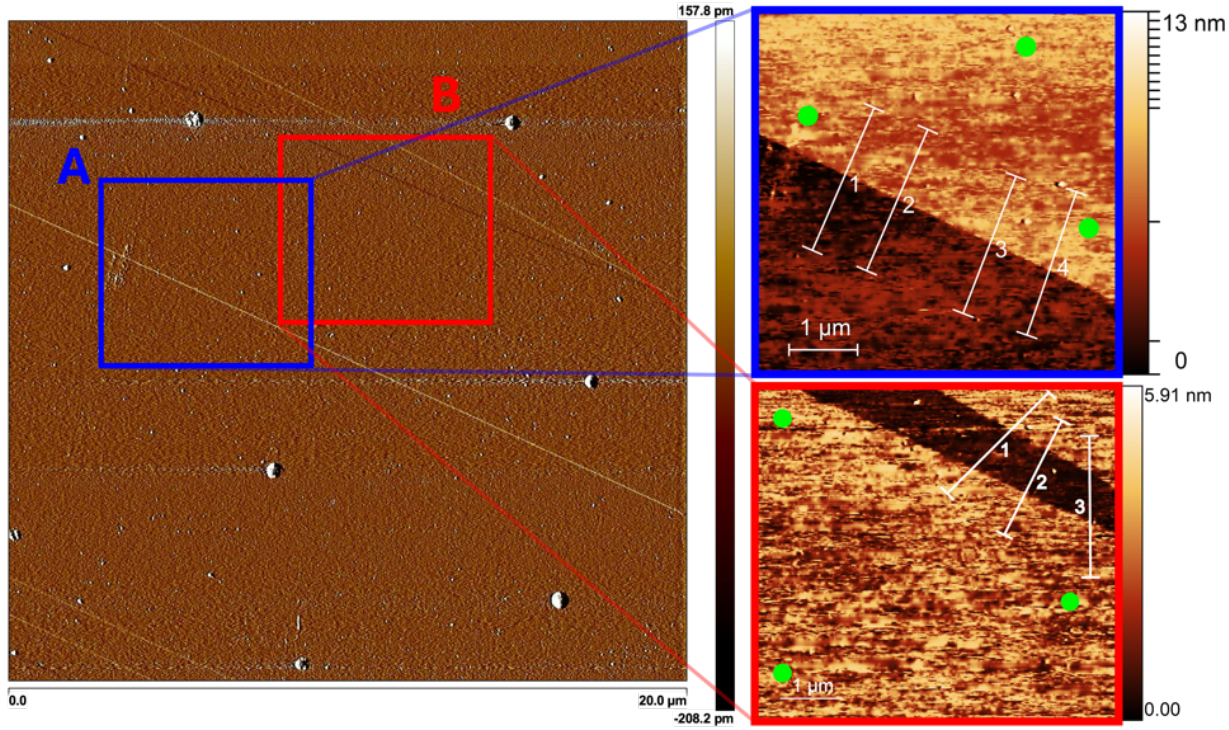


FIG. S1: AFM raw image (left) of the terrace structure on the as-cleaved surface. Areas A (blue box) and B (red box) were selected for detailed analysis of the terrace height. On the right side, the top and bottom panels show the selected areas A and B, respectively. Three points on the same plane, indicated by green markers, were manually selected for three-point leveling.

The raw images were flattened, corrected for tilting and levelled using the Gwyddion software.[1] Levelling was done by manually selecting three points at the same height on a single terrace (indicated by green markers). For the analysis of step height line profiles, a Boltzmann bent step function is employed, which can be expressed as follows:

$$y(x) = y_0 + \frac{h}{1+\exp\left(\frac{x-x_0}{w}\right)} + \alpha x + \beta x^2 \tag{S1}$$

In the Boltzmann bent step function, the parameter x_0 represents the position along the x-axis at which the center of the step occurs, while y_0 sets the baseline offset of the function on the y-axis. The width of the step transition is given by w, with smaller

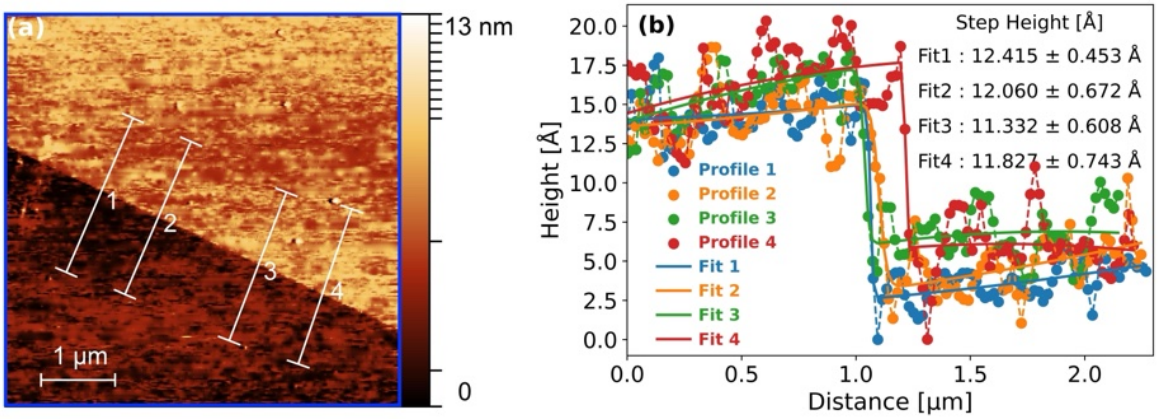


FIG. S2: (a) AFM image acquired from the selected area A of the as-cleaved (100)-oriented single crystal of (x = 0.2) Al-doped β-Ga_2O_3, illustrating the surface morphology and step structure. Four representative line profiles are indicated. (b) Height profiles corresponding to the four lines marked in (a), together with the corresponding fits. The profiles indicate a step height of approximately one unit cell.

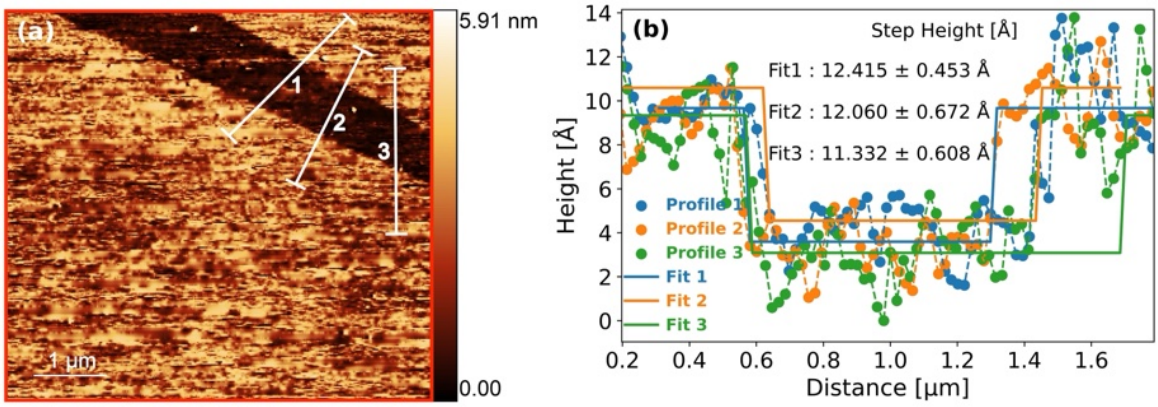


FIG. S3: AFM image acquired from the selected area B of the as-cleaved (100)-oriented single crystal of (x = 0.2) Al-doped β-Ga_2O_3, showing the surface morphology and step structure. Three representative line profiles are indicated. (b) Height profiles corresponding to the three lines marked in (a), together with the corresponding fits. The profiles indicate a step height of approximately one unit cell.

values indicating a sharper, steeper step and larger values a more gradual change. The step height h determines the difference in function value from the lower to the upper plateau at the step. The parameters α and β account for background trends in the data, with α correcting for any linear (sloped) baseline and β capturing any quadratic (parabolic) curvature in the background outside of the step region. Together, these parameters allow the model to accurately represent a step-like feature as our step height data, even in the presence of non-flat backgrounds. The particle-like features occur with a surface coverage, which we estimate to be in the range 5-10%, which makes their contribution to the CTRs minor. This is also evident from the fitting procedure which does not explicitly include a deviation from a perfect surface; SXRD is in principle sensitive to such imperfections, albeit for large coverage.

Total standard error in the composition, $\sigma(x)$:
By applying standard error-propagation principles, the total standard error of the quantified aluminum composition is obtained from the partial derivatives $\frac{\partial x}{\partial \rho'} = -\frac{V_{uc}}{8Z'_{\mathrm{Ga}} - 8Z'_{\mathrm{Al}}}$ and $\frac{\partial x}{\partial V_{uc}} = -\frac{\rho'}{8Z'_{\mathrm{Ga}} - 8Z'_{\mathrm{Al}}}$ and the total standard error of the composition, $\sigma(x)$, is given by

$$\sigma(x) = \frac{1}{\left|8Z'_{\mathrm{Ga}} - 8Z'_{\mathrm{Al}}\right|} \sqrt{V_{uc}^2 \sigma^2(\rho') + (\rho')^2 \sigma^2(V_{uc})} \tag{S2}$$

where $\sigma^2(\rho')$ is the variance of the experimentally determined scattering density, and $\sigma^2(V_{uc})$ is the variance of the experimentally determined unit cell volume.

X-ray reflectivity (XRR) Data and Analysis

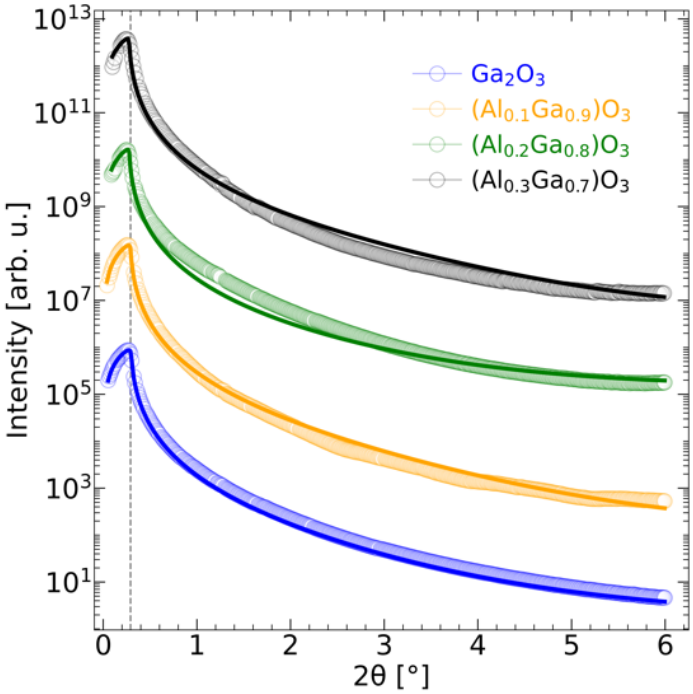


FIG. S4: X-ray reflectivity (XRR) raw and fitted profiles of $(Al_xGa_{1-x})_2O_3$ (100) bulk single crystals with varying aluminum content (x = 0 to 0.3). The specular reflected intensity raw data are shown as a function of the reflection angle 2θ (open circles), and the fitted profiles (solid lines) for pure β-Ga_2O_3 (blue), $(Al_{0.1}Ga_{0.9})_2O_3$ (yellow), $(Al_{0.2}Ga_{0.8})_2O_3$ (green), and $(Al_{0.3}Ga_{0.7})_2O_3$ (black).

TABLE S1: Fitted X-ray Reflectivity (XRR) parameters extracted from GenX for $(Al_xGa_{1-x})_2O_3$ single crystals.

Parameter [Unit]	**Nominal Al (x)**	**Fitted Value**	**Error** $(-\Delta, +\Delta)$
Substrate Density, ρ [Å^{-3}]	0	1.924×10^{-2}	$(-5.680 \times 10^{-13}, +4.997 \times 10^{-5})$
	0.1	2.970×10^{-2}	$(-1.327 \times 10^{-4}, +3.123 \times 10^{-17})$
	0.2	3.025×10^{-2}	$(-2.139 \times 10^{-4}, +6.939 \times 10^{-17})$
	0.3	3.000×10^{-2}	$(-1.991 \times 10^{-4}, +2.151 \times 10^{-16})$
Surface Roughness, σ [Å]	0	0.362	$(-4.038 \times 10^{-14}, +8.852 \times 10^{-1})$
	0.1	0.955	$(-6.640 \times 10^{-1}, +7.460 \times 10^{-1})$
	0.2	0.996	-
	0.3	1.187	$(-1.120 \times 10^{0}, +1.448 \times 10^{0})$
Electron Density, ρ_e [e/Å^3]	0	1.6635	$(-0.0000, +0.0043)$
	0.1	1.5944	$(-0.0071, +0.0000)$
	0.2	1.5690	$(-0.0111, +0.0000)$
	0.3	1.5017	$(-0.0100, +0.0000)$

Surface X-ray Diffraction (SXRD) Data and Analysis

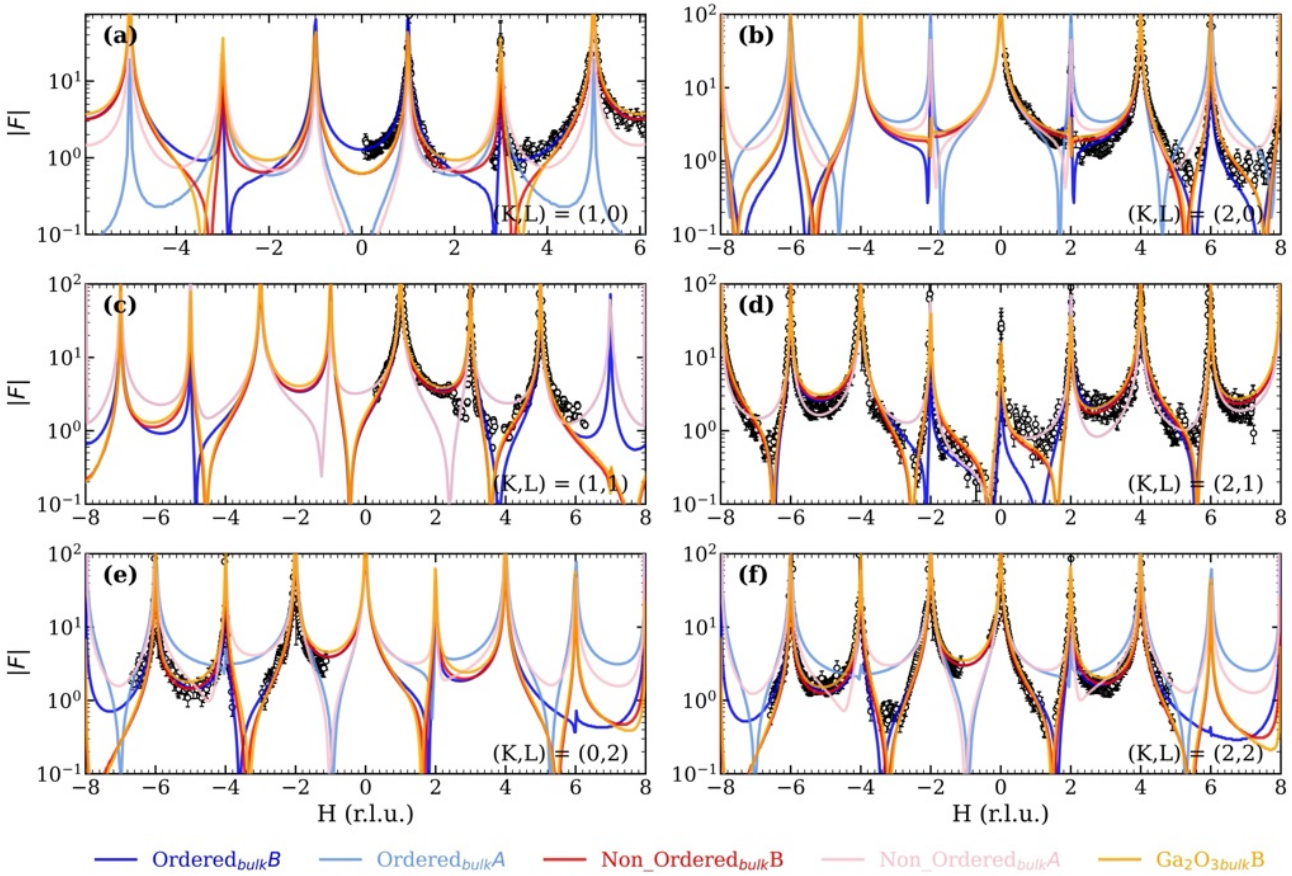


FIG. S5: Comparison of the simulated structure factor (F) of the Ordered$_{bulk}$, Non-Ordered$_{bulk}$ (red), and the pure Ga_2O_{3bulk} model with A- & B- termination for the $(Al_xGa_{1-x})_2O_3$ (100) single crystal with Al content (x = 0.2). Experimental structure factors are shown in black with corresponding error bars. Each rod is indexed by (K,L) and plotted as a function of the out-of-plane momentum transfer in reciprocal space, H. A and B refer to the two possible surface terminations of the (100) surface.[2]

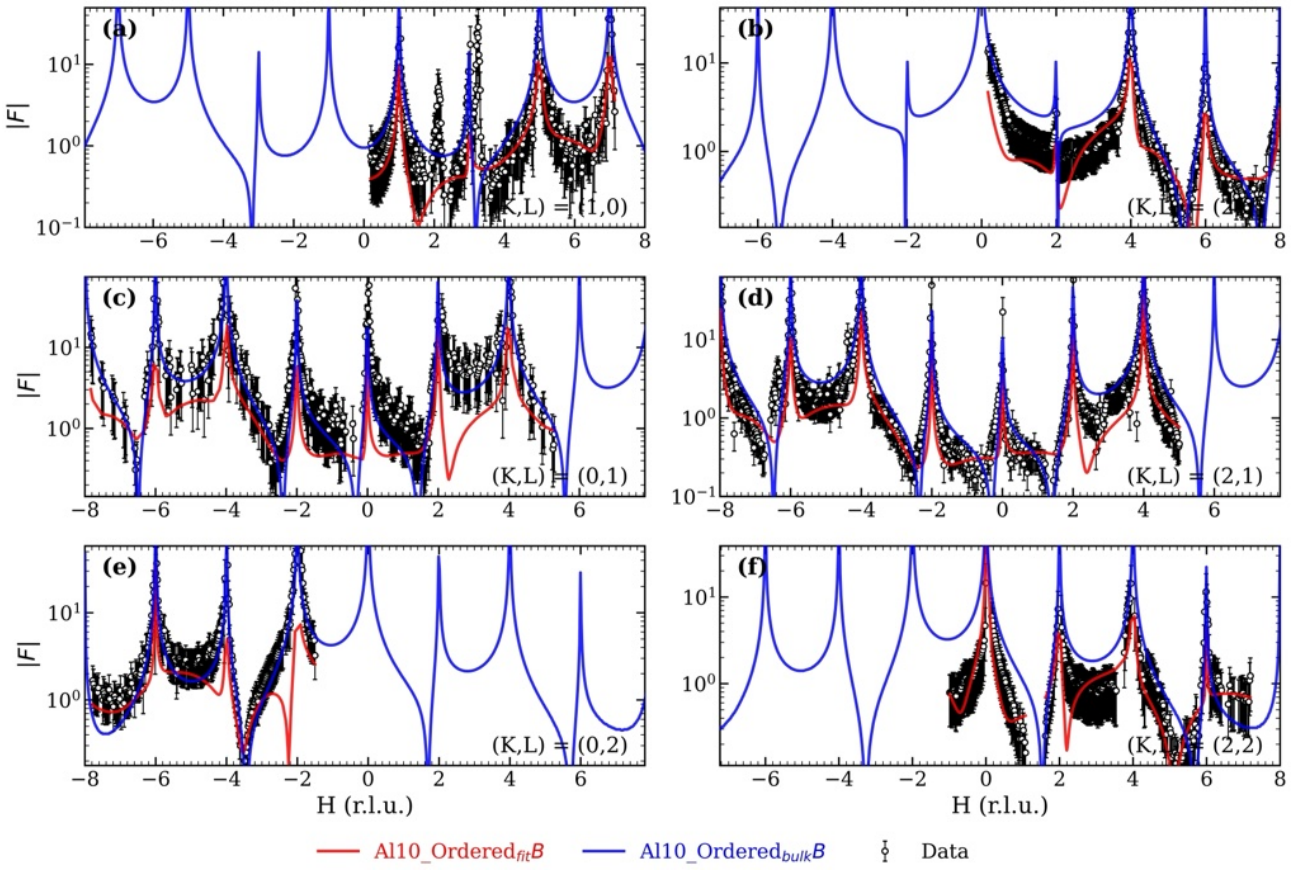


FIG. S6: Comparison of the fitted and simulated structure factor (F) of the Ordered$_{fit}$ (red), and Ordered$_{bulk}$ (blue) models of the $(Al_xGa_{1-x})_2O_3$ (100) single crystal with Al content (x = 0.1). Experimental structure factors are shown in black with corresponding error bars. Each rod is indexed by (K,L) and plotted as a function of the out-of-plane momentum transfer in reciprocal space, H. B refers to the surface terminations of the as-cleaved (100) surface.[2]

Model	Ordered				Non-ordered			
Atom	x-dis. (Å)	z-dis. (Å)	DW (Å^2)	Occ. (%)	x-dis. (Å)	z-dis. (Å)	DW (Å^2)	Occ. (%)
O1	−0.177(19)	−0.291(31)	0.000(32)	100.0	0.095(19)	−0.403(28)	0.010(25)	100.0
O2	−0.806(23)	−0.834(45)	0.000(32)	100.0	−0.112(23)	0.163(42)	0.010(25)	100.0
Ga1(oct)	−0.113(6)	0.091(9)	0.000(7)	80.8	−0.212(8)	−0.113(12)	1.193(14)	49.4
Al1(oct)			0.000(7)	19.2(15)			1.193(14)	50.6(17)
Ga2(tet)	−0.051(5)	−0.103(8)	0.000(7)	100.0	0.007(4)	0.149(7)	1.193(14)	99.9
Al2(tet)	x	x	x	x	x		1.193(14)	0.1(23)
O3	−1.636(37)	−0.672(49)	0.42	100.0	0.862(21)	−0.418(35)	0.42	100.0
O4	−0.183(23)	0.170(36)	0.42	100.0	−0.061(21)	0.151(37)	0.42	100.0
Ga3(tet)	−0.140(5)	−0.210(8)	0.31	100.0	−0.143(5)	−0.143(7)	0.31	100.0
Al3(tet)	x	x	x	x	x		0.31	0.0(11)
Ga4(oct)	−0.079(7)	0.068(10)	0.31	89.4	−0.076(4)	−0.100(6)	0.31	100.0
Al4(oct)			0.31	10.7(16)			0.31	0.0(13)
O5			0.42	100.0			0.42	100.0
O6			0.42	100.0			0.42	100.0

TABLE S2: Structural parameters for Al-alloyed bulk crystal with Al content of $x = 0.2$ derived from two distinct models: ordered and non-Ordered. Reported values include fitted displacements along the x (surface normal) and z axes, followed by Debye-Waller (DW) factors, and Ga/Al site occupancies. The occupancies were constrained such that Occ.(Ga) + Occ.(Al) = 1 at each site, therefore, the reported error bar is the same for both values. Fitted values are presented with associated error bars. The DW parameters (without error bar) are taken from literature.[3, 4]

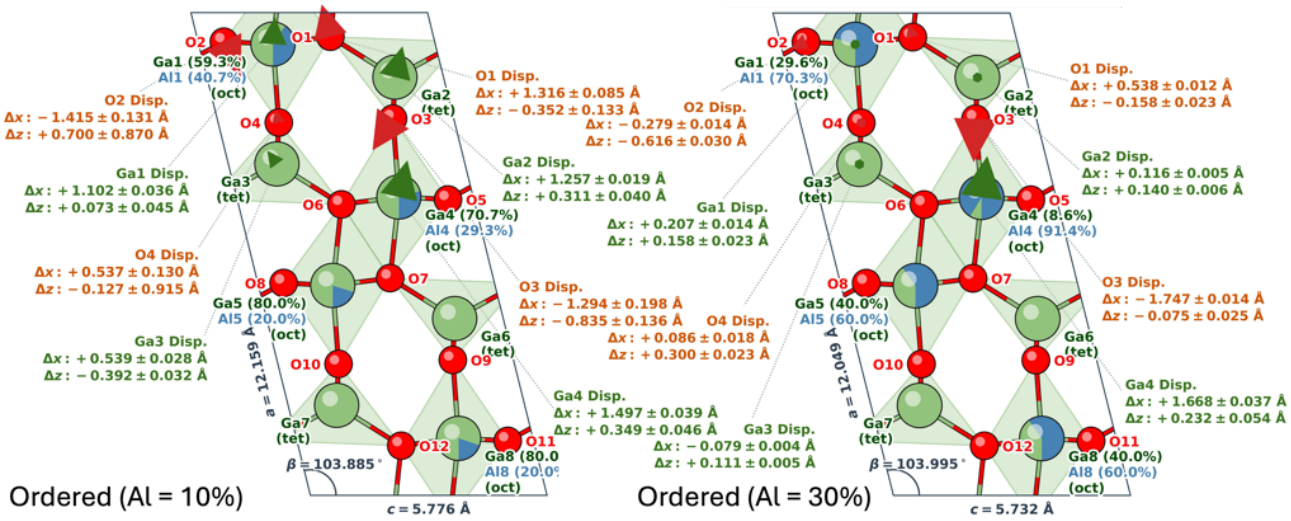


FIG. S7: Visualization of the fitted atomic displacements (in Å) and the site occupancy (in %) obtained from the Ordered x = 0.1 (left), x = 0.3 (right) models, the corresponding fitted CTRs, is shown in Fig S6 and Fig S8. The fitting was performed by allowing the top half of the surface unit cell to vary, while the remaining half was constrained to the bulk structure. Detailed results are listed in Table S3.

Model	x = 0.1 Ordered$_{fit}$B				x = 0.3 Ordered$_{fit}$B			
Atom	x-dis. (Å)	z-dis. (Å)	DW (Å^2)	Occ. (%)	x-dis. (Å)	z-dis. (Å)	DW (Å^2)	Occ. (%)
O1	1.313(85)	−0.352(133)	0.000(938)	100.0	0.542(12)	−0.155(23)	0.014(122)	100.0
O2	−1.410(134)	0.699(872)	0.000(938)	100.0	−0.277(12)	−0.619(29)	0.014(122)	100.0
Ga1(oct)	1.106(36)	0.075(46)	1.20(34)	59.3	0.205(12)	0.160(23)	0.005(37)	29.7
Al1(oct)			1.20(34)	40.7(44)			0.005(37)	70.4(11)
Ga2(tet)	1.252(24)	0.312(40)	1.20(34)	100.0	0.120	0.138(11)	0.005(37)	100.0
Al2(tet)	x	x	x	x	x	x	x	x
O3	−1.289(195)	−0.838(133)	0.42	100.0	−1.747(12)	−0.075(23)	0.42	100.0
O4	0.535(134)	−0.127(913)	0.42	100.0	0.084(24)	0.298(23)	0.42	100.0
Ga3(tet)	0.535(24)	−0.393(35)	0.31	100.0	−0.084	0.109(11)	0.31	100.0
Al3(tet)	x	x	x	x	x	x	x	x
Ga4(oct)	1.496(36)	0.347(46)	0.31	70.7	1.663(36)	0.229(52)	0.31	8.6
Al4(oct)			0.31	29.4(44)			0.31	91.4(6)
O5	0.486(146)		0.42	100.0	−0.253(12)		0.42	100.0
O6	0.839(97)		0.42	100.0	−0.169(12)		0.42	100.0

TABLE S3: Structural parameters fitted using the Ordered models for Al contents of x = 0.1 and 0.3. The corresponding fitted CTRs, is shown in Fig S6 and Fig S8, visualization of the fitted atomic displacements and the site occupancy is as Fig S7. Reported values include fitted displacements along the *x* (surface normal) and *z* axes, followed by Debye-Waller (DW) factors, and Ga/Al site occupancies. The occupancies were constrained such that Occ.(Ga) + Occ.(Al) = 1 at each site, therefore, the reported error bar is the same for both values. Fitted values are presented with associated error bars. The DW parameters (without error bar) are taken from literature.[3, 4]

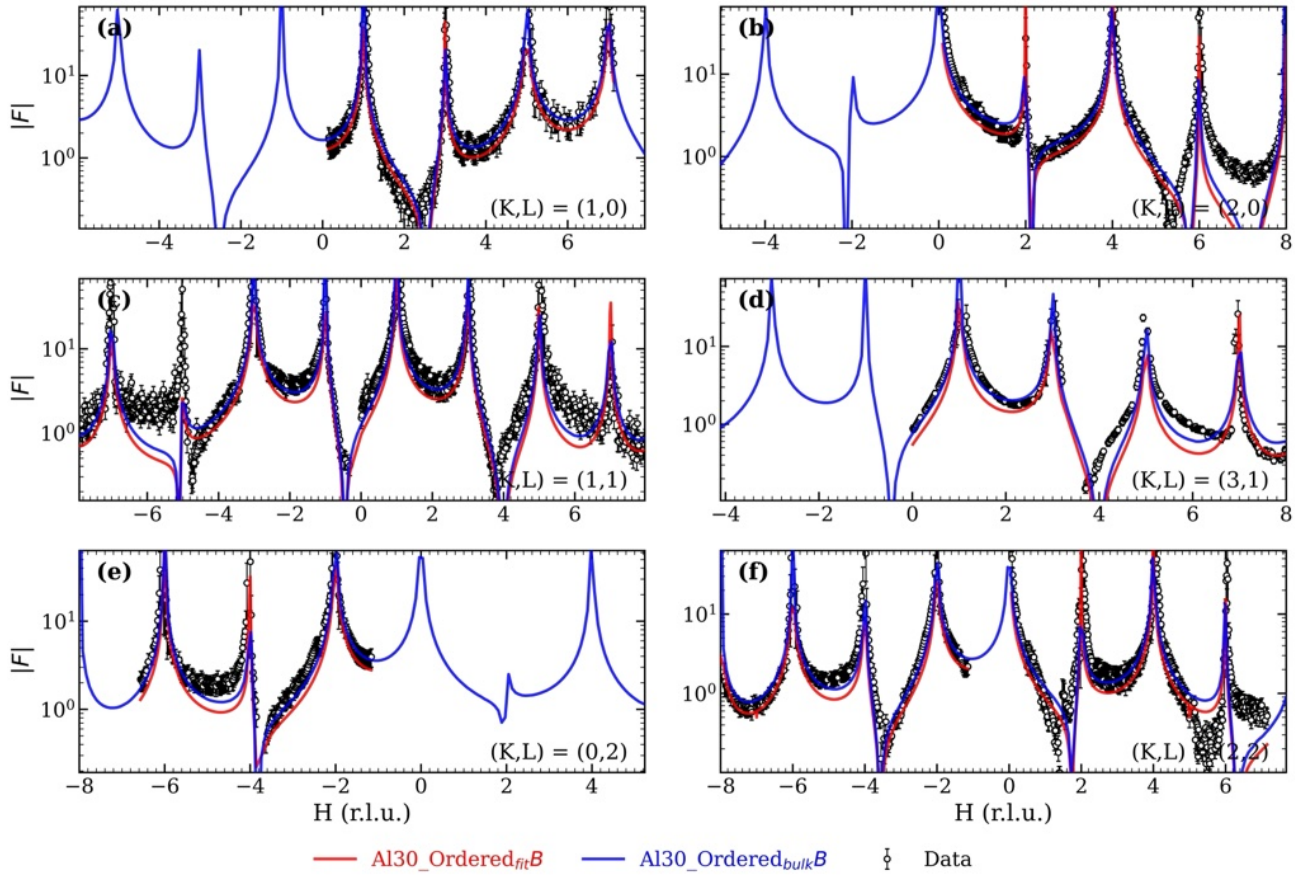
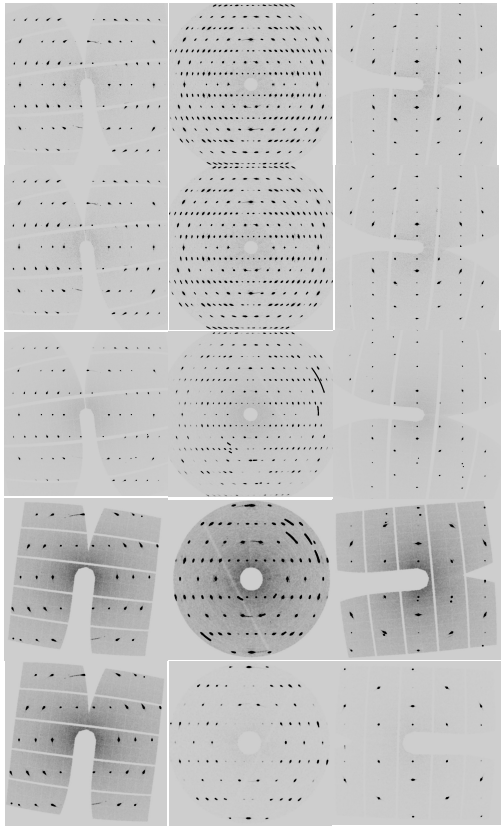
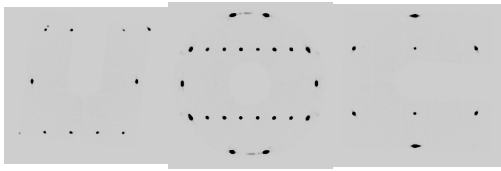


FIG. S8: Comparison of the fitted and simulated structure factor (F) of the Ordered$_{fit}$ (red), and Ordered$_{bulk}$ (blue) models of the $(Al_xGa_{1-x})_2O_3$ (100) single crystal with Al content (x = 0.3). Experimental structure factors are shown in black with corresponding error bars. Each rod is indexed by (K,L) and plotted as a function of the out-of-plane momentum transfer in reciprocal space, H. B refers to the surface terminations of the as-cleaved (100) surface.[2]

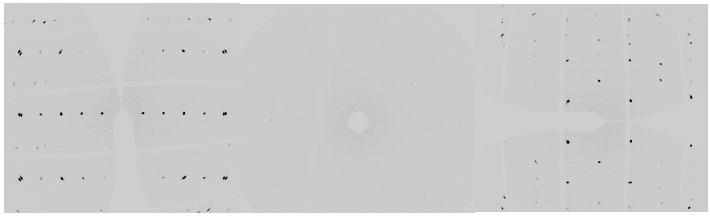
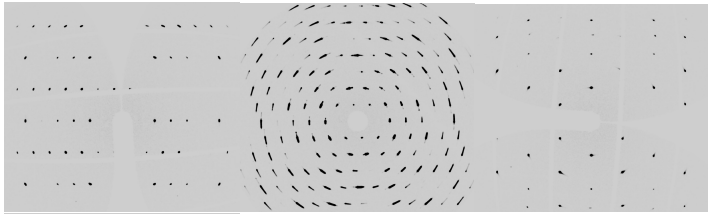
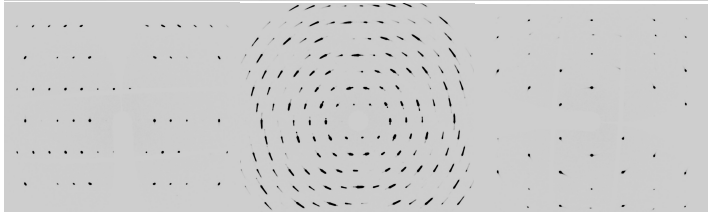
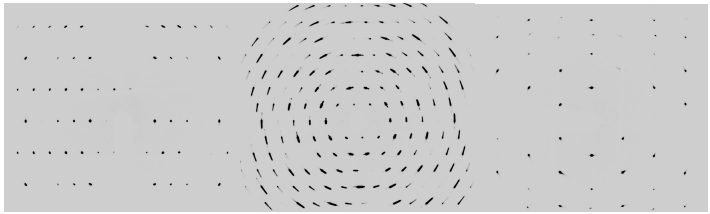
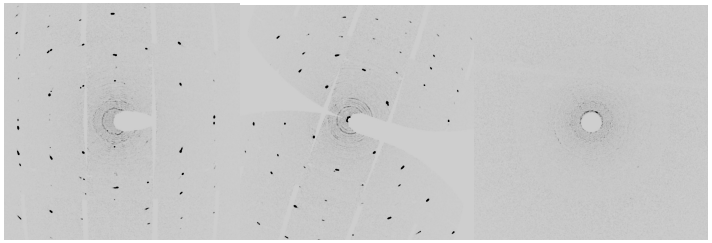
References

[1] D. Nečas and P. Klapetek, Open Physics **10**, 181 (2012).
[2] M.-C. Kao, L. P. Schewe, A. Akhtar, A. Vlad, T. F. Keller, K. Henkel, S. B. Anooz, A. Popp, Z. Galazka, J. I. Flege, A. Stierle, and V. Vonk, Applied Physics Letters **128**, 071601 (2026).
[3] J. Åhman, G. Svensson, and J. Albertsson, Crystal Structure Communications **52**, 1336 (1996).
[4] E. Vlieg, "A concise rod manual," (2001).

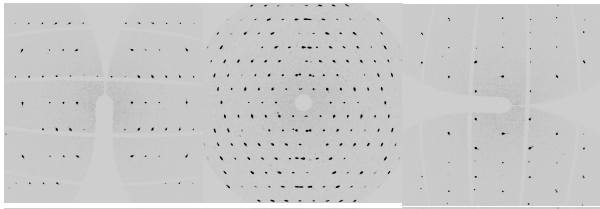
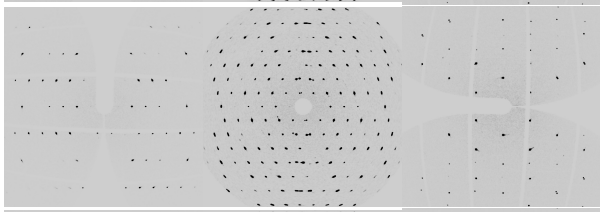
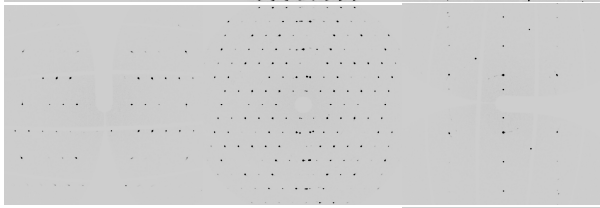
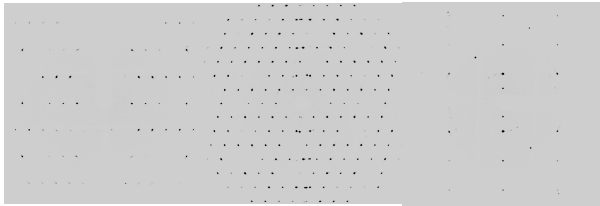
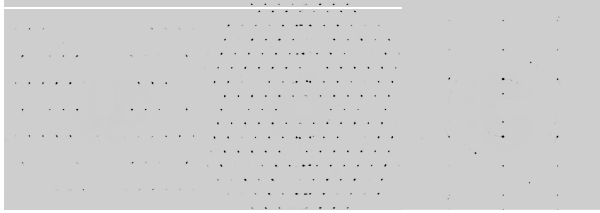
A.3 Single-Crystal X-ray Diffraction Data (P24)

#S	name	Detdist	deg	Scan info	data reduction		Unit cell	HK0	H0L	0KL
					Ga0_0p_SC_03					
#2	Ga0_0p_SC_03_120_s2	120	0	pflyscan kphi 0 360 360 2; atten 0	UB fit with 4284 obs out of 8113 (total:8113,skipped:0)	(52.80%)	12.176(2) 3.0288(5) 5.7860(11) 89.921(15) 103.642(16) 89.984(15) 207.36(7)			
#3	Ga0_0p_SC_03_120_s3	120	0	pflyscan kphi 0 360 360 2; atten 10	UB fit with 2941 obs out of 3465 (total:3465,skipped:0)	(84.88%)	12.209(2) 3.0361(3) 5.7998(10) 89.992(10) 103.768(15) 89.990(10) 208.81(5)			
#4	Ga0_0p_SC_03_120_s4	120	0	pflyscan kphi 0 360 360 2; atten 20	UB fit with 2772 obs out of 5170 (total:5170,skipped:0)	(53.62%)	12.171(3) 3.0270(7) 5.7969(15) 89.92(2) 103.67(2) 90.17(2) 207.52(9)			
#5	Ga0_0p_SC_03_120_s5	250	0	pflyscan kphi 0 360 360 2; atten 0	UB fit with 1230 obs out of 1414 (total:1414,skipped:0)	(86.99%)	12.210(6) 3.0315(8) 5.799(3) 89.94(3) 103.71(4) 90.14(3) 208.52(14)			
#6	Ga0_0p_SC_03_120_s6	250	0	pflyscan kphi 0 360 360 2; atten 10	UB fit with 28 obs out of 29 (total:29,skipped:0)	(96.55%)	12.24(3) 3.037(7) 5.798(16) 89.9(2) 104.0(2) 89.8(2) 209.1(9)			
					GaO_0p_SC_03			HK0	H0L	0KL
#1	Ga0_0p_SC_03_500_s1	500	0	pflyscan kphi 0 360 360 5; atten 0	UB fit with 161 obs out of 162 (total:162,skipped:0)	(99.38%)	12.24(2) 3.035(3) 5.806(10) 89.86(10) 103.77(14) 90.11(10) 209.6(5)			

#3	Ga0_0p_SC_03_115_s3	115	0	pflyscan kphi 0 360 1800 0.4; atten 4	UB fit with 4883 obs out of 5314 (total:5314,skipped:0)	(91.89%)	12.1943(14) 3.0324(3) 5.7933(7) 90.000(8) 103.739(10) 89.988(8) 208.09(4)	
#4	Ga0_0p_SC_03_115_s4	115	0	pflyscan kphi 0 360 1800 0.4; atten 0	UB fit with 5855 obs out of 7121 (total:7121,skipped:0)	(82.22%)	12.1751(16) 3.0279(3) 5.7854(7) 90.024(10) 103.685(11) 89.964(10) 207.23(4)	

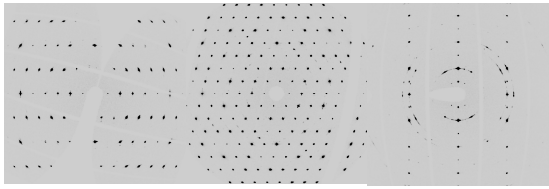
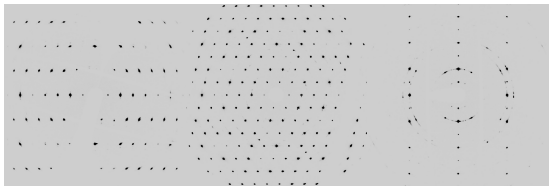
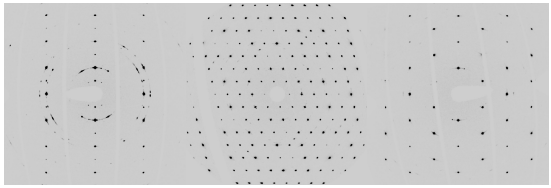
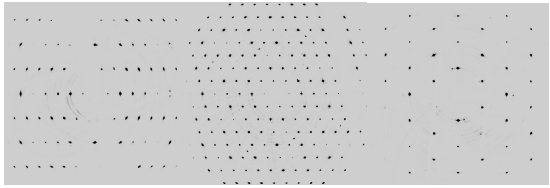
#S	name	Detdist	deg	Scan info	data reduction	Ga0_5p_SC_02	Unit cell	HK0	H0L	0KL
#2	Ga0_5p_SC_02_115_s2	115	0	pflyscan kphi 0 360 1800 0.4; atten 0	UB fit with 19 obs out of 35 (total:35,skipped:0)	(54.29%)	4.91(4) 12.00(3) 4.87(3) 89.4(4) 107.1(7) 90.2(4) 274(3)			
#3	Ga0_5p_SC_02_115_s3	115	0	pflyscan kphi 0 360 1800 0.4; atten 4	UB fit with 2698 obs out of 5370 (total:5370,skipped:0)	(50.24%)	12.140(2) 3.0211(3) 5.7784(13) 90.034(13) 103.818(17) 89.962(11) 205.79(6)			
#4	Ga0_5p_SC_02_115_s4	115	0	pflyscan kphi 0 360 1800 2; atten 4	UB fit with 4262 obs out of 10452 (total:10452,skipped:0)	(40.78%)	12.1454(18) 3.0210(3) 5.7773(11) 90.048(11) 103.806(14) 89.957(10) 205.85(5)			
#5	Ga0_5p_SC_02_115_s5	115	0	pflyscan kphi 0 360 1800 5; atten 4	UB fit with 4605 obs out of 10819 (total:10819,skipped:0)	(42.56%)	12.1450(17) 3.0211(4) 5.7745(10) 90.027(12) 103.782(14) 89.994(11) 205.78(5)			
#6	Ga0_5p_SC_02_115_s6	115	15	pflyscan kphi 0 360 1800 0.4; atten 0	UB fit with 363 obs out of 6531 (total:6531,skipped:0)	(5.56%)	12.210(6) 3.031(4) 5.691(7) 92.97(11) 104.92(9) 88.39(11) 203.2(4)			

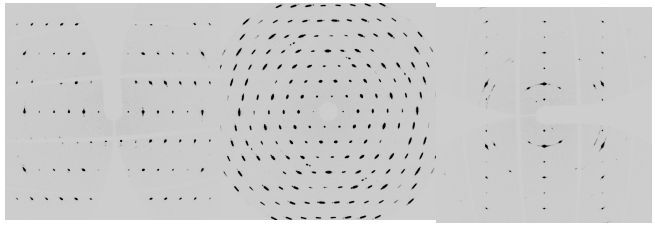
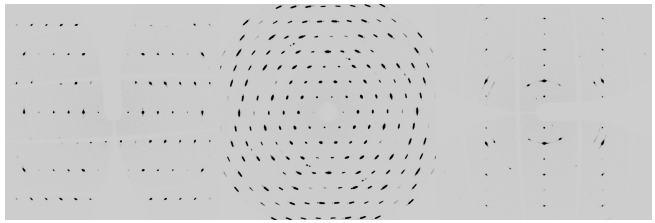
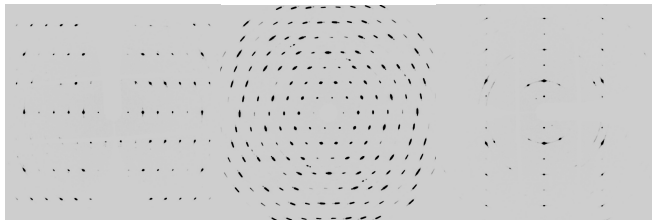
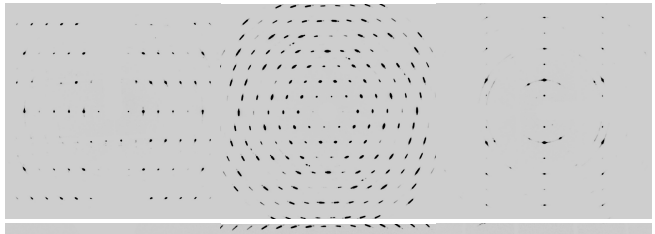
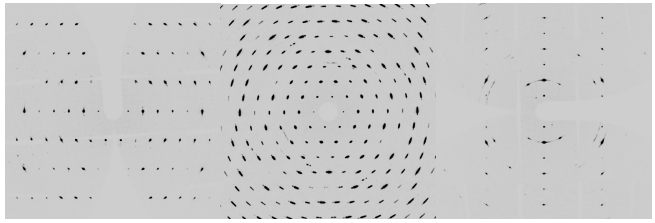
#7	Ga0_5p_SC_02_115_s7	115	**15**	pflyscan kphi 0 360 1800 0.4; atten 4	UB fit with 2554 obs out of 4679 (total:4679,skipped:0)	(54.58%)	12.1815(18) 3.0289(3) 5.7945(11) 89.986(11) 103.731(14) 90.021(10) 207.69(5)
#8	Ga0_5p_SC_02_115_s8	115	**15**	pflyscan kphi 0 360 1800 2; atten 4	UB fit with 925 obs out of 1240 (total:1240,skipped:0)	(74.60%)	12.250(3) 3.0427(5) 5.8164(18) 90.05(2) 103.71(2) 89.949(17) 210.61(9)
#9	Ga0_5p_SC_02_115_s9	115	**15**	pflyscan kphi 0 360 1800 5; atten 4	UB fit with 1843 obs out of 2793 (total:2793,skipped:0)	(65.99%)	12.218(2) 3.0370(4) 5.8118(12) 89.991(14) 103.734(17) 90.017(13) 209.48(6)

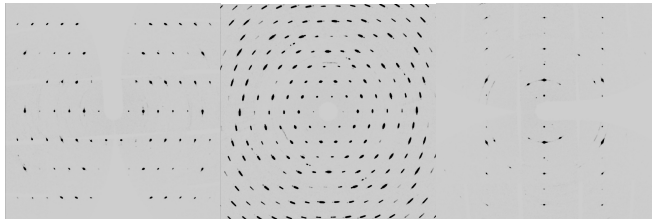
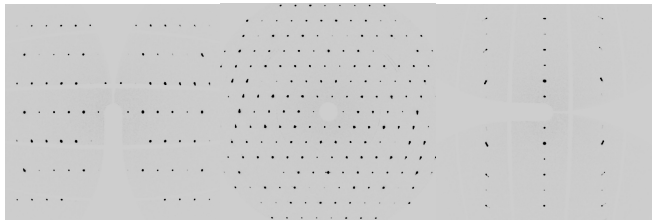
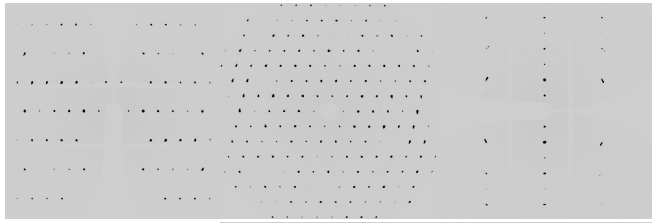
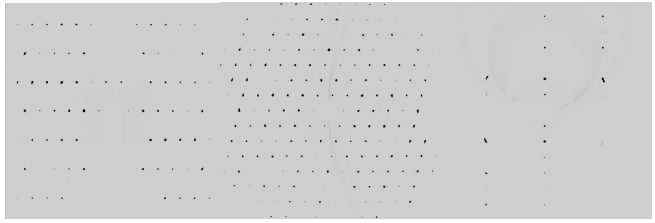
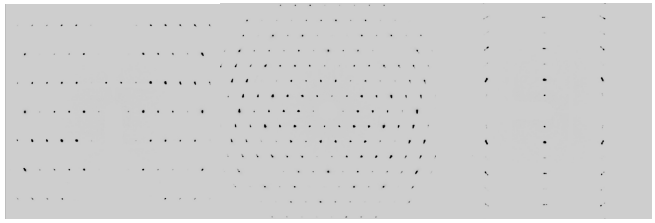
#S	name	Detdist	deg	Scan info	data reduction		Unit cell	HK0	H0L	0KL
					Ga0_10p_SC_04					
#3	GaO_10p_SC_04_115_s3	115	0	pflyscan kphi 0 360 360 1; atten 4	UB fit with 19 obs out of 35 (total:35,skipped:0)	(54.29%)	4.91(4) 12.00(3) 4.87(3) 89.4(4) 107.1(7) 90.2(4) 274(3)			
#4	GaO_10p_SC_04_115_s4	115	0	pflyscan kphi 0 360 1800 0.4; atten 0	UB fit with 981 obs out of 1622 (total:1622,skipped:0)	(60.48%)	12.132(3) 3.0154(7) 5.7637(18) 90.11(2) 103.91(3) 89.85(2) 204.66(10)			
#5	GaO_10p_SC_04_115_s5	115	0	pflyscan kphi 0 360 1800 0.4; atten 4	UB fit with 544 obs out of 799 (total:799,skipped:0)	(68.09%)	12.168(5) 3.0222(9) 5.778(2) 90.00(3) 103.92(3) 89.82(3) 206.23(13)			
#6	GaO_10p_SC_04_115_s6	115	0	pflyscan kphi 0 360 1800 2; atten 4	UB fit with 1745 obs out of 2999 (total:2999,skipped:0)	(58.19%)	12.137(2) 3.0143(5) 5.7646(10) 90.011(14) 103.936(16) 90.002(14) 204.69(6)			
#7	GaO_10p_SC_04_115_s7	115	0	pflyscan kphi 0 360 1800 5; atten 4	UB fit with 2573 obs out of 5106 (total:5106,skipped:0)	(50.39%)	12.1379(19) 3.0139(6) 5.7645(10) 90.028(15) 103.926(14) 90.000(15) 204.68(6)			

#S	name	Detdist	deg	Scan info	data reduction		Unit cell	HK0	H0L	0KL
					Ga0_10p_SC_01					

#15	Ga0_10p_SC_01_115_s15	115	0	pflyscan kphi 0 360 1800 0.4; atten 4	UB fit with 2204 obs out of 5076 (total:5076,skipped:0)	(43.42%)	12.135(2) 3.0150(5) 5.7603(15) 90.034(16) 103.860(18) 90.051(13) 204.61(7)
#16	Ga0_10p_SC_01_115_s16	115	0	pflyscan kphi 0 360 1800 2; atten 4	UB fit with 3021 obs out of 7432 (total:7432,skipped:0)	(40.65%)	12.135(2) 3.0146(4) 5.7644(16) 90.017(16) 104.005(19) 90.006(12) 204.60(7)

#S	name	Detdist	deg	Scan info	data reduction		Unit cell	HK0	H0L	0KL
					Ga0_15p_SC_02					
#4	GaO_15p_SC_02_115_S4	115	0	pflyscan kphi 0 360 1800 0.4; atten 0	UB fit with 1825 obs out of 1875 (total:1875,skipped:0)	(97.33%)	12.1167(18) 3.0090(4) 5.7574(10) 90.001(12) 103.885(14) 90.005(11) 203.78(5)			
#5	GaO_15p_SC_02_115_S5	115	0	pflyscan kphi 0 360 1800 2; atten 4	UB fit with 5716 obs out of 9796 (total:9796,skipped:0)	(58.35%)	12.1107(15) 3.0081(5) 5.7535(8) 89.925(14) 103.963(12) 90.059(13) 203.41(5)			
#6	GaO_15p_SC_02_115_S6	115	0	pflyscan kphi 0 360 1800 0.4; atten 0	UB fit with 1774 obs out of 1819 (total:1819,skipped:0)	(97.53%)	12.136(2) 3.0160(4) 5.7735(9) 90.003(11) 103.622(14) 90.009(12) 205.38(5)			
#7	GaO_15p_SC_02_115_S7	115	0	pflyscan kphi 0 360 1800 2; atten 4	UB fit with 3360 obs out of 3933 (total:3933,skipped:0)	(85.43%)	12.1353(17) 3.0140(4) 5.7723(9) 90.026(11) 103.661(12) 89.957(11) 205.15(5)			

#S	name	Detdist	deg	Scan info	data reduction		Unit cell	HK0	H0L	0KL
					Ga0_20p_SC_01					
#26	GaO_20p_SC_01_115_S26	115	0	pflyscan kphi 0 360 1800 0.4; atten 0	UB fit with 4928 obs out of 8994 (total:8994,skipped:0)	(54.79%)	12.0995(13) 3.0006(6) 5.7580(11) 89.972(16) 104.047(13) 90.031(13) 202.80(6)			
#27	GaO_20p_SC_01_115_S27	115	0	pflyscan kphi 0 360 1800 0.4; atten 4	UB fit with 4004 obs out of 6504 (total:6504,skipped:0)	(61.56%)	12.0767(14) 2.9956(5) 5.7480(12) 90.024(16) 104.045(14) 89.975(12) 201.73(6)			
#28	GaO_20p_SC_01_115_S28	115	0	pflyscan kphi 0 360 1800 2; atten 4	UB fit with 6182 obs out of 15025 (total:15025,skipped:0)	(41.14%)	12.0780(12) 2.9953(6) 5.7484(11) 90.040(16) 104.023(12) 89.929(14) 201.76(6)			
#29	GaO_20p_SC_01_115_S29	115	0	pflyscan kphi 0 360 1800 5; atten 4	UB fit with 2871 obs out of 4381 (total:4381,skipped:0)	(65.53%)	12.0768(18) 2.9957(5) 5.7482(15) 89.908(17) 104.138(17) 89.981(13) 201.66(7)			
#30	GaO_20p_SC_01_115_S30	115	15	pflyscan kphi 0 360 1800 0.4; atten 0	UB fit with 5016 obs out of 8827 (total:8827,skipped:0)	(56.83%)	12.1011(11) 3.0016(5) 5.7568(9) 90.022(14) 104.025(11) 89.990(11) 202.87(5)			

#S	name	Detdist	deg	Scan info	data reduction		Unit cell	HK0	H0L	0KL
#31	GaO_20p_SC_01_115_S31	115	15	pflyscan kphi 0 360 1800 0.4; atten 4	UB fit with 3867 obs out of 6236 (total:6236,skipped:0)	(62.01%)	12.0764(12) 2.9960(5) 5.7458(10) 90.022(14) 104.032(12) 90.003(11) 201.68(5)			
					Ga0_20p_SC_04					
#1	GaO_20p_SC_04_115_S1	115	0	pflyscan kphi 0 360 1800 0.4; atten 0	UB fit with 3019 obs out of 3771 (total:3771,skipped:0)	(80.06%)	12.0786(19) 2.9977(7) 5.7439(10) 89.818(17) 104.059(14) 89.991(17) 201.74(7)			
#2	GaO_20p_SC_04_115_S2	115	0	pflyscan kphi 0 360 1800 0.4; atten 4	UB fit with 2372 obs out of 2830 (total:2830,skipped:0)	(83.82%)	12.077(2) 2.9971(8) 5.7455(11) 90.205(19) 104.086(16) 90.03(2) 201.72(7)			
#3	GaO_20p_SC_04_115_S3	115	0	pflyscan kphi 0 360 1800 2; atten 4	UB fit with 2189 obs out of 2995 (total:2995,skipped:0)	(73.09%)	12.078(2) 2.9977(9) 5.7520(12) 90.42(2) 104.254(18) 90.01(2) 201.85(8)			
#4	GaO_20p_SC_04_115_S4	115	0	pflyscan kphi 0 360 1800 5; atten 4	UB fit with 5970 obs out of 8494 (total:8494,skipped:0)	(70.28%)	12.0755(18) 2.9946(7) 5.7493(10) 89.928(18) 103.976(15) 89.996(18) 201.75(7)			

#5

GaO_20p_SC_04_115_S5

115

0

pflyscan kphi 0 360 1800 2; atten 2

UB fit with 5246 obs out of 7490 (total:7490,skipped:0)

(70.04%)

12.1167(16) 3.0066(7) 5.7637(9)
90.369(16) 104.132(13)
89.987(16) 203.61(6)

#6

GaO_20p_SC_04_115_S6

115

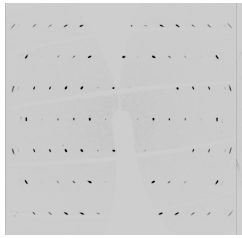
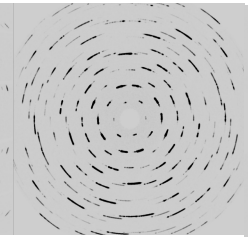
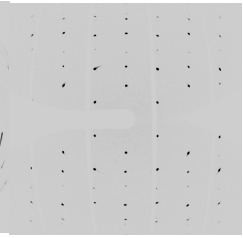
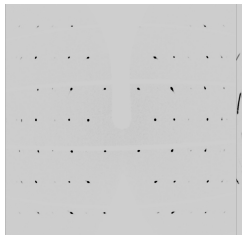
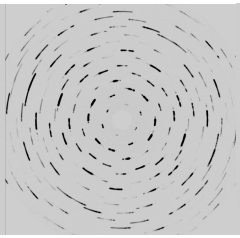
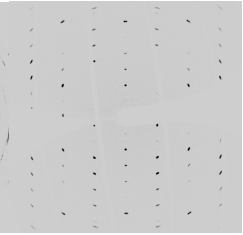
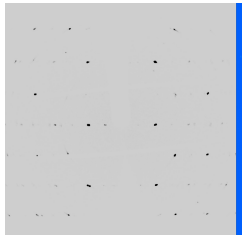
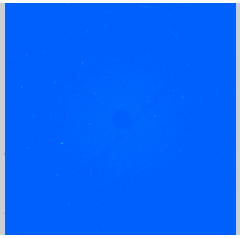
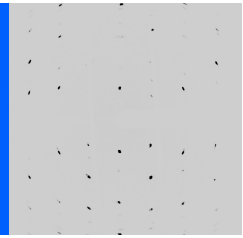
0

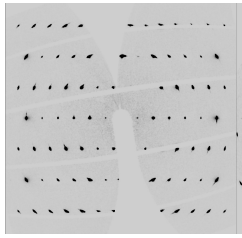
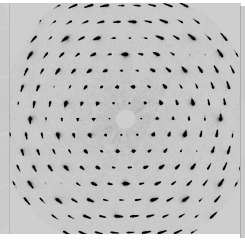
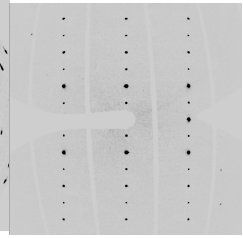
pflyscan kphi 0 360 1800 2; atten 6

UB fit with 4486 obs out of 6226 (total:6226,skipped:0)

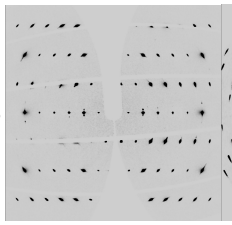
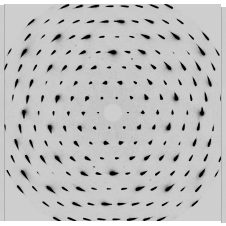
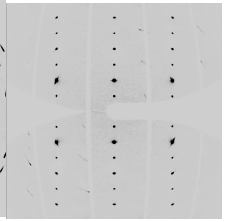
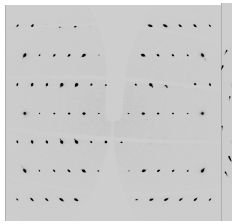
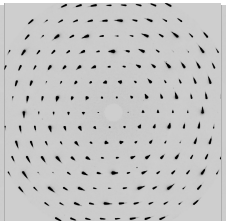
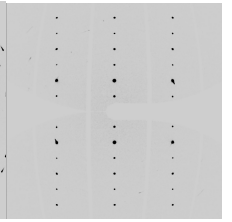
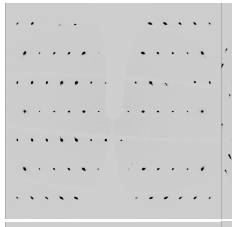
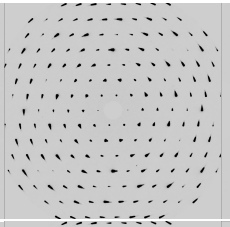
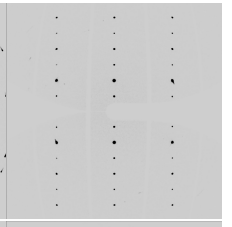
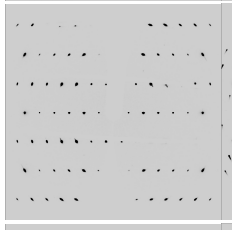
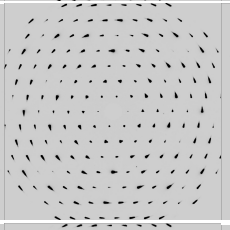
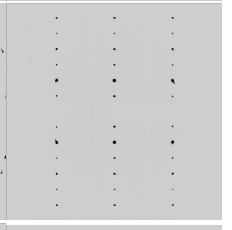
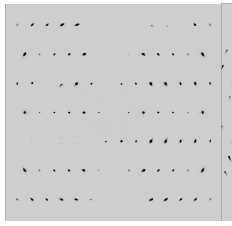
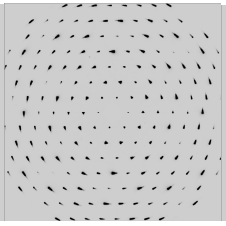
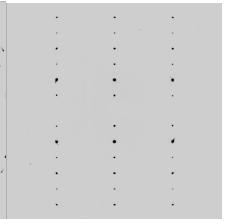
(72.05%)

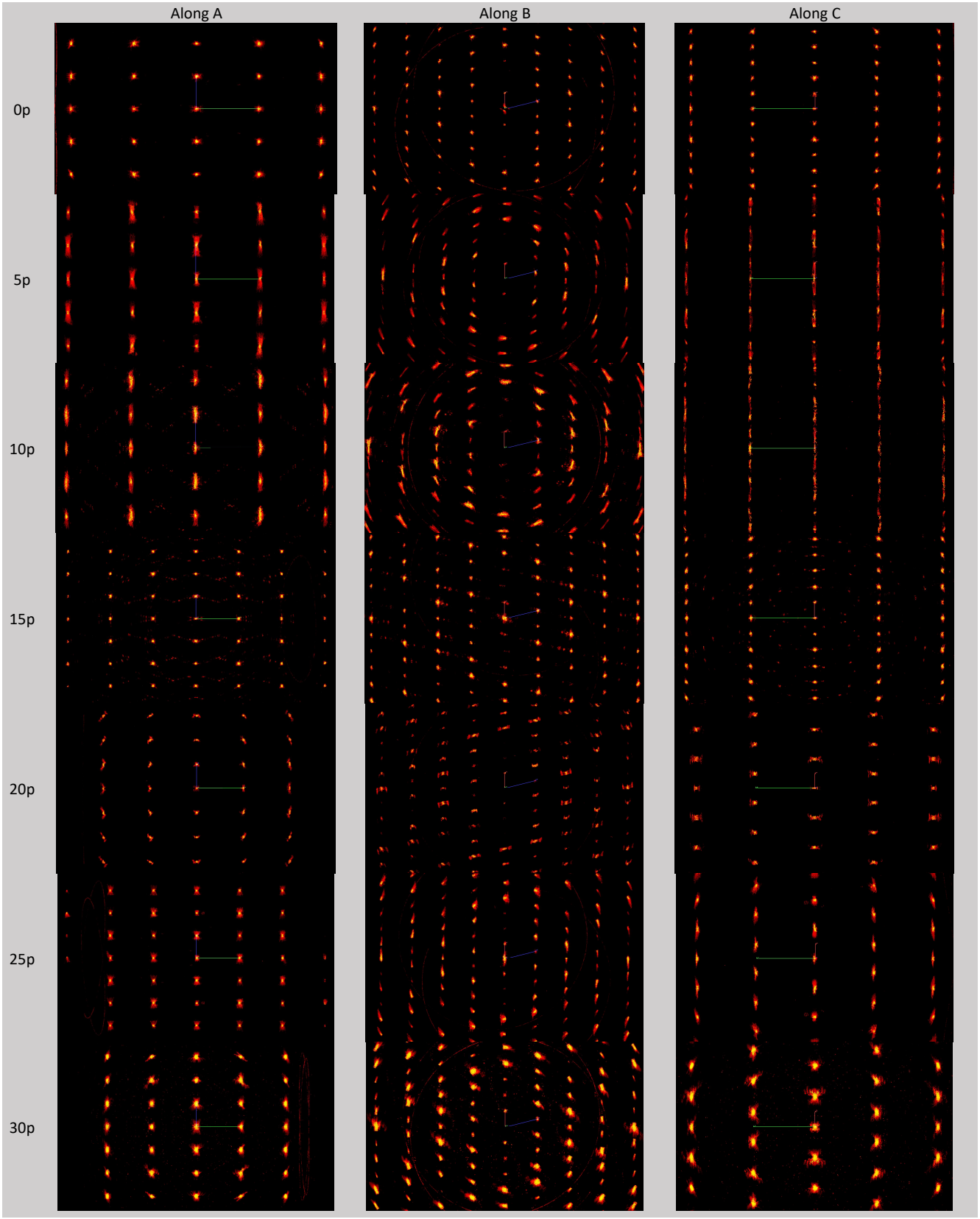
12.0804(18) 2.9972(7) 5.7468(9)
90.319(16) 104.133(13)
89.984(17) 201.78(6)

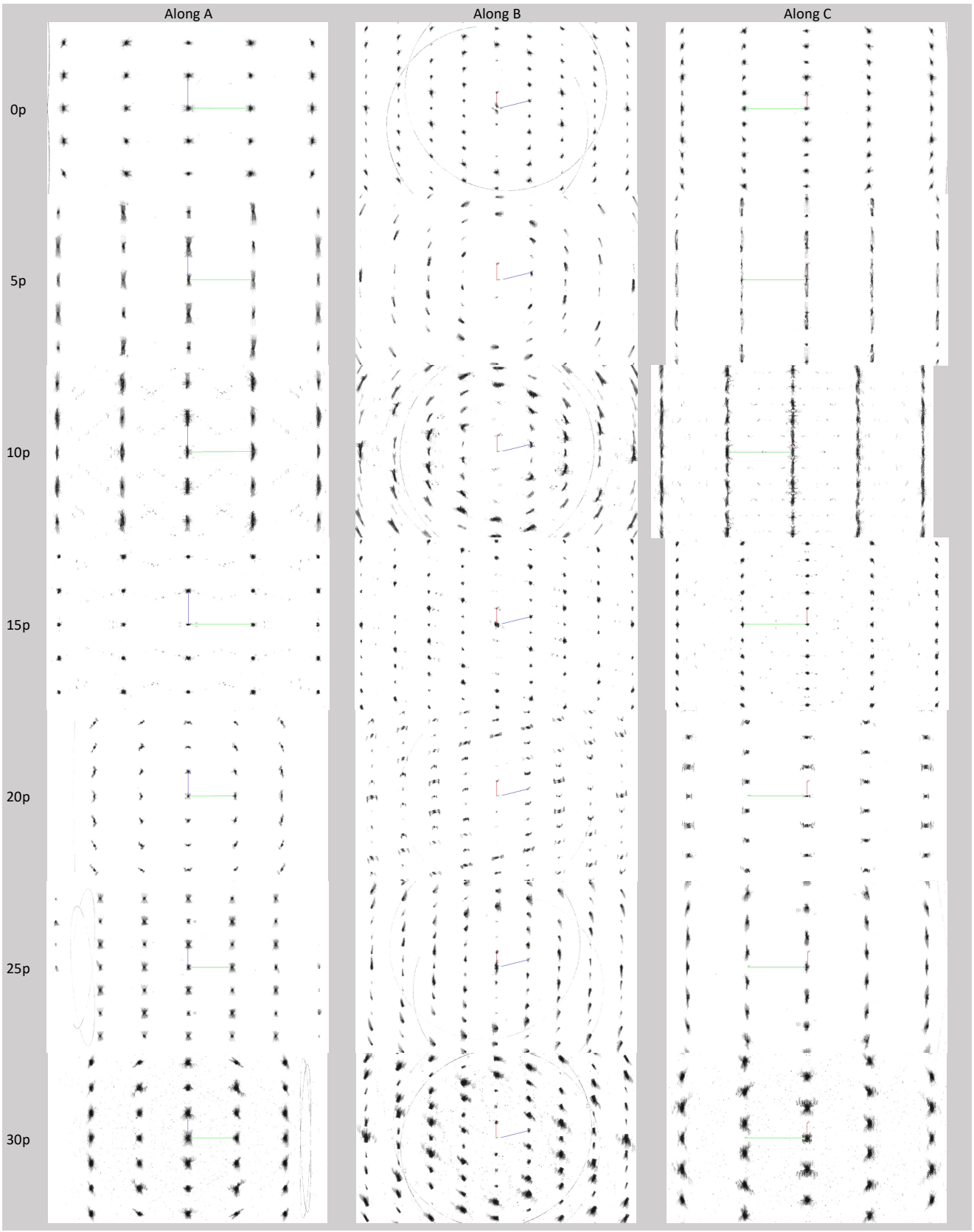
#S	name	Detdist	deg	Scan info	data reduction		Unit cell	HK0	H0L	0KL
						Ga0_25p_SC_01				
#3	GaO_25p_SC_01_115_S3	115	0	pflyscan kphi 0 360 1800 0.4; atten 0	UB fit with 41 obs out of 52 (total:52,skipped:0)	(78.85%)	12.03(4) 2.985(4) 5.72(2) 90.63(18) 104.0(3) 90.24(17) 199(1)			
#4	GaO_25p_SC_01_115_S4	115	0	pflyscan kphi 0 360 1800 0.4; atten 4	UB fit with 6 obs out of 7 (total:7,skipped:0)	(85.71%)	5.74(8) 2.989(13) 12.09(10) 89.6(6) 104.5(10) 89.4(9) 201(3)			
#5	GaO_25p_SC_01_115_S5	115	0	pflyscan kphi 0 360 1800 2; atten 4	UB fit with 20 obs out of 30 (total:30,skipped:0)	(66.67%)	2.77(4) 15.31(6) 3.29(2) 90.5(6) 104.5(9) 88.3(10) 135(2)			

#S	name	Detdist	deg	Scan info	data reduction		Unit cell	HK0	H0L	0KL
						Ga0_25p_SC_01				
#2	GaO_25p_SC_02_115_S2	115	0	pflyscan kphi 0 360 360 2; atten 0	UB fit with 2801 obs out of 5460 (total:5460,skipped:0)	(51.30%)	12.0497(18) 2.9887(4) 5.7343(15) 89.961(15) 104.052(17) 89.995(11) 200.33(6)			

#3	GaO_25p_SC_02_115_S3	115	0	pflyscan kphi 0 360 1800 0.4; atten 0	UB fit with 3090 obs out of 5406 (total:5406,skipped:0)	(57.16%)	12.0316(16) 2.9879(4) 5.7288(12) 89.974(13) 103.405(15) 90.005(10) 200.34(6)		
#4	GaO_25p_SC_02_115_S4	115	0	pflyscan kphi 0 360 1800 0.4; atten 4	UB fit with 2656 obs out of 4256 (total:4256,skipped:0)	(62.41%)	12.0496(17) 2.9892(4) 5.7345(13) 89.984(14) 104.105(16) 89.993(11) 200.32(6)		
#5	GaO_25p_SC_02_115_S5	115	0	pflyscan kphi 0 360 1800 2; atten 4	UB fit with 3692 obs out of 7118 (total:7118,skipped:0)	(51.87%)	12.0514(16) 2.9891(4) 5.7331(14) 90.038(15) 104.084(15) 89.970(11) 200.31(6)		
#6	GaO_25p_SC_02_115_S6	115	0	pflyscan kphi 0 360 1800 5; atten 4	UB fit with 4422 obs out of 8901 (total:8901,skipped:0)	(49.68%)	12.0553(16) 2.9922(4) 5.7432(13) 90.029(15) 103.439(15) 89.989(11) 201.50(6)		

#S	name	Detdist	deg	Scan info	data reduction		Unit cell	HK0	H0L	0KL
					Ga0_30p_SC_01					
#2	GaO_30p_SC_01_115_S2	115	0	pflyscan kphi 0 360 360 2; atten 4	UB fit with 3002 obs out of 6025 (total:6025,skipped:0)	(49.83%)	12.026(3) 2.9810(5) 5.7310(12) 90.043(15) 103.888(19) 89.986(15) 199.45(7)			
#5	GaO_30p_SC_01_115_S5	115	0	pflyscan kphi 0 360 1800 0.4; atten 0	UB fit with 4429 obs out of 6755 (total:6755,skipped:0)	(65.57%)	12.0287(15) 2.9821(3) 5.7303(9) 89.971(10) 104.116(13) 90.011(9) 199.34(4)			
#6	GaO_30p_SC_01_115_S6	115	0	pflyscan kphi 0 360 1800 0.4; atten 4	UB fit with 3915 obs out of 5363 (total:5363,skipped:0)	(73.00%)	12.0287(16) 2.9821(3) 5.7284(9) 89.982(10) 104.083(13) 90.007(9) 199.31(5)			
#7	GaO_30p_SC_01_115_S7	115	0	pflyscan kphi 0 360 1800 2; atten 4	UB fit with 5467 obs out of 9604 (total:9604,skipped:0)	(56.92%)	12.0269(16) 2.9805(3) 5.7328(10) 89.939(11) 104.042(13) 90.095(10) 199.36(5)			
#8	GaO_30p_SC_01_115_S8	115	0	pflyscan kphi 0 360 1800 5; atten 4	UB fit with 3604 obs out of 4999 (total:4999,skipped:0)	(72.09%)	12.033(2) 2.9818(4) 5.7279(11) 90.004(13) 103.976(16) 90.017(12) 199.43(6)			

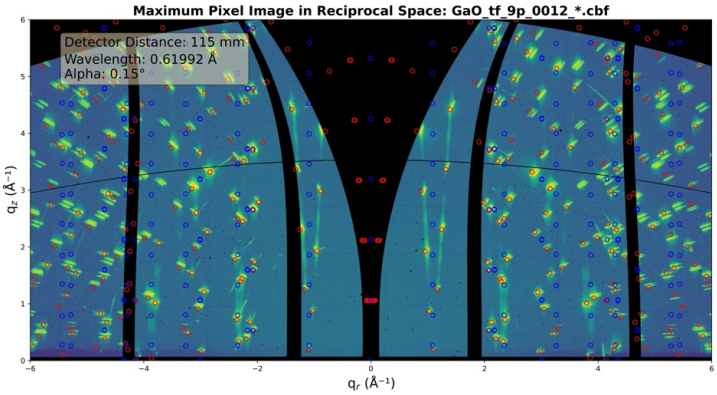
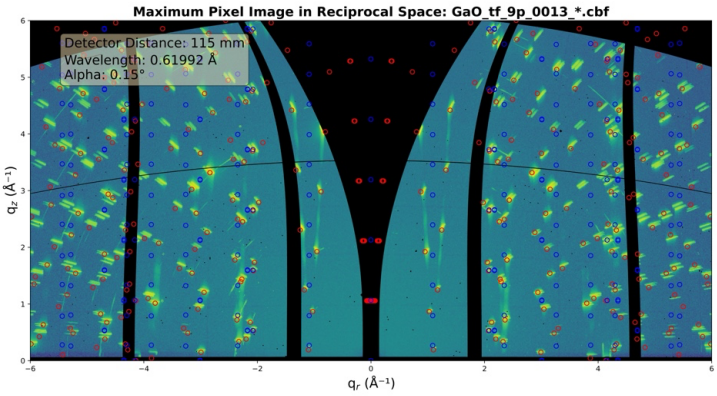
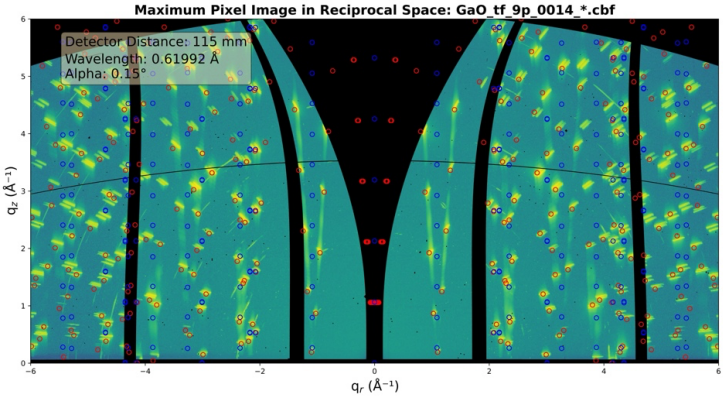

Along A
Along B
Along C
0p
5p
10p
15p
20p
25p
30p


Along A
Along B
Along C
0p
5p
10p
15p
20p
25p
30p

GiXRD_ 20keV (0. 61992 Å) 0.4428025

Sample 23 (23-018-AG 9% Al; 4 miscut GaO substrate)

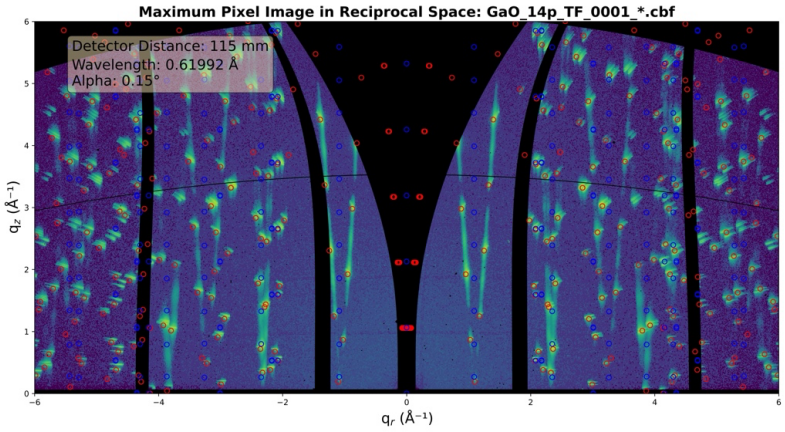
directory GaO_tf_9p

(detdist 115 0) S# 1 atten 8 flyscan kphi 0 360 720 2 Frame 0 -25 shutter still closed. Seems too many attenuators. Abort scan. S# 2 Atten 4 flyscan kphi 0 360 720 2 Scan crashed after 19 images….. #S 3 Atten 4 flyscan kphi 0 1 10 1 #S 4~7 Atten 0 flyscan kphi 0 1 10 1 #S 8 Atten 4 flyscan kphi 0 360 720 2 #S 9~11 Atten 4 flyscan kphi 0 1 10 1 #S 12 Atten 2; flyscan kphi 0 360 720 2 #S 13 Atten 2 flyscan kphi 0 360 720 2 #S 14 Atten 1 flyscan kphi 0 360 720 2 Red is simulated substrate peaks 0p Blue is simulated 9p peaks	 
(detdist 115 20) #S 15 Atten 1 flyscan kphi 0 5 10 2 (detdist 115 50) #S 16 Atten 1 flyscan kphi 0 5 10 2 #S 17 Atten 1 flyscan kphi 0 360 720 2 #S 18 Atten 1 flyscan kphi 16 17.99 6 2 #S 19 Atten: 1 ascan kth 35.0144 36.5144 100 1 (35.0144 to 36.5144) #S 20 Atten: 1 flyscan kth 35.0144 36.5144 100 2 #S 21 Atten 4 flyscan kth 35.0144 36.5144 100 2	
(detdist 500 20) #S 22 Atten 4 flyscan kphi 16 17.99 6 2 #S 23 Atten 4 flyscan kphi 16 17.99 6 2 #S 24 Atten 4 flyscan kphi 10 30 40 1 #S 25 Atten 2 flyscan kphi 0 360 360 1 #S 26 Atten 2 flyscan kphi 0 360 360 1 #S 27 Atten 2 flyscan kphi 217 223 60 1	#S 29 Atten 2 flyscan kphi 0 360 360 1 #S 30 Atten 1 flyscan kphi 0 360 360 1 #S 31 Atten 1 flyscan kphi 0 360 1800 2(detdist 500 0) #S 32 Atten 1 flyscan kphi 0 360 1800 2(detdist 500 17) #S 33 Atten 1 flyscan kphi 0 360 1800 2(detdist 500 34) #S 34 Atten 1 flyscan kphi 0 360 1800 2(detdist 500 51) #S 35 Atten 1 flyscan kphi 0 360 1800 2(detdist 500 68)

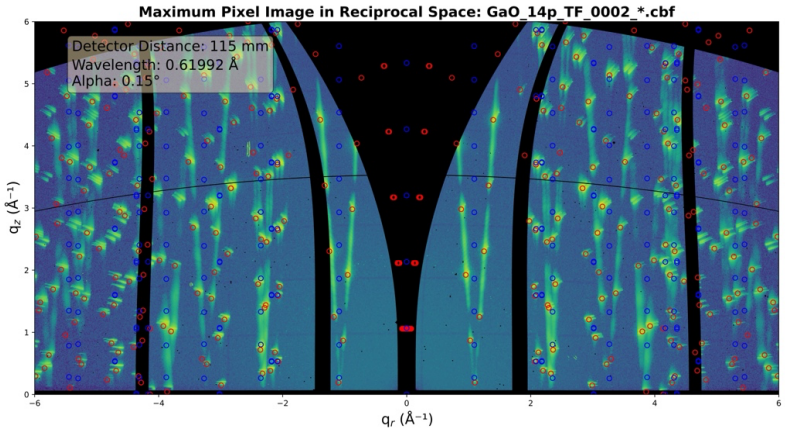
#S 28 Atten 2 flyscan kth 35.2644 36.5144 100 1	

Sample 24 (23-020-AG 14% Al; 4 miscut GaO substrate)

#S1 atten 4;pflyscan kphi 0 360 360 1(detdist 115 0)



#S2 atten 1;pflyscan kphi 0 360 360 1(detdist 115 0)



#3 atten 1: pflyscan kphi 0 360 1800 2 (detdist 500 0)

#4 atten 1: pflyscan kphi 0 360 1800 2 (detdist 500 17)

#5 atten 1: pflyscan kphi 0 360 1800 2 (detdist 500 34)

#6 atten 1: pflyscan kphi 0 360 1800 2 (detdist 500 51)

#7 atten 1: pflyscan kphi 0 360 1800 2 (detdist 500 68)

Red is simulated substrate peaks 0p

Blue is simulated 14p peaks

Sample 25 (23-016-AG 6% ; 4 miscut GaO substrate)

#S1 atten 1;pflyscan kphi 0 360 360 1 (detdist 115 0)

Forgot to adjust incident angle kth=35.26439---------

#3 atten 1: pflyscan kphi 0 360 1800 2 (detdist 500 0)

#4 atten 1: pflyscan kphi 0 360 1800 2 (detdist 500 17)

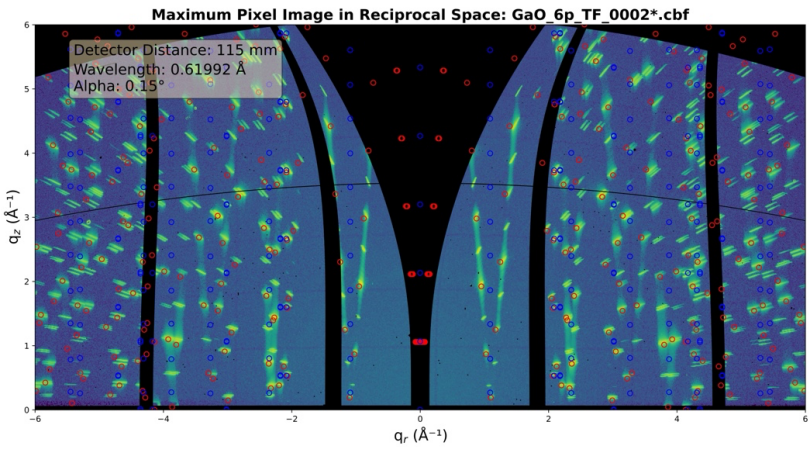
#5 atten 1: pflyscan kphi 0 360 1800 2 (detdist 500 34)

#6 atten 1: pflyscan kphi 0 360 1800 2 (detdist 500 51)

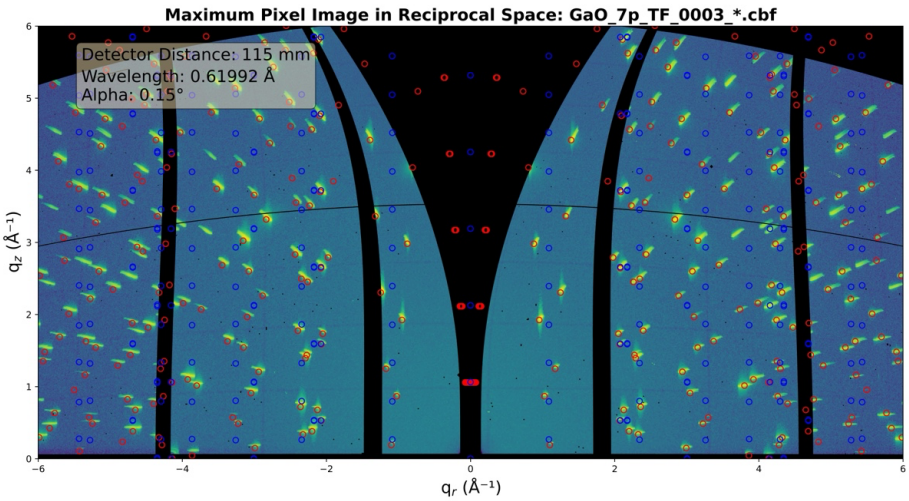
#7 atten 1: pflyscan kphi 0 360 1800 2 (detdist 500 68)

#S2 atten 1;pflyscan kphi 0 360 360 1(detdist 115 0)

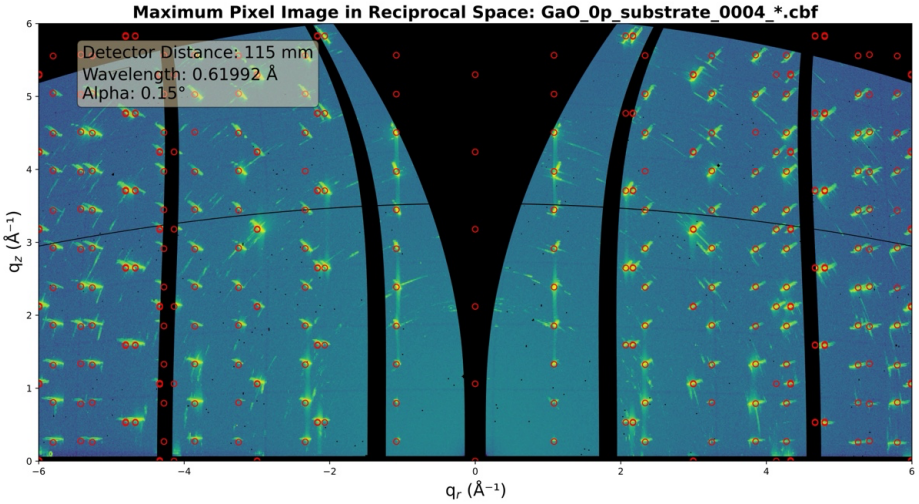
Red is simulated substrate peaks; Blue is simulated 6p peaks



Sample 26 (24-085-AG 7% Al ; 4 miscut GaO substrate)

#S 1 atten 1;pflyscan kphi 0 360 360 1 (bs off) #S 2 atten 1;pflyscan kphi 0 360 360 1 (check atten if its at 1; abort) #4 atten 1: pflyscan kphi 0 360 1800 2 (detdist 500 0) #5 atten 1: pflyscan kphi 0 360 1800 2 (detdist 500 17) #6 atten 1: pflyscan kphi 0 360 1800 2 (detdist 500 34) #7 atten 1: pflyscan kphi 0 360 1800 2 (detdist 500 51) #8 atten 1: pflyscan kphi 0 360 1800 2 (detdist 500 68)	#S 3 atten 1;pflyscan kphi 0 360 360 1  Red is simulated 7p peaks

Sample 27 (GaO_0p_substrate) pure GaO as-cleaved SC

(detdist 115 0) ; **#angle of incidence 0.16 deg** **(35.26439+0.15) umv kth 35.41439** #1 atten 1: pflyscan kphi 0 360 360 1 #2 atten 2: pflyscan kphi 0 20 20 1 (phiz -0.01) 500k #3 atten 3: pflyscan kphi 0 20 20 1 (phiz -0.01) 100k Alignment scan	#4 atten 1: pflyscan kphi 0 360 360 1 
	atten 1;#angle of incidence 0.16 deg (35.26439+0.15) ; umv kth 35.41439 #5 atten 1: pflyscan kphi 0 360 1800 2 (detdist 500 0) #6 atten 1: pflyscan kphi 0 360 1800 2 (detdist 500 17) #7 atten 1: pflyscan kphi 0 360 1800 2 (detdist 500 34) #8 atten 1: pflyscan kphi 0 360 1800 2 (detdist 500 51) #9 atten 1: pflyscan kphi 0 360 1800 2 (detdist 500 68)

Sample 28 (GaO_30p_substrate) as-cleaved SC

(detdist 115 0) ;

#angle of incidence 0.16 deg

(35.26439+0.15) umv kth 35.41439

#1 atten 1: pflyscan kphi 0 20 20 1

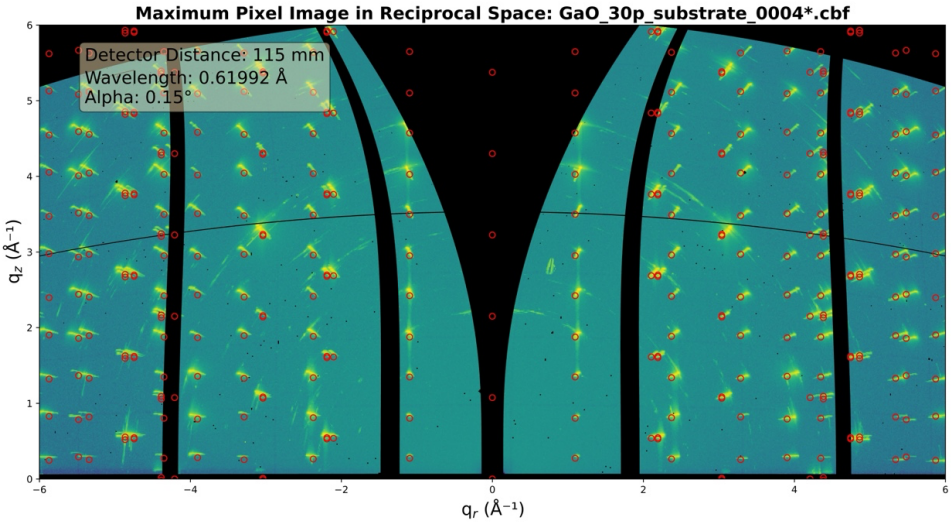
#2 atten 1: pflyscan kphi 0 20 20 1 (umvr phiz 0.01)

#3 atten 1: pflyscan kphi 0 20 20 1 (umvr phiz 0.01)

Alignment scan

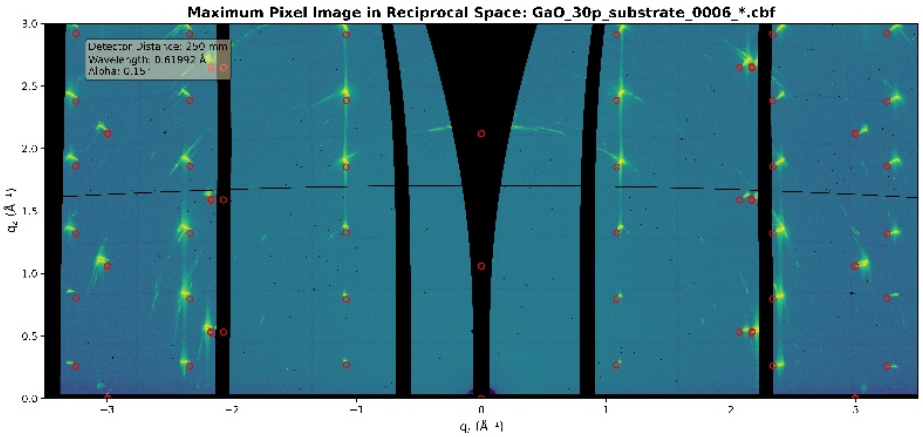
Red is simulated 30p peaks

#4 detdist 115 0; atten 1: pflyscan kphi 0 360 360 2

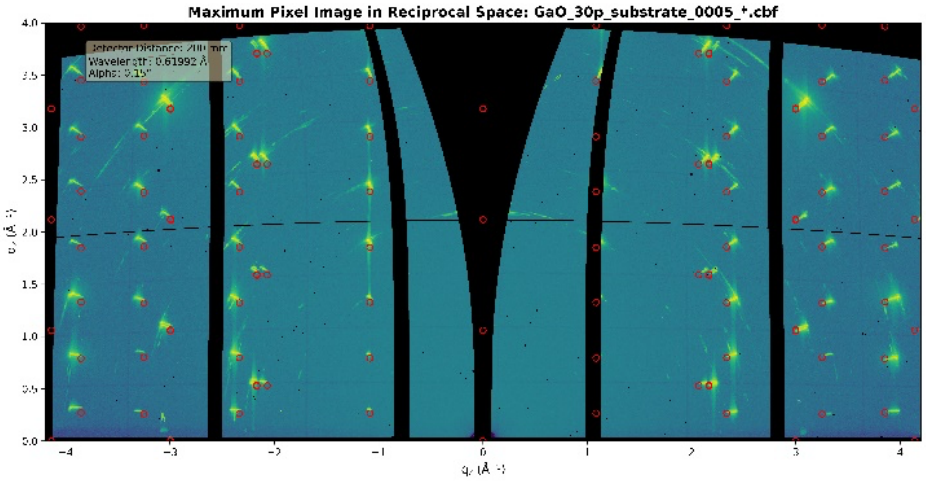


#7 **detdist 500 0**; atten 1: pflyscan kphi 0 360 360 2 ; Beam is shut off (machine day) abort

#6 **detdist 250 0**; atten 1: pflyscan kphi 0 360 360 2



#5 **detdist 200 0**; atten 1: pflyscan kphi 0 360 360 2



for CRYSALIS

x = 0.00: 12.2140 3.0370 5.7981 90 103.8300 90

x = 0.05: 12.1865 3.0285 5.7871 90 103.8575 90

x = 0.10: 12.1590 3.0200 5.7761 90 103.8850 90

x = 0.15: 12.1315 3.0115 5.7651 90 103.9125 90

x = 0.20: 12.1040 3.0030 5.7541 90 103.9400 90

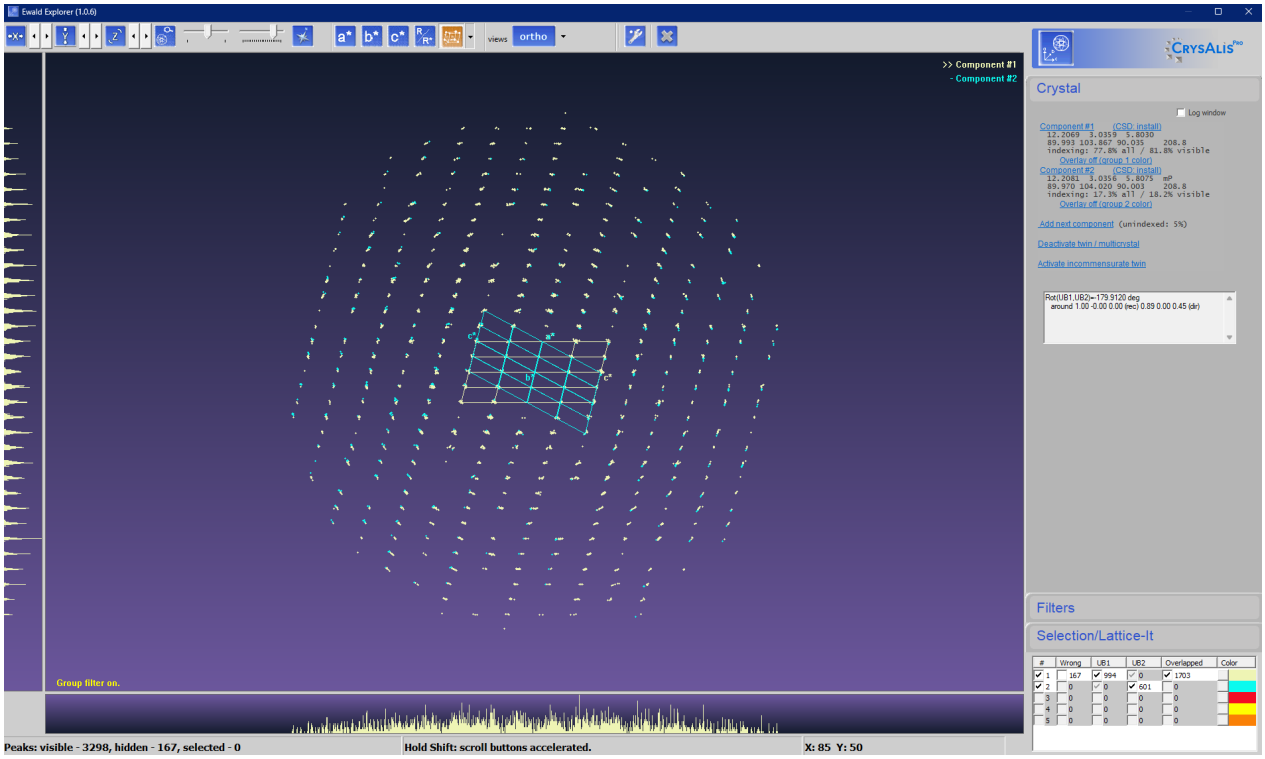
x = 0.25: 12.0765 2.9945 5.7431 90 103.9675 90

x = 0.30: 12.0490 2.9860 5.7321 90 103.9950 90

x = 0.35: 12.0215 2.9775 5.7211 90 104.0225 90

Rikagu Analysis

GaO_0p_S3



A.4 Crystallography Data

Bulk unit cell				B-termination					
Atom	x	y	z	x (surface normal)	y	z	DW (Å^2)	x-displacement (Å)	z-displacement (Å)
O1	1.000	0.5	0.564	0.9934 ± 0.0013	0.5	0.5490 ± 0.0028	0.522 ± 0.041	-0.0807	-0.0868
O2	0.990	0.5	0.109	0.9945 ± 0.0011	0.5	0.1138 ± 0.0025	0.522 ± 0.041	0.0561	0.0279
Ga1(oct)	0.985	0.0	0.314	0.9765 ± 0.0003	0.0	0.3163 ± 0.0009	1.066 ± 0.176	-0.1034	0.0132
Ga2(tet)	0.916	0.5	0.795	0.9196 ± 0.0003	0.5	0.7912 ± 0.0008	1.066 ± 0.176	0.0441	-0.0223
O3	0.831	0.0	0.744	0.8293 ± 0.0011	0.0	0.7330 ± 0.0025	0.42	-0.0208	-0.0640
O4	0.822	0.0	0.256	0.8252 ± 0.0012	0.0	0.2544 ± 0.0028	0.42	0.0387	-0.0095
Ga3(tet)	0.737	0.5	0.205	0.7332 ± 0.0003	0.5	0.1974 ± 0.0008	0.31	-0.0462	-0.0438
Ga4(oct)	0.668	0.0	0.686	0.6684 ± 0.0003	0.0	0.6818 ± 0.0007	0.31	0.0045	-0.0242
O5	0.663	0.5	0.891	0.6633 ± 0.0010	0.5	0.891	0.42	0.0038	
O6	0.653	0.5	0.436	0.6457 ± 0.0010	0.5	0.436	0.42	-0.0887	
O7	0.500	0.0	0.564	0.5042 ± 0.0010	0.0	0.564	0.42	0.0509	
O8	0.490	0.0	0.109	0.4863 ± 0.0009	0.0	0.109	0.42	-0.0455	
Ga5(oct)	0.485	0.5	0.314	0.485	0.5	0.314	0.31		
Ga6(tet)	0.416	0.0	0.795	0.416	0.0	0.795	0.31		
O9	0.331	0.5	0.744	0.331	0.5	0.744	0.42		
O10	0.322	0.5	0.256	0.322	0.5	0.256	0.42		
Ga7(tet)	0.237	0.0	0.205	0.237	0.0	0.205	0.31		
Ga8(oct)	0.168	0.5	0.686	0.168	0.5	0.686	0.31		
O11	0.163	0.0	0.891	0.163	0.0	0.891	0.42		
O12	0.153	0.0	0.436	0.153	0.0	0.436	0.42		

Table A.1: Fractional positions (x, y, z) and isotropic Debye-Waller parameters (DW) of the atoms in the bulk β-Ga_2O_3 unit cell and fitted positions of the atoms in the near-surface of the B-termination. The DW parameters (without error bar) are taken from literature. [43] All fractional co-ordinates are defined with respect to a monoclinic cell with: a = 12.214 Å, b = 3.037 Å, c = 5.798 Å, α = 90°, β = 103.83°, and γ = 90°. Please note that the x-direction is along the surface normal. The chi-square of the fit B is 3297.77, the normalised chi-square is 1.20, and the R-factor is 0.199.

Model	Ordered				Non-ordered				Refined			
Atom	x-dis. (Å)	z-dis. (Å)	DW (Å^2)	Occ. (%)	x-dis. (Å)	z-dis. (Å)	DW (Å^2)	Occ. (%)	x-dis. (Å)	z-dis. (Å)	DW (Å^2)	Occ. (%)
O1	−0.177(19)	−0.291(31)	0.000(32)	100.00	0.095(19)	−0.403(28)	0.010(25)	100.00	−0.037(20)	−0.228(29)	0.002(66)	100.00
O2	−0.806(23)	−0.834(45)	0.000(32)	100.00	−0.112(23)	0.163(42)	0.010(25)	100.00	0.166(24)	0.360(38)	0.002(66)	100.00
Ga1(oct)	−0.113(6)	0.091(9)	0.000(7)	80.78	−0.212(8)	−0.113(12)	1.193(14)	49.37	−0.186(7)	0.017(10)	1.200(16)	75.96
Al1(oct)			0.000(7)	19.22(148)			1.193(14)	50.63(174)			1.200(16)	24.04(164)
Ga2(tet)	−0.051(5)	−0.103(8)	0.000(7)	100.00	0.007(4)	0.149(7)	1.193(14)	99.93	0.012(5)	0.105(7)	1.200(16)	96.73
Al2(tet)	x	x	x	x	x		1.193(14)	0.07(234)			1.200(16)	3.27(165)
O3	−1.636(37)	−0.672(49)	0.42	100.00	0.862(21)	−0.418(35)	0.42	100.00	−1.764(55)	0.010(76)	0.42	100.00
O4	−0.183(23)	0.170(36)	0.42	100.00	−0.061(21)	0.151(37)	0.42	100.00	−1.028(19)	0.671(31)	0.42	100.00
Ga3(tet)	−0.140(5)	−0.210(8)	0.31	100.00	−0.143(5)	−0.143(7)	0.31	99.98	−0.094(5)	−0.188(8)	0.31	100.00
Al3(tet)	x	x	x	x	x		0.31	0.02(106)			0.31	0.00(103)
Ga4(oct)	−0.079(7)	0.068(10)	0.31	89.35	−0.076(4)	−0.100(6)	0.31	100.00	0.015(11)	−0.124(14)	0.31	99.97
Al4(oct)			0.31	10.65(156)			0.31	0.00(129)			0.31	0.03(122)
O5			0.42	100.00			0.42	100.00			0.42	100.00
O6			0.42	100.00			0.42	100.00			0.42	100.00

Table A.2: Structural parameters for β-$(Al_{0.2}Ga_{0.8})_2O_3$ derived from three distinct models: ordered, non-ordered, and PXRD-refined. Reported values include fitted displacements along the x (surface normal) and z axes, followed by Debye-Waller (DW) factors, and Ga/Al site occupancies. Fitted values are presented with associated error bars. The DW parameters (without error bar) are taken from literature. [43]

List of Figures

1.1 Application space of Si and wide-bandgap semiconductors. (a) Summary of voltage and current ratings reported for Si, SiC, GaN, and Ga_2O_3 power devices from Pearton et al. [13] (b) Power–frequency operating regimes as described by Mastro et al. [3] Figure adapted from [1, 3, 13]. 4

2.1 A schematic representation of the Ewald sphere construction in two dimensions. The reciprocal lattice points are indicated by black dots. The incident wavevector ($\mathbf{k}_i$) and the scattered wavevector ($\mathbf{k}_f$) originate from the center of the Ewald sphere (solid blue circle). The scattering vector ($\mathbf{G}$) connects the origin to the reciprocal lattice point, satisfying the Laue condition for diffraction ($\mathbf{k}_f - \mathbf{k}_i = \mathbf{G}$). 12

2.2 Bragg diffraction geometry. Constructive interference occurs when the path difference between rays reflected from adjacent lattice planes equals an integer multiple of the wavelength, $2d_{hkl} \sin\theta = n\lambda$. The angle between the incident and diffracted beams is 2θ. 13

2.3 Calculated 1D structure factor amplitude $|F|$ demonstrating finite size effects for $N = 4$ (black), $N = 8$ (blue), and $N = 60$ (red) unit cells. As N increases, the intermediate Laue oscillation fringes are suppressed, and the main Bragg peaks rapidly converge toward sharp δ-functions. 14

2.4 (a) In an infinite three-dimensional crystal, periodicity in the h, k and l directions gives rise to constructive interference in reciprocal space, producing diffraction at the Bragg peaks. (b) At the crystal surface, periodicity is interrupted, leading to incomplete interference along l. As a result, the scattered intensity along the CTRs remains non-zero and exhibits maxima at the Bragg peaks. 15

2.5 Calculated CTR intensity profile as a function of out-of-plane momentum transfer, l, showing the effect of surface relaxation. For an ideally terminated crystal with no surface relaxation ($z = 0$), the intensity decreases smoothly between the Bragg peaks ($l = 0, 1, 2, \dots$). In contrast, surface expansion ($z > 0$) or contraction ($z < 0$) produces characteristic intensity differences which become more pronounced at higher momentum transfer. 16

2.6 Snell's law and the Fresnel equations relate the incident wavevector k_I impinging on a sample surface at a grazing angle α to the reflected and refracted waves, occurring at angles α and α', splitting into a reflected wave at α and a refracted wave transmitted at α', respectively. Adapted from [20, 23]. 19

2.7 Schematic diagram of a multilayer transmission and reflection model consisting of $j + 1$ layers and N interfaces. Redrawn from [23]. 20

2.8 Energy-dependent experimental mean free path lengths of electrons in various materials. A universal minimum occurs at electron kinetic energies of around 100 eV, where the mean free path is typically below 1 nm. The dashed curves represent theoretical models from the original study: (i) represents Penn's theoretical relation using mean parameter values, [30] and (ii) represents the least squares fit to the experimental data for energies above 150 eV. Adapted from [29]. 23

2.9 Overview of a LEED setup in real space and its corresponding Ewald sphere representation in reciprocal space, showing the crystal truncation rods indexed by (h, k). Adapted from [31]. 24

2.10 LEED patterns of (a) an as-cleaved β-Ga_2O_3(100) single crystal surface ($E = 98.4$ eV), and as-cleaved $(Al_xGa_{1-x})_2O_3$(100) single crystal surface with (b) $x = 0.1$ ($E = 98.3$ eV), (c) $x = 0.2$ ($E = 98.4$ eV), and (d) $x = 0.3$ ($E = 149$ eV). All patterns were acquired after oxygen annealing. With increasing Al content, the diffraction features become increasingly blurred, most likely due to charging effects. 25

2.11 Atomic Force Microscopy (AFM). (a) Photograph of the AFM instrument (Bruker Dimension Icon) located at the DESY NanoLab. (b) Schematic illustrations of AFM operation in contact mode and tapping mode. (c) AFM image of an as-cleaved β-Ga_2O_3 single-crystal surface. The schematic illustrations have been adapted and modified from [32]. 26

2.12 The MBE II chamber at the DESY NanoLab is used for surface characterization using LEED. [33] 28

2.13 (a) Reflectometer, (b) PSIC diffractometer, and (c) SIXC diffractometer available at the X-ray laboratory of DESY NanoLab. [33] 29

2.14 UHV hutch endstation at the SIXS beamline at the SOLEIL synchrotron. The UHV system is integrated into the large diffractometer, with the preparation chamber on the right side and the main chamber with the beryllium window for in-situ scattering measurements on the left. The X-ray beam enters from the direction indicated by the yellow dot. 30

2.15 EH1 endstation at the P24 Chemical Crystallography beamline of PETRA III (DESY), equipped with a high-precision Huber four-circle kappa diffractometer and a Pilatus 1M CdTe detector for data collection. Bottom right: a β-Ga_2O_3 single crystal prepared to a size of approximately 40 x 40 μm, mounted on a Kapton-based sample loop using Paratone oil for single-crystal X-ray diffraction measurements. 31

2.16 Schematic of the GIXRD geometry. μ denotes the grazing incidence angle of the incoming beam with respect to the sample surface (the xz plane), while δ and γ the detector in-plane and out-of-plane angles with respect to the surface normal (z axis). 32

2.17 Peak integration and background subtraction using BINoculars. A two-dimensional reciprocal-space cross-section shows the defined ROI used for data extraction along the rod (K,L) = (2,2). 33

2.18 CTR Profile. The final output from BINoculars plotting the extracted structure factor as a function of the reciprocal lattice index (H). The sharp, high-intensity spikes correspond to bulk Bragg peaks, while the continuous curves connecting them represent the surface-sensitive truncation rod signals. Every data point reflects an individual integration step along the rod. 34

3.1 Atomic unit cells corresponding to the five known polymorphs of Ga_2O_3, with $\alpha, \beta, \gamma, \delta$ and ϵ occurring as metastable phases and β representing the thermodynamically stable form. 40

3.2 Phase transformation relationships and pathways among gallium oxide (Ga_2O_3) polymorphs and its hydrated precursors. The chart illustrates the specific thermal and environmental conditions driving the transitions from metastable phases ($\alpha, \gamma, \delta, \epsilon$) toward the thermodynamically stable β phase. For $Ga_{2-x}Al_xO_3$ solid solutions, wet conversion to β-Ga_2O_3 occurs only when x < 1.3. When x > 1.3, the material forms a β-Al_2O_3 type structure instead of converting to β-Ga_2O_3. Adopted from [41]. 41

3.3 Conventional unit cell of β-Ga_2O_3(100). (a) and (b) show side views along the [100]/[001] and [100]/[010] directions, respectively, while (c) shows the top view along the [010]/[001] plane. Gallium atoms are shown in green and oxygen atoms in red. 42

3.4 Bandgap energy (E_g) of $(Al_xGa_{1-x})_2O_3$ alloys as a function of the Al composition (x). Direct bandgaps are indicated by solid symbols and indirect bandgaps by open symbols for the monoclinic and corundum structures. Solid and dashed lines represent quadratic fits to the indirect and direct bandgaps, respectively. Computed values are shown in color, while experimental values are shown in black. [7, 15, 46–49] This figure is adopted from [7]. 43

3.5 Crystallographic models of pure β-Ga_2O_3, θ-Al_2O_3, and three representative 20% Al-alloyed β-Ga_2O_3 structures. (a) Pure β-Ga_2O_3. (b) θ-Al_2O_3. (c) Ordered model with Al occupying only the octahedral sites. (d) Non-ordered alloy model with Al distributed over both octahedral and tetrahedral sites. (e) PXRD-refined model with Ga and Al located at their refined fractional coordinates. Al atoms are shown in blue, Ga in green, and O in red. 44

3.6 Schematic illustration of a general-purpose growth furnace used for producing high-melting-point oxide crystals by the Czochralski method. This figure is adapted from Galazka et al. (2022). [45] 47

3.7 Phase diagram of the Ga_2O_3–Al_2O_3 system. The red points indicate experimentally measured melting temperatures of $(Al_xGa_{1-x})_2O_3$ during Czochralski growth. This figure is adapted from Galazka et al. (2023). [18] 48

3.8 (a) An image of the MOVPE system used for the growth of $(Al_xGa_{1-x})_2O_3$ thin films equipped at the Leibniz-Institut für Kristallzüchtung in Berlin. [62] (b) Schematic drawing of the MOVPE growth chamber used for the deposition of our thin-film samples, this figure is taken from [63]. 50

3.9 Diffraction image highlighting the pixel with the maximum intensity after a full 360° rotation, acquired at the P24 beamline using an X-ray energy of 20 keV. (a) β-Ga_2O_3 (100) single crystal substrate without miscut. (b) $(Al_xGa_{1-x})_2O_3$ with Al contents of 7% thin films grown on (100) β-Ga_2O_3 substrates with the miscut of 4°. (c) $(Al_xGa_{1-x})_2O_3$ with Al contents of 14% thin films grown on (100) β-Ga_2O_3 substrates with the miscut of 4°. The red circles indicate the simulated Bragg positions of the β-Ga_2O_3, and the blue circles indicate the Bragg positions of the $(Al_xGa_{1-x})_2O_3$. 51

3.10 Schematic of real and reciprocal space structures for a β-Ga_2O_3 substrate and MOVPE-grown AlGaO thin film, illustrating the influence of surface miscut and step-step correlation. For the thin film samples, the system is aligned with the thin-film surface. (a) An ideal, flat β-Ga_2O_3 substrate with no miscut, producing continuous CTRs perfectly aligned with the crystallographic surface normal. (b) A 4° miscut β-Ga_2O_3 substrate with an ideally thin film on top and a perfectly regular train of steps. A strong step-to-step correlation leads to CTR streaks oriented perpendicular to the crystallographic surface normal, with the Bragg peak signals aligned perpendicular to the stepped surface. (c) A 4° miscut β-Ga_2O_3 substrate with a thicker film (step bunching) on top and weak step–step correlation. The weak correlation causes the CTR signal oriented perpendicular to the crystallographic surface normal, but tilted by 4°. [67] Blue represents the signal contribution from the substrate, and orange represents the contribution from the thin film. 52

3.11 (a) All possible surface terminations of the as-cleaved β-Ga_2O_3 (100) surface. Terminations B, E, A, F, and G are symmetry-equivalent to terminations H, I, J, C, and D. (b) Experimental measured data (symbols) and simulated structure factors (solid line) for the different (100) surface terminations. The curves for terminations D & E, F & J, and G & I are fully overlap to each other because the two terminations are symmetry-equivalent and therefore produce identical structure factors. 55

3.12 Schematic of the twinned structure. (a) Real-space illustration of the twinned crystal, with the primary and twin domains shown in red and blue, respectively. (b) Simulated reciprocal space map demonstrating **twinning by (pseudo)merohedry**. A twinned crystal exhibits two superimposed sets of diffraction spots (red and blue), where an untwinned single domain shows only one set. The reciprocal space axes H and L are used consistently throughout this thesis to label all diffraction data, including CTRs. The indicated real-space crystal direction labeled as *surf.* corresponds to the c-axis, [001], of the unit cell. 57

3.13 Reconstructed $H0L$ reciprocal space plane of twinned β-Ga_2O_3 (100) single crystal. The experimental X-ray diffraction data (black spots) are overlapped with simulated reflections corresponding to the primary domain (red) and the twin domain (blue). 58

3.14 Reconstructed $H0L$ reciprocal space plane of untwinned 20% Al-doped β-Ga_2O_3 (100) single crystal. The experimental X-ray diffraction data (black spots) are overlapped with simulated reflections corresponding to the primary domain (red) and the expected twin domain (blue). The absence of experimental diffraction spots at the blue twin positions confirms the untwinned nature of the crystal. 60

4.1 Two possible surface terminations of β-Ga_2O_3(100) are indicated by red and blue dashed lines. The A-termination is a plane through the corner-sharing oxygen octahedra and tetrahedra. The B-termination is a plane through edge-sharing oxygen octahedra. The average broken bond length for B-termination is slightly higher than for the A-termination. The unit cell is shown in the (a) [100]/[001], (b) [100]/[010], and (c) [010]/[001] planes. (d) The fitted displacements of gallium atoms at the octahedral (Ga_{oct}) and tetrahedral (Ga_{tet}) sites, as well as the oxygen atoms, for the B-terminated surface are shown. The length of the displacement arrows are proportional to the magnitude of the displacement, but it is scaled up by a factor of approximately 100 to enhance visibility. 62

4.2 (a) AFM image of the as-cleaved β-Ga_2O_3(100) single crystal, showing the surface morphology and step structure. Four representative line profiles are indicated on the image. (b) Height profiles corresponding to the four indicated lines in (a), together with their fits. The profiles reveal a step height of approximately half the unit cell. 63

4.3 LEED patterns and in-plane reciprocal space maps of the β-Ga_2O_3(100) single crystal after annealing. (a) LEED pattern recorded at an electron energy of 98.4 eV. (b) Two-dimensional in-plane reciprocal space map, acquired at an X-ray energy of 18.42 keV. Both figures are indexed by (K, L). 64

4.4 Comparison of experimental, simulated, and fitted CTR data. The bulk structure factor (F) are shown as black circles with error bars. Simulated CTRs for terminations A and B are represented by blue and yellow lines. Fitted CTRs for termination B is indicated by red line. Each CTR is indexed by (K, L) and plotted as a function of H. 66

5.1 Cell parameters of $(Al_xGa_{1-x})_2O_3$ single crystals as a function of Al content (x = 0 to 0.3): (a) lattice parameters a, b, and c (in Å); (b) lattice angles α, β, and γ (in degrees). (c) unit cell volume (in $Å^3$). Experimental data measured in air are shown as symbols with error bars, while dashed lines show linear fits to the measured data. 71

5.2 X-ray reflectivity (XRR) profiles and fitted electron density (ρ_{el}) of $(Al_xGa_{1-x})_2O_3$ (100) bulk single crystals with varying aluminum content (x = 0 to 0.3). (a) Specular reflected intensity as a function of the reflection angle (open circles) and the fitted profile (solid line). Magnified view of the critical-angle region showing the shift of the 2θ (open circles) values toward lower angles for pure β-Ga_2O_3 (blue), $(Al_{0.1}Ga_{0.9})_2O_3$ (yellow), $(Al_{0.2}Ga_{0.8})_2O_3$ (green), and $(Al_{0.3}Ga_{0.7})_2O_3$ (black). The systematic shift with increasing Al content, as indicated by the red arrow, is consistent with the decrease in mass density. (b) Fitted average electron density (purple stars) as a function of Al content, obtained from XRR fits. The dashed purple line represents a linear fit to these fitted electron densities. . . . 73

5.3 Experimentally determined Al composition (x) of $(Al_xGa_{1-x})_2O_3$ (100) single crystals, derived from fitted electron densities and lattice parameters, as a function of the nominal Al composition. The experimentally determined Al compositions are shown as red points with error bars, and the dashed line indicates the ideal 1:1 relationship with x. 75

5.4 Crystallographic models of pure β-Ga_2O_3, θ-Al_2O_3, and two representative $(Al_xGa_{1-x})_2O_3$ structures with Al content of $x = 0.2$. (a) Pure β-Ga_2O_3. (b) θ-Al_2O_3. (c) Ordered model with Al occupying only the octahedral sites. (d) Non-ordered model with Al distributed over both octahedral and tetrahedral sites. Al atoms are shown in blue, Ga in green, and O in red. 75

5.5 Comparison of simulated and fitted CTR data for the $(Al_xGa_{1-x})_2O_3$ (100) single crystal with Al content of $x = 0.2$. The fitted and simulated structure factor (F) for the B-terminated surface of the Ordered$_{fit}$ (blue), Non-Ordered$_{fit}$ (red), and the pure Ga_2O_{3bulk} (yellow) model. The simulated structure factor (F) for the A-terminated surface of the Ordered$_{bulk}$A (light blue), Non-Ordered$_{bulk}$A (light red) model. Experimental structure factors are shown in black with corresponding error bars. Each rod is indexed by (K, L) and plotted as a function of the out-of-plane momentum transfer in reciprocal space, H. A and B refer to the two possible surface terminations of the (100) surface. 77

5.6 Visualization of the fitted atomic displacements (in Å) and the site occupancy (in %) results using the Ordered$_{fit}$ (left), Non-Ordered$_{fit}$ (right) model for a $(Al_xGa_{1-x})_2O_3$ (100) single crystal with the Al content of $x = 0.2$. The atomic displacements of the Ga/Al and O atoms were fitted along the [100] directions as Δx and [001] directions as Δz. The arrows indicate the displacement direction, and their lengths are proportional to the displacement magnitude, but are scaled up for clarity. 78

List of Tables

1.1 Comparison of fundamental material parameters relevant to power semiconductors performance, including BFOM values. Table adapted from Higashiwaki et al. [12] 3

2.1 Symmetry-equivalent CTRs grouped by in-plane momentum transfer families $\{K, L\}$ for the $C2/m$ plane group. The out-of-plane index is denoted by H. . . 35

5.1 Summary of linear fit results for the cell parameters and electron density as a function of nominal Al composition (x = 0 to 0.3). Fits were performed using the linear relation $y = m\,x + b$. 74

A.1 Fractional positions (x, y, z) and isotropic Debye-Waller parameters (DW) of the atoms in the bulk β-Ga_2O_3 unit cell and fitted positions of the atoms in the near-surface of the B-termination. The DW parameters (without error bar) are taken from literature. [43] All fractional co-ordinates are defined with respect to a monoclinic cell with: a = 12.214 Å, b = 3.037 Å, c = 5.798 Å, α = 90°, β = 103.83°, and γ = 90°. Please note that the x-direction is along the surface normal. The chi-square of the fit B is 3297.77, the normalised chi-square is 1.20, and the R-factor is 0.199. 125

A.2 Structural parameters for β-$(Al_{0.2}Ga_{0.8})_2O_3$ derived from three distinct models: ordered, non-ordered, and PXRD-refined. Reported values include fitted displacements along the x (surface normal) and z axes, followed by Debye-Waller (DW) factors, and Ga/Al site occupancies. Fitted values are presented with associated error bars. The DW parameters (without error bar) are taken from literature. [43] 126

List of Publications

1. Schober, J.-C., Beck, E. E., **Kao, M.-C.**, Kohantorabi, M., Creutzburg, M., Novikov, D. V., Keller, T. F., Holtermann, B., Firman, N., Caulfield, L., et al. (2024). *Atomically Smooth Fully Hydroxylated CeO_2 (001) Films on YSZ (001).* The Journal of Physical Chemistry C, 128(46), 19795–19806.
   URL: https://pubs.acs.org/doi/full/10.1021/acs.jpcc.4c04438.
2. S. Jatav, **M.-C. Kao**, M. Graf, E. H. Hill. Colloidal growth of titania in nanoporous gold toward electrochemical applications. Colloids Surf. A: Physicochem. Eng. Asp., 651. pp: 129700 (2022). ISSN: 0927-7757.
   URL: https://doi.org/10.1016/j.colsurfa.2022.129700.
3. Dolling, D.S., Blanco Garcia, M., Kohatorabi, M., Zhai, Y., Sochor, B., Haji Naghi Tehrani, M.E., Schober, J.C., **Kao, M.C.**, Dwivedi, J., Jeromin, A. and Gutowski, O., (2026). In-Situ Growth and Oxidation of Cu Nanoparticles on Rutile TiO_2 (110). The Journal of Physical Chemistry C.
   URL: https://pubs.acs.org/doi/full/10.1021/acs.jpcc.6c00835.
4. **Kao, M.C.**, Schewe, L.P., Akhtar, A., Vlad, A., Keller, T.F., Henkel, K., Anooz, S.B., Popp, A., Galazka, Z., Flege, J.I. and Stierle, A., (2026). Surface termination of β-Ga_2O_3 (100) as-cleaved single crystals. Applied Physics Letters, 128(7).
   URL: https://pubs.aip.org/aip/apl/article/128/7/071601/3380390.

Bibliography

[1] J. S. Speck and E. Farzana, *Ultrawide bandgap β-Ga_2O_3 semiconductor.* AIP Publishing, 2023, no. PUBDB-2026-00716.

[2] Z. Galazka, "β-Ga_2O_3 for wide-bandgap electronics and optoelectronics," *Semiconductor Science and Technology*, vol. 33, no. 11, p. 113001, 2018.

[3] M. A. Mastro, A. Kuramata, J. Calkins, J. Kim, F. Ren, and S. Pearton, "Perspective—opportunities and future directions for Ga_2O_3," *ECS Journal of Solid State Science and Technology*, vol. 6, no. 5, p. P356, 2017.

[4] H. H. Tippins, "Optical absorption and photoconductivity in the band edge of β-Ga_2O_3," *Physical Review*, vol. 140, no. 1A, p. A316, 1965.

[5] Z. Galazka, "β-Ga_2O_3 for wide-bandgap electronics and optoelectronics," *Semiconductor Science and Technology*, vol. 33, no. 11, p. 113001, 2018.

[6] E. Farzana and J. Speck, "Ultrawide bandgap β-Ga_2O_3 semiconductor: Theory and applications," 2023.

[7] H. Peelaers, J. B. Varley, J. S. Speck, and C. G. Van de Walle, "Structural and electronic properties of ga2o3-al2o3 alloys," *Applied Physics Letters*, vol. 112, no. 24, 2018.

[8] J. Rehm, T.-S. Chou, S. Bin Anooz, P. Seyidov, A. Fiedler, Z. Galazka, and A. Popp, "Perspectives on movpe-grown (100) β-Ga_2O_3 thin films and its al-alloy for power electronics application," *Applied Physics Letters*, vol. 121, no. 24, 2022.

[9] S. Mu, M. Wang, H. Peelaers, and C. G. Van de Walle, "First-principles surface energies for monoclinic Ga_2O_3 and Al_2O_3 and consequences for cracking of β-$(Al_xGa_{1-x})_2O_3$," *APL Materials*, vol. 8, no. 9, p. 081110, 2020.

[10] B. J. Baliga, "Semiconductors for high-voltage, vertical channel field-effect transistors," *Journal of applied Physics*, vol. 53, no. 3, pp. 1759–1764, 1982.

[11] N. Ma, N. Tanen, A. Verma, Z. Guo, T. Luo, H. G. Xing, and D. Jena, "Intrinsic electron mobility limits in β-Ga_2O_3," *Applied Physics Letters*, vol. 109, no. 21, 2016.

[12] M. Higashiwaki, K. Sasaki, A. Kuramata, T. Masui, and S. Yamakoshi, "Gallium oxide (Ga_2O_3) metal-semiconductor field-effect transistors on single-crystal β-Ga_2O_3 (010) substrates," *Applied Physics Letters*, vol. 100, no. 1, 2012.

[13] S. Pearton, F. Ren, M. Tadjer, and J. Kim, "Perspective: Ga_2O_3 for ultra-high power rectifiers and mosfets," *Journal of Applied Physics*, vol. 124, no. 22, 2018.

[14] M. J. Tadjer, "Toward gallium oxide power electronics," *Science*, vol. 378, no. 6621, pp. 724–725, 2022.

[15] Q. Feng, X. Li, G. Han, L. Huang, F. Li, W. Tang, J. Zhang, and Y. Hao, "$(AlGa)_2O_3$ solar-blind photodetectors on sapphire with wider bandgap and improved responsivity," *Optical Materials Express*, vol. 7, no. 4, pp. 1240–1248, 2017.

[16] X. Chen, F. Ren, S. Gu, and J. Ye, "Review of gallium-oxide-based solar-blind ultraviolet photodetectors," *Photonics Research*, vol. 7, no. 4, pp. 381–415, 2019.

[17] X. Wang, Z. Chen, D. Guo, X. Zhang, Z. Wu, P. Li, and W. Tang, "Optimizing the performance of a β-Ga_2O_3 solar-blind uv photodetector by compromising between photoabsorption and electric field distribution," *Optical Materials Express*, vol. 8, no. 9, pp. 2918–2927, 2018.

[18] Z. Galazka, A. Fiedler, A. Popp, S. Ganschow, A. Kwasniewski, P. Seyidov, M. Pietsch, A. Dittmar, S. B. Anooz, K. Irmscher *et al.*, "Bulk single crystals and physical properties of β-$(Al_xGa_{1-x})_2O_3$ (x= 0-0.35) grown by the czochralski method," *Journal of Applied Physics*, vol. 133, no. 3, p. 075105, 2023.

[19] T. Ohtsuki and M. Higashiwaki, "Crystallinity degradation and defect development in $(Al_xGa_{1-x})_2O_3$ thin films with increased al composition," *Journal of Vacuum Science & Technology A*, vol. 41, no. 4, 2023.

[20] J. Als-Nielsen and D. McMorrow, *Elements of modern X-ray physics*. John Wiley & Sons, 2011.

[21] A. Stierle and E. Vlieg, *Surface-sensitive X-ray diffraction methods*. Wiley Online Library, 2013.

[22] R. Feidenhans, "Surface structure determination by x-ray diffraction," *Surface Science Reports*, vol. 10, no. 3, pp. 105–188, 1989.

[23] M. Tolan, *X-ray scattering from soft-matter thin films: materials science and basic research*. Springer, 1999, vol. 148.

[24] H. Kiessig, "Interferenz von röntgenstrahlen an dünnen schichten," *Annalen der Physik*, vol. 402, no. 7, pp. 769–788, 1931.

[25] L. G. Parratt, "Surface studies of solids by total reflection of x-rays," *Physical review*, vol. 95, no. 2, p. 359, 1954.

[26] A. Stierle, *FEWLAY: a fitting software for x-ray reflectivity curves*.

[27] A. Glavic and M. Björck, "Genx 3: the latest generation of an established tool," *Applied Crystallography*, vol. 55, no. 4, pp. 1063–1071, 2022.

[28] B. L. Henke, E. M. Gullikson, and J. C. Davis, "X-ray interactions: photoabsorption, scattering, transmission, and reflection at e= 50-30,000 ev, z= 1-92," *Atomic data and nuclear data tables*, vol. 54, no. 2, pp. 181–342, 1993.

[29] M. P. Seah and W. Dench, "Quantitative electron spectroscopy of surfaces: A standard data base for electron inelastic mean free paths in solids," *Surface and interface analysis*, vol. 1, no. 1, pp. 2–11, 1979.

[30] D. R. Penn, "Quantitative chemical analysis by esca," *Journal of Electron Spectroscopy and Related Phenomena*, vol. 9, no. 1, pp. 29–40, 1976.

[31] M. Henzler and W. Göpel, *Oberflächenphysik des Festkörpers*. Springer-Verlag, 2013.

[32] H.-J. Butt, K. Graf, and M. Kappl, "Physics and chemistry of interfaces," 2013.

[33] A. Stierle, T. F. Keller, H. Noei, V. Vonk, and R. Roehlsberger, "DESY NanoLab," *Journal of large-scale research facilities JLSRF*, vol. 2, pp. A76–A76, 2016.

[34] "Surfaces interfaces x-ray scattering (SIXS) beamline at the soleil synchrotron." [Online]. Available: https://www.synchrotron-soleil.fr/en/beamlines/sixs

[35] "P24 chemical crystallography beamline at PETRA III, DESY." [Online]. Available: https://photon-science.desy.de/facilities/petra_iii/beamlines/p24_chemical_crystallography/index_eng.html

[36] D. Nečas and P. Klapetek, "Gwyddion: an open-source software for spm data analysis," *Central European Journal of Physics*, vol. 10, no. 1, pp. 181–188, 2012.

[37] S. Roobol, W. Onderwaater, J. Drnec, R. Felici, and J. Frenken, "Binoculars: data reduction and analysis software for two-dimensional detectors in surface x-ray diffraction," *Applied Crystallography*, vol. 48, no. 4, pp. 1324–1329, 2015.

[38] M. Creutzburg and A. Stierle, "Adsorption of carboxylic acids on magnetite single crystal surfaces," Nanolab, Tech. Rep., 2020.

[39] E. Vlieg, "A concise rod manual," 2001.

[40] D. Baker, "Crysalispro data collection and processing software for agilent x-ray diffractometers user manual," *Agilent Technologies, Poland*, 2013.

[41] "Polymorphism of Ga_2O_3 and the system Ga_2O_3—H_2O, author=Roy, Rustum and Hill, VG and Osborn, EF, journal=Journal of the American Chemical Society, volume=74, number=3, pages=719–722, year=1952, publisher=ACS Publications."

[42] S. Geller, "Crystal structure of β-Ga_2O_3," *The Journal of Chemical Physics*, vol. 33, no. 3, pp. 676–684, 1960.

[43] J. Åhman, G. Svensson, and J. Albertsson, "A reinvestigation of β-gallium oxide," *Crystal Structure Communications*, vol. 52, no. 6, pp. 1336–1338, 1996.

[44] Y. Ota, "Band alignment of β-$(Al_xGa_{1-x})_2O_3$ alloys via atomic solid-state energy scale approach," *AIP Advances*, vol. 10, no. 12, p. 115123, 2020.

[45] Z. Galazka, "Growth of bulk β-Ga_2O_3 single crystals by the Czochralski method," *Journal of Applied Physics*, vol. 131, no. 3, p. 125105, 2022.

[46] J. L. Lyons, "A survey of acceptor dopants for β-Ga_2O_3," *Semiconductor science and technology*, vol. 33, no. 5, p. 05LT02, 2018.

[47] K. Kaneko, K. Suzuki, Y. Ito, and S. Fujita, "Growth characteristics of corundum-structured α-$(Al_xGa_{1-x})_2O_3$/Ga_2O_3 heterostructures on sapphire substrates," *Journal of Crystal Growth*, vol. 436, pp. 150–154, 2016.

[48] E. Ahmadi, Y. Oshima, F. Wu, and J. S. Speck, "Schottky barrier height of ni to β-$(Al_xGa_{1-x})_2O_3$ with different compositions grown by plasma-assisted molecular beam epitaxy," *Semiconductor Science and Technology*, vol. 32, no. 3, p. 035004, 2017.

[49] X. Wang, Z. Chen, K. Saito, T. Tanaka, M. Nishio, and Q. Guo, "Temperature-dependent raman scattering in cubic $(InGa)_2O_3$ thin films," *Journal of Alloys and Compounds*, vol. 690, pp. 287–292, 2017.

[50] A. Kyrtsos, M. Matsubara, and E. Bellotti, "Migration mechanisms and diffusion barriers of vacancies in Ga_2O_3," *Physical Review B*, vol. 95, no. 24, p. 245202, 2017.

[51] Z. Galazka, R. Uecker, D. Klimm, K. Irmscher, M. Naumann, M. Pietsch, A. Kwasniewski, R. Bertram, S. Ganschow, and M. Bickermann, "Scaling-up of bulk β-Ga_2O_3 single crystals by the czochralski method," *ECS Journal of Solid State Science and Technology*, vol. 6, no. 2, pp. Q3007–Q3011, 2017.

[52] Z. Galazka, *Transparent semiconducting oxides: bulk crystal growth and fundamental properties*. Jenny Stanford Publishing, 2020.

[53] Z. Galazka, S. Ganschow, A. Fiedler, R. Bertram, D. Klimm, K. Irmscher, R. Schewski, M. Pietsch, M. Albrecht, and M. Bickermann, "Doping of czochralski-grown bulk β-Ga_2O_3 single crystals with cr, ce and al," *Journal of Crystal Growth*, vol. 486, pp. 82–90, 2018.

[54] Z. Galazka, K. Irmscher, R. Schewski, I. M. Hanke, M. Pietsch, S. Ganschow, D. Klimm, A. Dittmar, A. Fiedler, T. Schroeder *et al.*, "Czochralski-grown bulk β-Ga_2O_3 single crystals doped with mono-, di-, tri-, and tetravalent ions," *Journal of Crystal Growth*, vol. 529, p. 125297, 2020.

[55] Z. Galazka, R. Schewski, K. Irmscher, W. Drozdowski, M. E. Witkowski, M. Makowski, A. J. Wojtowicz, I. M. Hanke, M. Pietsch, T. Schulz *et al.*, "Bulk β-Ga_2O_3 single crystals doped with ce, ce+ si, ce+ al, and ce+ al+ si for detection of nuclear radiation," *Journal of Alloys and Compounds*, vol. 818, p. 152842, 2020.

[56] Z. Galazka, S. Ganschow, P. Seyidov, K. Irmscher, M. Pietsch, T.-S. Chou, S. Bin Anooz, R. Grueneberg, A. Popp, A. Dittmar *et al.*, "Two inch diameter, highly conducting bulk β-Ga_2O_3 single crystals grown by the czochralski method," *Applied Physics Letters*, vol. 120, no. 15, 2022.

[57] M. Higashiwaki and S. Fujita, *Gallium Oxide: Materials Properties, Crystal Growth, and Devices*. Springer Nature, 2020, vol. 293.

[58] R. Uecker, "The historical development of the czochralski method," *Journal of Crystal Growth*, vol. 401, pp. 7–24, 2014.

[59] G. K. Teal, "Single crystals of germanium and silicon—basic to the transistor and integrated circuit," *IEEE Transactions on electron devices*, vol. 23, no. 7, pp. 621–639, 2005.

[60] Z. Galazka, R. Uecker, K. Irmscher, M. Albrecht, D. Klimm, M. Pietsch, M. Brützam, R. Bertram, S. Ganschow, and R. Fornari, "Czochralski growth and characterization of β-Ga_2O_3 single crystals," *Crystal Research and Technology*, vol. 45, no. 12, pp. 1229–1236, 2010.

[61] S. Irvine and P. Capper, *Metalorganic vapor phase epitaxy (MOVPE): Growth, materials properties, and applications*. John Wiley & Sons, 2019.

[62] Leibniz-Institut für Kristallzüchtung (IKZ), "Sektion dünne oxidschichten," https://www.ikz-berlin.de/forschung-lehre/nanostrukturen-schichten/sektion-duenne-oxidschichten#group451464, accessed: 2026-06-02.

[63] T.-S. Chou, *Growth and characterization of epitaxial gallium oxide films*. Technische Universitaet Berlin (Germany), 2023.

[64] T.-S. Chou, S. Bin Anooz, N. Dropka, H.-H. Chen, Z. Galazka, M. Albrecht, A. Fiedler, and A. Popp, "Optimizing the morphology transition on movpe-grown (100) β-Ga_2O_3 film between step-flow growth and step-bunching: A machine learning-assisted approach," *APL Materials*, vol. 13, no. 5, 2025.

[65] T.-S. Chou, P. Seyidov, S. Bin Anooz, R. Grüneberg, T. T. V. Tran, K. Irmscher, M. Albrecht, Z. Galazka, J. Schwarzkopf, and A. Popp, "Fast homoepitaxial growth of (100) β-Ga_2O_3 thin films via movpe," *AIP Advances*, vol. 11, no. 11, 2021.

[66] S. Bin Anooz, A. Akhtar, T.-S. Chou, Z. Galazka, M. Schmidbauer, T. Remmele, M. Albrecht, A. Fiedler, and A. Popp, "Metalorganic vapor phase epitaxy of β-$(Al_xGa_{1-x})_2O_3$ (x= 0-0.55) and multilayer structure on (100) β-$(Al_{0.24}Ga_{0.76})_2O_3$ substrates," *Journal of Vacuum Science & Technology A*, vol. 44, no. 3, 2026.

[67] E. Vlieg, "Photon-based methods: 3.4. 2 x-ray diffraction from surfaces and interfaces," *Surface and Interface Science*, vol. 1, pp. 375–425, 2013.

[68] H. He, R. Orlando, M. A. Blanco, R. Pandey, E. Amzallag, I. Baraille, and M. Rérat, "First-principles study of the structural, electronic, and optical properties of Ga_2O_3 in its monoclinic and hexagonal phases," *Physical Review B—Condensed Matter and Materials Physics*, vol. 74, no. 19, p. 195123, 2006.

[69] K. Irmscher, Z. Galazka, M. Pietsch, R. Uecker, and R. Fornari, "Electrical properties of β-Ga_2O_3 single crystals grown by the czochralski method," *Journal of Applied Physics*, vol. 110, no. 6, 2011.

[70] P. Tasker, "The stability of ionic crystal surfaces," *Journal of Physics C: Solid State Physics*, vol. 12, no. 22, pp. 4977–4984, 1979.

[71] C. Noguera, "Polar oxide surfaces," *Journal of Physics: Condensed Matter*, vol. 12, no. 31, pp. R367–R410, 2000.

[72] Z. Dauter, "Twinned crystals and anomalous phasing," *Biological Crystallography*, vol. 59, no. 11, pp. 2004–2016, 2003.

[73] S. Parsons, "Introduction to twinning," *Biological Crystallography*, vol. 59, no. 11, pp. 1995–2003, 2003.

[74] S. Jenni and N. Ban, "Imperfect pseudo-merohedral twinning in crystals of fungal fatty acid synthase," *Biological Crystallography*, vol. 65, no. 2, pp. 101–111, 2009.

[75] T. Hahn and H. Klapper, "Twins of twins," 2013.

[76] T. Matsumoto, A. Yamano, T. Sato, J. D. Ferrara, F. J. White, and M. Meyer, "" what is this?" a structure analysis tool for rapid and automated solution of small molecule structures," *Journal of Chemical Crystallography*, vol. 51, no. 3, pp. 438–450, 2021.

[77] D. Nečas and P. Klapetek, "Gwyddion: an open-source software for SPM data analysis," *Open Physics*, vol. 10, no. 1, pp. 181–188, 2012.

[78] A. Dawiec, Y. Garreau, J. Bisou, S. Hustache, B. Kanoute, F. Picca, G. Renaud, and A. Coati, "Real-time control of the beam attenuation with xpad hybrid pixel detector," *Journal of Instrumentation*, vol. 11, no. 12, p. P12018, 2016.

[79] I. Robinson and D. Tweet, "Surface x-ray diffraction," *Reports on Progress in Physics*, vol. 55, no. 5, p. 599, 1992.

[80] I. K. Robinson, "Crystal truncation rods and surface roughness," *Physical Review B*, vol. 33, no. 6, p. 3830, 1986.

[81] G. Wagner, M. Baldini, D. Gogova, M. Schmidbauer, R. Schewski, M. Albrecht, Z. Galazka, D. Klimm, and R. Fornari, "Homoepitaxial growth of β-Ga_2O_3 layers by metal-organic vapor phase epitaxy," *Physica Status Solidi (a)*, vol. 211, no. 1, pp. 27–33, 2014.

[82] T. Lovejoy, E. Yitamben, N. Shamir, J. Morales, E. Villora, K. Shimamura, S. Zheng, F. Ohuchi, and M. Olmstead, "Surface morphology and electronic structure of bulk single crystal β-Ga_2O_3 (100)," *Applied Physics Letters*, vol. 94, no. 8, p. 081906, 2009.

[83] W. de Poel, S. Pintea, J. Drnec, F. Carla, R. Felici, P. Mulder, J. A. Elemans, W. J. van Enckevort, A. E. Rowan, and E. Vlieg, "Muscovite mica: Flatter than a pancake," *Surface Science*, vol. 619, pp. 19–24, 2014.

[84] R. Schewski, M. Baldini, K. Irmscher, A. Fiedler, T. Markurt, B. Neuschulz, T. Remmele, T. Schulz, G. Wagner, Z. Galazka *et al.*, "Evolution of planar defects during homoepitaxial growth of β-Ga_2O_3 layers on (100) substrates—a quantitative model," *Journal of Applied Physics*, vol. 120, no. 22, p. 225305, 2016.

[85] P. Tasker, "Stability of ionic-crystal surfaces," *Journal of Physics C- Solid State Physics*, vol. 12, no. 22, pp. 4977–4984, 1979.

[86] J. Goniakowski, F. Finocchi, and C. Noguera, "Polarity of oxide surfaces and nanostructures," *Reports on Progress in Physics*, vol. 71, no. 1, p. 016501, JAN 2008.

[87] V. Bermudez, "The structure of low-index surfaces of β-Ga_2O_3," *Chemical Physics*, vol. 323, no. 2-3, pp. 193–203, 2006.

[88] M. Busch, E. Meyer, K. Irmscher, Z. Galazka, K. Gärtner, and H. Winter, "Fast atom diffraction from a β-Ga_2O_3 (100) surface," *Applied Physics Letters*, vol. 105, no. 5, p. 051602, 2014.

[89] A. Vlad, A. Stierle, M. Marsman, G. Kresse, I. Costina, H. Dosch, M. Schmid, and P. Varga, "Metastable surface oxide on coga (100): Structure and stability," *Physical Review B—Condensed Matter and Materials Physics*, vol. 81, no. 11, p. 115402, 2010.

[90] A. Stierle, R. Streitel, P. Nolte, A. Vlad, I. Costina, M. Marsman, G. Kresse, E. Lundgren, J. N. Andersen, R. Franchy *et al.*, "Real time observation of ultrathin epitaxial oxide growth during alloy oxidation," *New Journal of Physics*, vol. 9, no. 9, p. 331, 2007.

[91] A. S. Kilian, A. de Siervo, R. Landers, G. J. P. Abreu, M. S. Castro, T. Back, and A. Pancotti, "Unravelling the surface structure of β-Ga_2O_3 (100)," *RSC advances*, vol. 13, no. 40, pp. 28 042–28 050, 2023.

[92] M. Higashiwaki, K. Sasaki, H. Murakami, Y. Kumagai, A. Koukitu, A. Kuramata, T. Masui, and S. Yamakoshi, "Recent progress in Ga_2O_3 power devices," *Semiconductor Science and Technology*, vol. 31, no. 3, p. 034001, 2016.

[93] M. Higashiwaki, K. Sasaki, T. Kamimura, M. Hoi Wong, D. Krishnamurthy, A. Kuramata, T. Masui, and S. Yamakoshi, "Depletion-mode Ga_2O_3 metal-oxide-semiconductor field-effect transistors on β-Ga_2O_3 (010) substrates and temperature dependence of their device characteristics," *Applied Physics Letters*, vol. 103, no. 12, p. 123511, 2013.

[94] M. Higashiwaki, K. Sasaki, A. Kuramata, T. Masui, and S. Yamakoshi, "Development of gallium oxide power devices," *physica status solidi (a)*, vol. 211, no. 1, pp. 21–26, 2014.

[95] T. Wang, W. Li, C. Ni, and A. Janotti, "Band gap and band offset of Ga_2O_3 and $(Al_xGa_{1-x})_2O_3$ alloys," *Physical Review Applied*, vol. 10, no. 1, p. 011003, 2018.

[96] F. Zhang, K. Saito, T. Tanaka, M. Nishio, M. Arita, and Q. Guo, "Wide bandgap engineering of $AlGa_2O_3$ films," *Applied Physics Letters*, vol. 105, no. 16, 2014.

[97] M.-C. Kao, L. P. Schewe, A. Akhtar, A. Vlad, T. F. Keller, K. Henkel, S. B. Anooz, A. Popp, Z. Galazka, J. I. Flege, A. Stierle, and V. Vonk, "Surface termination of β-Ga_2O_3 as-cleaved single crystals," *Applied Physics Letters*, vol. 128, no. 7, p. 071601, 02 2026.

[98] Z. Galazka, A. Fiedler, A. Popp, P. Seyidov, S. B. Anooz, R. Blukis, J. Rehm, K. Tetzner, M. Pietsch, A. Dittmar *et al.*, "Solid-solution limits and thorough characterization of bulk β-$(Al_xGa_{1-x})_2O$ single crystals grown by the czochralski method," *Advanced Materials Interfaces*, vol. 12, no. 2, p. 2400122, 2025.

[99] Z. Galazka, "Current status of bulk β-(Ga_2O_3 and β-(Al_xGa_{1-x})$_2O_3$ crystal growth," *IEEE Transactions on Semiconductor Manufacturing*, 2025.

[100] B. Warren, "Warren X-ray Diffraction," 1969.

Acknowledgements

My sincere gratitude goes to everyone who supported me during my time at the DESY NanoLab. Countless beamtime experiments, hours spent growing perfect nanoparticles, building experimental chambers, troubleshooting, attending meetings, and engaging in fruitful discussions throughout my PhD journey contributed greatly to the completion of this dissertation.

I would like to express my deepest gratitude to my supervisors, **Prof. Dr. Andreas Stierle** and **Dr. Vedran Vonk** for making this work possible and for giving me this opportunity to pursue my PhD. I am especially thankful for the chance to work on several challenging research projects and beamtime experiments, as well as to participate in conferences abroad. I also deeply appreciate their valuable advice and guidance during my PhD journey and the proof-reading of this thesis and many manuscripts.

I thank **Prof. Dr. Wolfgang Parak** for chairing my PhD defense and being a member of the committee, as well as the other committee members, **Prof. Dr. Jan Ingo Flege** and **Prof. Dr. Gabriel Bester**, for their time, their valuable comments, and for evaluating my work.

I am deeply grateful to my colleagues **Prof. Dr. Andreas Stierle**, **Dr. Vedran Vonk**, **Lukas Paul Schewe**, **Luis Felipe Mochalski**, **Luisa Wartner**, and **Simon Geile** for their support during my SCXRD beamtime at P24 beamline in DESY, and to **Prof. Dr. Andreas Stierle**, **Dr. Vedran Vonk**, **Lukas Paul Schewe**, **Arub Akhtar**, and **Simon Geile** for their support during my SXRD experiment at SIXS beamtime in the SOLEIL synchrotron. Many thanks also to the beamline staff at the SIXS beamline in the Soleil synchrotron, **Dr. Alina Vlad**, **Prof. Dr. Garreau Yves**, **Dr. Andreas Resta**, **Dr. Alessandro Coati**, and **Benjamin Vosin**, as well as to the beamline scientist at P24 beamline in DESY, **Dr. Carsten Paulmann**. Thank you all so much for the support during the beamtimes.

Many thanks to **Dr. Vedran Vonk** and **Dr. Marcus Creutzburg** for their assistance with the analysis of the SXRD data and the use of the ROD program, as well as to **Dr. Thomas Keller**

for his assistance with the AFM image analysis. I would like to thank **Katharina Röper** for her help and support with all administrative matters.

I would also like to thank the Deutsche Forschungsgemeinschaft (DFG, German Research Foundation) and DESY, a member of the Helmholtz Association (HGF), for funding and supporting this research project. I am also grateful to all DFG project collaborators, **Prof. Dr. Andreas Stierle**, **Dr. Vedran Vonk**, **Prof. Dr. Jan Ingo Flege**, **Dr. Andreas Popp**, **Dr. Zbigniew Galazka**, **Dr. Saud Bin Anooz**, **Karsten Henkel**, **Lukas Paul Schewe**, **Arub Akhtar**, and **Jana Rehm** for the fruitful discussions and valuable collaboration. Special thanks go to **Dr. Zbigniew Galazka** for providing the high-quality AlGaO single crystals studied in this thesis.

My special thanks go to my parents in Taiwan, **Mei-I Lin** and **Cheng-Kang Kao**, for their unwavering support throughout my pursuit of this PhD's degree in Germany.

Last but not least, I am deeply grateful to my wife, **Lina-Sophie**, for her emotional support and encouragement in everyday life, as well as her understanding throughout this journey, especially during the beamtime experiments and the writing period of this thesis.